Mixing in axisymmetric gravity currents and volcanic conduits

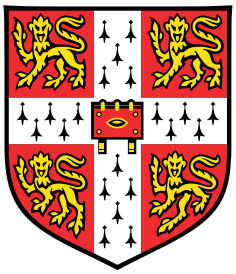

Peeradon Samasiri

Department of Earth Sciences
University of Cambridge

This dissertation is submitted for the degree of
Doctor of Philosophy

Churchill College August 2018

Mixing in axisymmetric gravity currents and volcanic conduits

Peeradon Samasiri

The first part of this thesis investigates the mixing of ambient fluid into axisymmetric high Reynolds number gravity currents. A series of laboratory experiments were conducted in which small scale gravity currents travelled along a wedge shaped channel with an increasing width in the downstream direction. The channel was filled with fresh water and the current was generated using saline solution introduced either by a rapid release of a known finite volume from behind a lock gate or by pumping at a constant rate into the apex of the channel. The distribution and evolution of the density of the flow with distance downstream was measured using a light attenuation technique. Additional experiments were performed by injecting parcels of dye in different regions of the flow in order to visualise the motion of fluid in and surrounding the gravity current. Unlike currents introduced by the release of a finite volume of fluid, where most mixing occurs in the head of the flow, currents produced from a steady source develop a steady tail region behind the front which is also found to entrain a significant amount of ambient fluid. In both types of current, we estimate the fraction of displaced ambient fluid that is entrained into the flow. We then derive a new class of self-similar solutions for gravity currents produced from a finite volume release of fluid.

The second part of this thesis develops the experimental method of measuring mixing using light attenuation to investigate the mixing of liquid in a vertical conduit which results from a continuous stream of high Reynolds number gas bubbles. The experiments identify that the mixing in the wake of the bubbles leads to a net dispersive transport along the conduit. The process provides an explanation for the heat transfer within a volcanic conduit in the case of a gas-slug flow regime as occurs in the near surface region of volcanic conduits connected to surface lava lakes. We derive a theoretical model to estimate the heat flux associated with such a system using the empirical law for the dispersive mixing. The predicted heat flux associated with the bubbles is found to be comparable to the heat loss at the surface of lava lakes associated with radiative and convective heat loss. Given values for the gas flux, the lake area and the temperature at the surface of the lake, the model enables new predictions for the size of the volcanic conduit.

To my mother, sisters
and His Late Majesty King Bhumibol of Thailand.

Declaration

I hereby declare that except where specific reference is made to the work of others, the contents of this dissertation are original and have not been submitted in whole or in part for consideration for any other degree or qualification in this, or any other university. This thesis is my own work and contains nothing which is the outcome of work done in collaboration with others, except as specified in the text and Acknowledgements. This thesis contains less than 275 numbered pages of which not more than 225 pages are text, appendices, illustrations and bibliography.

Peeradon Samasiri
August 2018

Publication

The majority of the work discussed in chapters 2 has been published in a peer-reviewed journal as appear in the paper:

- Samasiri, P., Woods, A. W. 2015. Mixing in axisymmetric gravity currents. *Journal of Fluid Mechanics*, **782**.

Acknowledgements

Firstly, this thesis would not have been possible without great guidance and support from Professor Andy Woods, my supervisor, who has always motivated and enthused me throughout the past four years. His advice has deeply shaped and developed not only my research skills but also my critical thinking and scientific creativity.

My experimental works at BP Institute could not have been performed without massive help from Andrew Pluck, who has created, designed and fixed all our experimental apparatus. I would also like to thank Lotty Gladstone for her helpful advice on experimental techniques, as well as Nicola and Diana for their advice and help in the laboratory. Special thanks go out to everyone in BPI, especially the top floor people: Charanee A, Joanna S, Martin L, Neeraja B, Finn B, Fin A, Tim BJ, and Peter D.

A special shout out to my beloved colleagues in room Danger Pond: Stefano Rocco for all of his compliments that kept boosting my self-confidence; Marcus Horsely for his great entertaining skills and encouraging photo above my desk; Richard Alloway for always giving us a spare desk and also Wei Jin Gun for all the cakes you baked for us during the first few years of my degree.

Cambridge can surprisingly form a warm and cosy (also nosy) Thai society. I would like to especially thank Pac Peerapat, Khaow T, Baitong T, Earn Isaree and Lily K for helping me adapt to Cambridge as though it were my second home. I am also very grateful to have crossed paths with fantastic friends like Keng Nakarin, Nae Nontawit and Earth Kawin, and to have experienced the Cambridge university life together. Thank you, Fasai Nonthiwat, Rainbow Nattaphong and also Kusala T, who have been through all good and bad times since we came to live in the sunny UK island.

Lastly, Sean K R Chia, for always being there for me.

Table of contents

List of figures **xvii**

List of tables **xxix**

List of symbols **xxxi**

1 Introduction **1**

1.1 Gravity currents . . . 1

1.1.1 Motivation . . . 1

1.1.2 Modelling gravity currents . . . 3

1.1.3 Entrainment in a turbulent plume . . . 8

1.1.4 Entrainment in a gravity current . . . 10

1.1.5 Research outline . . . 12

1.2 Heat supply to lava lakes . . . 14

1.2.1 Motivation . . . 14

1.2.2 Heat loss at a lava lake . . . 15

1.2.3 Heat supply by magma convection . . . 18

1.2.4 Heat supply by gas bubbles . . . 21

1.2.5 Experimental two-phase flow in a vertical conduit . . . 23

1.2.6 Research outline . . . 27

2 Finite volume release axisymmetric gravity currents **29**

2.1 Abstract . . . 29

2.2 Introduction . . . 30

2.3 Experimental Method . . . 31

2.4 Experimental Observations . . . 35

2.4.1 Mechanism of Mixing . . . 35

2.4.2 Entrainment coefficient . . . 38

2.4.3 Scaling Laws for the Head . . . 39
2.4.4 Structure of the current . . . 41
2.5 A depth averaged model . . . 43
2.6 Discussion . . . 47

3 Steady flux axisymmetric gravity currents 49
3.1 Abstract . . . 49
3.2 Introduction . . . 50
3.3 Experimental method . . . 51
3.4 Experimental observations . . . 54
3.4.1 Current development near the source . . . 54
3.4.2 Evolution of the flow . . . 57
3.4.3 Mechanism of mixing . . . 57
3.5 The properties near the front . . . 60
3.5.1 Front position, r_n . . . 60
3.5.2 Frontal Froude number . . . 63
3.6 Entrainment coefficients . . . 65
3.6.1 Estimating velocity profiles . . . 65
3.6.2 Entrainment in the body region . . . 68
3.6.3 Entrainment in the front region . . . 71
3.7 Comparison with theoretical models . . . 74
3.7.1 Mathematical considerations . . . 74
3.7.2 Comparison with the experimental data . . . 77
3.8 Discussion and conclusion . . . 79

4 Thermodynamics of a lava lake 81
4.1 Abstract . . . 81
4.2 Introduction . . . 81
4.3 Experimental Method . . . 83
4.4 Results . . . 83
4.4.1 Qualitative descriptions for mixing in the wake . . . 83
4.4.2 Bubble characteristics . . . 85
4.4.3 A modelling approach for mixing process . . . 88
4.5 Modelling temperature profile within a volcanic conduit . . . 92
4.5.1 Model development . . . 92
4.5.2 Model validation . . . 95

4.5.3 Additional consideration for solidified crusts 99
4.5.4 Transition depth to conduit-filling bubbles 100
4.6 Application to geological problems 103
4.6.1 Erta 'Ale 103
4.6.2 Erebus 107
4.6.3 Stromboli 109
4.6.4 Villarica 111
4.6.5 Nyiragongo 112
4.7 Conclusion 114

5 Conclusions and future work **115**
5.1 Mixing in axisymmetric gravity currents 115
5.1.1 Conclusion 115
5.1.2 Future work 117
5.2 Thermodynamics of a lava lake 118
5.2.1 Conclusion 118
5.2.2 Future work 119

References **121**

Appendix A **131**
A.1 Error approximation based on conservation of dyes 131
A.2 The sensitivity for the current detection 132

List of figures

1.1 Photos of (left) a snow avalanche (image from Scientif38 2007, Wikipedia, 15 September 2017) and (right) turbidite deposit at Gorgoglione Flysch, South Italy (image from Geologist 2004, Wikipedia, 15 September 2017). 2

1.2 Photos of lava lakes at (left) Marum crater, Ambrym, Vanautu (image from Cai Tjeen Willink 2011, Wikipedia, 15 September 2017) and (right) Nyiragongo, Congo (image from Geophile71 2009, Wikipedia, 15 September 2017). 14

1.3 A digital image of Erta 'Ale lava lake taken in February 2001 showing a moderately active surface. Several incandescent cracks in between solidified crusts can be observed. Inset shows a thermal image obtained from the same location but taken 15 mins earlier. The figure is taken from Oppenheimer & Yirgu (2002). 16

1.4 A generic thermal and mass balance model based on magma convection (taken from Harris *et al.*, 1999, relabelled based on our notations). The model implies exchange flow within the conduit and replenishment of magma in the lake. The total heat loss at the surface of the lava lake ($\dot{Q}_{\rm rad}+\dot{Q}_{\rm conv}$) can be balanced by cooling ($\dot{M}_{\rm magma}c_m\Delta T$) and crystallising fresh magma ($\dot{M}_{\rm magma}c_L\Delta f$) arriving at the lake due to the exchange flow. 19

1.5 Diagrams showing models for (a) bi-directional flow (adapted from Stevenson & Blake (1998)) and (b) bubble rising in the conduit (adapted from Bouche *et al.* (2010)). For the bi-directional flow model, it might be unclear where the overturn actually occurs. Some authors believed that the overturn may happen within the lava lake as inferred from horizontal motion at the surface. 21

1.6 A plot for predicted bubble diameter, $2r_b$, at different depths based on the bubble volume observed at the surface within the range 10-1000 m^3. The calculation assumes the bubbles are spherical and are compressed at depth due to magmastatic pressure. The dotted line illustrates that for a given conduit size of 4 m, a 10 m^3 (volume at the surface) bubble would be conduit-filling in the top 100 m. Bubbles with larger mass would become conduit-filling at a deeper level. 22

1.7 Idealised vertical gas-liquid flow regime in vertical conduits (adapted from Pioli *et al.*, 2012). Liquid is shown in gray and gas bubbles are shown in white. For low gas flux, small gas bubbles may rise independently and bubbles have uniform size distribution. Increasing gas flux promotes bubble coalescence creating bubbles of different sizes. In slug flow, large bubbles become spherical-cap and fill up the conduit diameter. Increasing gas flux further, the large bubble becomes elongated and has the shape that resembles a Taylor bubble. Gas bubbles becomes unstable with further increase in gas flux which characterise churn flow regime. At annular flow conditions, the fluid may be dragged upwards by the gas motion. 24

2.1 Schematic diagram of the experimental tank, showing a top view and a side view of the tank. Figure also illustrates the depth h of the current at radius r, the maximum depth h_n, the position of the nose of the current r_n, and the radius of the lock gate, r_o. 32

2.2 (a) Photographs of a saline gravity current illustrating the evolution of the buoyancy, shown by false-colour contours, as the current from experiment H (Table 2.1) advances along the flume. Images are taken at equal time intervals of 1.5s. The x-axis shows the position in the current as a function of the number of lock lengths. The colour scale represents the value g'/g'_o which is the local buoyancy, g', measured as a fraction of the original buoyancy, g'_o. (b) Evolution of the depth averaged buoyancy of the flow as a function of position and time. The horizontal axis represents horizontal position, r/r_o, and the vertical axis is time. The colours represent the depth averaged buoyancy of the gravity current, with the legend illustrating the fraction of original buoyancy of the fluid which was released from behind the lock gate. The triangles in the figure denote the horizontal position at which the volume of the current in the region between the back of the lock and the triangle equals 25% of the total volume of the current (see figure 2.6b). 33

2.3 Series of images of the current at successive times. (a) Transport of a pulse of red dye injected just behind the front of the flow in the head (Exp. M). This shows how the dyed fluid in the current advances to the front of the flow, and then recirculates over the top of the current. Here it mixes with the ambient fluid which is displaced up over the advancing head of the flow. (b) Transport of dyed blue ambient fluid injected just ahead of the front of the red current (Exp. N). Some of the ambient fluid displaced by the current remains above the current after the head has passed by, and hence does not mix with the current, while the remainder mixes into the current, recirculating in the flow. . . 36

2.4 Variation as a function of r_n/r_o of (a) the volume of the current; (b) the height of the head of the current in the region $r_o < r_n < 8r_o$ and (c) the entrainment coefficient ε defined by (2.3) and estimated from the experimental data shown in panels a and b. Colours represent results from different experiments as coded in table 2.1. 37

2.5 Data from experiments A-L (Table 2.1) illustrating (a) the variation with time of $\mathcal{R} = r_n(t)/B^{1/4}(t+t_o)^{1/2}$, where r_n is the position of the nose of the current as a function of time; (b) the variation with time of the Froude number, $Fr = \left(\frac{\mathrm{d}r}{\mathrm{d}t}\right)_n (\overline{g'_n}h_n)^{-\frac{1}{2}}$, where $(\overline{g'}h)_n$ is the maximum value of the vertical integral of buoyancy as a function of the position in the current; (c) the variation of the Reynolds number in the head with time. The data that fall below $Re = 5000$ appear to be influenced by friction, and are not shown in panels a-b. Colours represent results from different experiments as coded in table 2.1. 40

2.6 Variation with position r/r_n of (a) the buoyancy in the current between the source and radius r as a fraction of the total buoyancy, $\int_0^r r\overline{g'}hdr / \int_0^{r_n} r\overline{g'}hdr$ (Exp. H), (b) the volume of the current in the region between the source and the position r as a fraction of the total volume, $\int_0^r rhdr / \int_0^{r_n} rhdr$ (Exp. H), (c) profiles of the dimensionless vertical integral of buoyancy (eqn 5a) and (d) profiles of the dimensionless depth (eqn 5b). (a,b) The black contour lines denote the horizontal location where the fraction of (a) the total buoyancy or (b) the total volume exceeds the value 0.1, 0.2, ..., 1.0. (c,d) Gray profiles denote the time-average for each of the experiments A-L. The ensemble averages, standard deviations from these ensemble averages and the prediction of the simplified similarity solution (eqn 12) are shown in black, blue and red profiles, respectively. 41

3.1 Schematic diagram showing the top and side views of the experimental tank. 52

3.2 Photographs of the currents near the source region ($r < 85$ cm) comparing the initiation of the flow generated from high and low, Q_j, in the left and right panels, respectively. In (a), the head may grow as big as 10 cm compared to (b) which develop only small head and the current appears to be laminar. Panels (c) and (d) show a photograph of the corresponding currents at large time. Panels (e) and (f) show the height profile at $t = 12.5 - 20$ s within the region $r < 85$ cm. During this time, the head of the current has already propagated downstream beyond the scope of the panel. The height profiles show that behind the head, the depth of the current appears to be quasi-steady. 54

3.3 (a) Photographs of a saline gravity current (exp. C) illustrating the evolution of the normalised buoyancy in the current, shown by false-colour contours, as it advances along the flume. Images are taken at time intervals of 1.25 s. Evolution of (b) the vertical integral of the buoyancy, $\int g' dz$, and (c) height, h, are shown as functions of radius on the x-axis and time on the y-axis. Near the front, the maximum integral buoyancy tends to decrease significantly while the maximum depth is approximately constant suggesting dilution within the front. The inverted triangles (black/white) indicates the separation at which 65% of total volume at each time is located. This boundary is later used in §3.6.3 to define the boundary between the head and the body of the current in our study. 56

3.4 A gravity current initially dyed yellow but which becomes colourless with time displaces a parcel of red dye located at $r = 125$ cm. Red dye is entrained into the head and travel together with the propagation of the front. The front then displaces blue dye located at $r = 175$ cm. The red and blue dyes do not seem to penetrate the whole depth as the bottommost of the current remains yellow-colourless during the whole flow. 58

3.5 (a) Photos displayed for $100 < r < 250$ cm shows blue dye being displaced by the head of yellow gravity current. A fraction of it mixes into the head and moves with the front of the gravity current. At the same time, red dye is injected behind the head into the body region but can eventually reach the front. Within the body, the fluid at the bottom appears to travel faster than the top part which can be seen by the shear of injected red dye. (b) The same current but is shown relative to front of the current. The advance of the red and blue dyes are traced and shown in the corresponding lines. 59

3.6 Schematic diagram of mixing in an axisymmetric gravity current. . . . 59

3.7 (a-c) The ratio of the coefficients provided by different power laws (3.6) have been compared. Black lines in (a) and (b) show the averaged values of the asymptotic $\mathcal{R}$ for different experiments while $\mathcal{R}_J$ does not seem to converge to a constant within our range of study. (d) Deviations of $\mathcal{R}$ to the associated asymptotic values, $\mathcal{R}(\hat{t}_{\max})$. It appears that $\mathcal{R}_C$ converges to its asymptotic value faster than $\mathcal{R}_S$ and $\mathcal{R}_J$. (e) The time averaged (with error bars representing standard deviation) ratios from the conventional power law: $r_n \sim t^{3/4}$ as a function of Fr_o for $\hat{t} > 5$. (f) The frontal position as a function of time. The black line shows the predicted r_n using $r_n = 1.33B_o^{1/4}t^{3/4}$. For (a-c) and (e), the results from different experiments are plotted in different colours as coded in table 3.1. 61

3.8 Variation as a function of normalised time of (a) instantaneous frontal velocity together with predicted frontal velocity based on conventional scaling: $\hat{r}_n = 1.33\hat{t}^{3/4}$, shown in black line; and (b) frontal Froude numbers estimated from the experimental data. (c) Time-averaged for $\hat{t} > 5$ for experimental frontal Froude numbers as a function of the effective source Froude numbers. Colours represent results from different experiments as coded in table 3.1. 64

3.9 (a) Time-series image of buoyancy, g', at $z = 2$ cm. Successive eddies can be seen in the image as streaks dense liquid (blue) on top of the background buoyancy (green). (b) Graphical illustration of how time-series image, $f(r,t)$, can be transformed into a Radon domain, $R_\theta(r')$. (c) Following the built-in Matlab Radon transform function, the image pixels are first divided into four sub-pixels before being remapped into the projected axis. 66

3.10 Vertical profiles of time-averaged velocity (red) and buoyancy (blue) of fluid within the body region of the gravity current. The red dotted lines show the error bounds associated with the predicted velocity profiles. The yellow lines show the time-averaged depth, h_r, of the current at the corresponding radial position. The fluctuation in depth of the current leads to non-zero buoyancy above this height. Near the top boundary, tracking eddies fails to suggest reliable speed of the flow. Hence, velocity profiles are extrapolated from the velocity at $z = 0.9h_r$ and assumed to reach zero where time-averaged buoyancy reaches zero. The numbers show the gradient Richardson number, Ri_g, associated to the two regions: $z > 0.9h_r$ and $0.1h_r < z < 0.9h_r$, calculated using the averaged gradient corresponding to each zone. 67

3.11 Plots show the properties within the tail of experimental gravity currents. (a) The radial fluxes are calculated from the velocity profiles and normalised by the corresponding effective source fluxes defined at r =60 cm. The general trend shows an increasing source flux with radius which can reach a value of 1.2-1.8 of Q_o at $r = 150$ cm. (b) The time-averaged depths show that the depth of each current is approximately constant in the tail region. (c) The depth-averaged velocities, $\bar{u}_r$, calculated from $Q_r = ru_rh_r$ show a generally decreasing trend with radius for each experiment. Colours represent results from different experiments as coded in table 3.1. 69

3.12 (a-c) Plots from experiment A showing measured time-averaged properties within the tail region of (a) the normalised volume flux at different radii, $\int ru\mathrm{d}z/Q_o$, and the curve fit associated with it; (b) h_r and u_r together with the estimated u_r determined from the curve fit of Q_r shown in (a), using $Q_r = ru_rh_r$; and (c) the approximation of the mixing coefficient along the back of the current, $\varepsilon_b = (h_r/Q_r)\,(\mathrm{d}Q_r/\mathrm{d}r)$, where $\mathrm{d}Q_r/\mathrm{d}r$ is determined from the curve fit of Q_r. The radial-averaged values, within the range $60 < r < 150$ cm, of h_r and ε_b from different experiments are shown as a function of Fr_o in (d) and (e), respectively. The error bars show standard deviations and the different experiments are plotted in different colours as coded in table 3.1. 70

3.13 (a) A plot of normalised volume with normalised time shows that the chosen length and time scales can successfully collapse the experimental data. The black line shows the source volume of the current based on the supply rate, Q_o. (b) A plot of volume change in time based on the data. The linear best fit (black line) is chosen to describe the general trend for experimental volume change. (c) The estimated volume fluxes associated with different parts of the currents. The crosses ($\times$) show the approximated volume fluxes being displaced by the advancing fronts, $r_n h_n u_n$ while the dots ($\cdot$) show the estimate volume fluxes being supplied behind the heads at $r_s(t)$. (d) The mixing coefficient near the front, $\varepsilon_n = 0.20 \pm 0.04$, is estimated from the volume change of the data. The mixing coefficients converge to a constant for each experiment but slightly vary from one experiment to another. (e) The time-averaged ε_n for $\hat{t} > 10$ from different experiments are plotted as a function of Fr_o. Colours represent results from different experiments as coded in table 3.1. 72

3.14 The experimental data for the height and vertical integral buoyancy profiles from experiment C at different time. The predicted height profiles, following Johnson *et al.* (2015)'s model, calculated from associated Fr_o and $\langle Fr_n \rangle$ for this experiment (table 3.1) are shown for comparison. We also plotted the vertical profiles of $\hat{g}'$ at $\hat{r} = 2, 3, 4, ... < \hat{r}_s$. The profiles are scaled such that they are 0 at their corresponding positions and are 1 at the positions of the next adjacent profiles. 78

4.1 Photos of dye mixing due to gas flows in a vertical tube. Dye originally located at the bottom of the tube is gradually mixed and transported upwards under the influence of bubbles rising within the conduit. . . . 84

4.2 Time series for gas slugs rising in a vertical conduit. The liquid phase was primarily mixed with red dye resulting from the conduit mixing by the bubble flow. The speed at which the bubbles rise can be determined from the gradient of bubbles in the plot which can be seen to be similar for each bubble. The speed is approximately constant except just before bubble coalescence, where the bubble is seen to accelerate (steeper slope) to catch up with the preceding bubble. 85

4.3 Plots for bubble length, L_b, and bubble fraction, L_b/L, as a function of superficial gas speed, u_g. Gas flux is normalised by u_bA which is found to collapse all the data from inviscid experiments ($\nu < 0.1$ cm^2 s^{-1}). The results from different liquid viscosities are plotted in different colours. 86
4.4 Schematic diagram showing some nomenclature used to described a slug unit. 86
4.5 shows the concentration profiles from a dye attenuation experiment. (a) Time series of averaged concentration re-plotted in the $z^2 - t$ domain shows a linear trend starting from the point of injection ($z = 0, t = 0$). Bubbles are filtered out using median filter over time direction. (b) Plots of normalised concentration profiles at different times, shown as plots in different colours, as a function of z^2/t shows collapse of the data confirming a diffusion-like process for dye propagation under the influence of bubble flow. The black line illustrates the best fit which determines the dispersion coefficient, D, describing this experiment. . . 89
4.6 (a) Plot of normalised diffusion coefficient, $D/(d_cu_g)$, as a function of, u_o/u_g. (b) Plot of normalised diffusion coefficient, $Du_g^{1/2}/(d_cu_gu_o^{1/2})$, as a function of, u_o/u_g. The black solid line illustrates the approximate fit to the data expressed in equation (4.9) and the dotted line corresponds to the asymptotic value expected for large u_o/u_g (4.10). The results from different liquid viscosities are plotted in different colours. 89
4.7 Numerical solutions for a model concerning heat flux due to gas expansion and partial thermal exchange between gas bubble and liquid melts. The boundary conditions are set for $T_g = T_m = 1000^o$C and $\mathrm{d}T_g/\mathrm{d}z = \mathrm{d}T_m/\mathrm{d}z$ at z = -1 km. 96
4.8 T_m at the surface as predicted for different gas fluxes, conduit diameters and initial bubble sizes at the base of the conduit. The conduit is set to be 1 km deep and the magma temperature gradient at $z = -z_{\max}$ is assumed to be the same as the gas temperature gradient. 97
4.9 Surface temperature as predicted by function of different $\mathrm{d}T_m/\mathrm{d}z$ at z = -1 km. The result is shown for the conduit diameter of 4 m. 97

4.10 A plot of heat supply/loss at a lava lake. Dotted lines show the estimated total heat loss ($\dot{Q}_{\text{rad}}+\dot{Q}_{\text{conv}}$) as a function of surface temperature T_m for lava lake of the sizes (from bottom to top) 100, 1000, 10000 m^2. Coloured lines show the predicted heat supply associated with different gas fluxes as a function of predicted temperature which is varied by changing $\text{d}T_m/\text{d}z$ at the source depth. Dashed lines show the predicted values at 50 m below the surface while solid lines show the predicted values at the surface and are plotted as a function of their corresponding local temperatures. The model is set for $d_c = 4$ m, $-z_{\text{max}} =$ -1 km and initial $r_b = 1.8$ m. 98

4.11 Plots of estimated transition depth where the gas bubble becomes conduit filling as a function of conduit diameter for given gas flux and bubble frequency. The bubble frequency chosen is equivalent to bubble appearance of (from left to right) one every second, minute and ten minutes. 101

4.12 Comparison between our model and the field data acquired from Erta 'Ale lava lake. (a) A plot of transition depth based on information of gas flux and bubble frequency is shown in black. Three conduit diameters (4, 5, 6, 7 m) are chosen in order to calculate the heat flux at the surface. The transition depths at which bubbles become conduit-filling are determined for each conduit diameter. (b) Lines in different colours show the predicted heat supply at the surface as a function of surface temperature for each chosen diameter. This is calculated using the corresponding z_T for each conduit size, read from panel (a), as the boundary where the temperature starts to drop from $T_{\text{max}} = 1000$ °C. The solid black line shows the calculated heat loss ($\dot{Q}_{\text{rad}} + \dot{Q}_{\text{conv}}$) as a function of surface lake temperature. The dashed and dotted black line show the calculated heat loss as a function of estimated molten lake temperature when including 1 and 2 cm thick conductive solidified crusts, respectively. 105

4.13 Comparison between our model and the field data acquired from Erebus volcano. (a) A plot of transition depth based on information of gas flux and bubble frequency is shown in black. Three conduit diameters (4, 5, 6 m) are chosen in order to calculate the heat flux at the surface. The transition depths at which bubbles become conduit-filling are determined for each conduit diameter. (b) Lines in different colours show the predicted heat supply at the surface as a function of surface temperature for each chosen diameter. This is calculated using the corresponding z_T for each conduit size, read from panel (a), as the boundary where the temperature starts to drop from $T_{\max} = 1000$ °C. The solid black line shows the calculated heat loss ($\dot{Q}_{\text{rad}} + \dot{Q}_{\text{conv}}$) as a function of surface lake temperature. The dotted black line shows the calculated heat loss as a function of estimated molten lake temperature when including a 10 cm thick conductive solidified crust. 108

4.14 Comparison between our model and the field data acquired from Stromboli and Villarica volcanoes. (a, c) plots of transition depth based on information of gas flux and bubble frequency are shown in black. Here we choose the conduit diameters of 2, 2.2, 2.5, 3 m for Stromboli and 2, 2.5, 3 m for Villarica. (b, d) Lines in different colours show the predicted heat supply at the surface as a function of surface temperature for each chosen diameter. This is calculated using the corresponding z_T for each conduit size, read from panel (a,c), as the boundary where the temperature starts to drop from $T_{\max} = 1000$ °C. The solid black line shows the calculated heat loss ($\dot{Q}_{\text{rad}} + \dot{Q}_{\text{conv}}$) as a function of surface lake temperature. At Villarica, (c-d), the solid and dashed lines associated to the calculations based on total and active degassing, respectively. . . 110

4.15 Comparison between our model and the field data acquired from Nyiragongo lava lake. (a) A plot of transition depth based on information of gas flux and bubble frequency is shown coloured lines. The blue, red, yellow and violet curves are associated with chosen bubble occurrence times of 0.5, 1, 2 and 4 hours, respectively. Here we fix the conduit diameter to be 15 m and z_T is predicted for each chosen bubble frequency. (b) Lines in different colours show the predicted heat supply at the surface as a function of surface temperature for each chosen bubble frequency. This is calculated using the corresponding z_T for each conduit size, read from panel (a), as the boundary where the temperature starts to drop from $T_{\max} = 1000$ °C. The solid black line shows the calculated heat loss ($\dot{Q}_{\text{rad}} + \dot{Q}_{\text{conv}}$) as a function of surface lake temperature. The dotted black line shows the calculated heat loss as a function of estimated molten lake temperature when including a 10 cm thick conductive solidified crust. 113

A.1 The ratio between the total measured buoyancy to the expected buoyancy in the case of discrete release gravity currents (chapter 2). Colours represent different experiments as coded in table 2.1. 132

A.2 The ratio between the total measured buoyancy to the expected buoyancy in the case of constant flux gravity currents (chapter 3). Colours represent different experiments as coded in table 3.1. 132

A.3 The normalised volumes detected when different threshold digital numbers are used. The threshold number of ~ 150 is consistent for all the four images corresponding to images taken at t =10, 20, 30 and 40 s. Images are taken from the finite volume release gravity current H. . . . 133

List of tables

2.1 Table of experiments illustrating the range of aspect ratio and dimensions of the lock. a. light attenuation experiment; b. dye injected into head of the flow; c. dye injected into the ambient fluid. Column of colours indicates colours of data shown in subsequent graphs. The quantities t_o, $\mathcal{R}$ and Fr are properties of the current which are defined in section 3.3. In the table, for each experiment, we list the asymptotic values of $\mathcal{R}$ and Fr for $r_n > 3r_o$ (figure 2.5a,b) 32

3.1 Table of experiments illustrating the range of initial volumetric flux and buoyancy used in this study. The quantities Fr_o, $\mathcal{R}_C$ and Fr_n are properties of the current which are defined in section 3.4.1, 3.5.1 and 3.5.2, respectively. In the table, for each experiment, we list the asymptotic values of Fr_n, $\mathcal{R}_o$ for $\hat{t} > 5$. The colour codes given for experiments A-I are used in the subsequent plots in this chapter. 52

4.1 A summary of the bubble period, gas flux and lava lake used in heat balance analysis based on our predicted heat supply due to bubble flows. The condition for a 10 cm solidified crust on top of the lake is included when the heat balance suggests a lake temperature of lower than 700-800 °C. The conduit diameter, d_c, is then predicted based on this analysis for each lava lake. 103

List of symbols

ch. 2	ch. 3	**Mixing in axisymmetric gravity currents**
B		total buoyancy
	B_o	buoyancy flux
Fr	Fr_n	frontal Froude number
	Fr_o	source Froude number
g'	g'	local buoyancy
	g'_j	initial buoyancy
	g'_o	effective source buoyancy
H	H	water depth in the experimental tank
h	h	depth of the currents
h_n	h_n	maximum depth near the front
	h_r	time-averaged depth in the body region
	Q_j	initial volume flux
	Q_o	effective source volume flux
	Q_r	total radial volume flux
	Q_n	radial volume flux supplying the head region
	Ri_g	gradient Richardson number
Re	Re	Reynolds number
r_n	r_n	radial position of the nose
	r_s	radial position of the rear/shock
	u_n	nose velocity
	u_r	depth-averaged velocity in the body region
V	V	total volume
ε		total entrainment coefficient
	ε_n	entrainment coefficient associated with the nose
	ε_b	entrainment coefficient associated with the back of the current
	$\epsilon_{\mathcal{R}}$	error associated with $\mathcal{R}$
$\mathcal{R}$	$\mathcal{R}_{\mathcal{C}}$	ratio between the experimental r_n to the conventional power law
	$\mathcal{R}_{\mathcal{S}}$	ratio between the experimental r_n to the predicted value by Slim & Huppert (2011)'s model
	$\mathcal{R}_{\mathcal{J}}$	ratio between the experimental r_n to the predicted value by Johnson *et al.* (2015)'s model

ch. 4 **Thermodynamics of a lava lake**

A_{lake}	lake surface area
A	conduit cross-sectional area
c	dye concentration
D	diffusion coefficient (dispersivity)
c_g	heat capacity of the gas
c_m	heat capacity of the magma
c_L	latent heat of crystalisation of the magma
d_c	conduit diameter
Eo	Eötvös number
Fr	Froude number
k	thermal conductivity
L	length of a slug unit
L_b	slug length
$\dot{M}$	gas mass flux
$\dot{M}_{\text{magma}}$	magma mass flux
P	pressure
$\dot{Q}$	heat flux
$\dot{Q}_{\text{rad}}$	heat flux by radiation
$\dot{Q}_{\text{conv}}$	heat flux by convection
$\dot{Q}_{\text{cond}}$	heat flux by conduction
$\dot{Q}_{\text{hyd}}$	heat flux by hydrological processes
$\dot{Q}_T$	heat flux from gas phase to liquid magma phase per unit conduit length
$\dot{Q}_{T,s}$	heat flux from gas phase to liquid magma phase by one gas bubble
$\dot{Q}_H$	heat flux through a conductive crust
R	specific gas constant
Re_b	Reynolds number based on the bubble speed
Re_B	Reynolds number based on the buoyancy force
r_b	bubble radius
T_g	gas temperature
T_m	magma temperature
u_o	rise speed of a single gas slug
u_b	rise speed of gas slugs from a continuous gas flux
u_g	superficial gas speed
V_b	bubble volume
$\dot{V}_g$	gas volume flux
z_T	transition depth
β	bubble fraction
δ	boundary layer thickness
κ	thermal diffusivity
μ	dynamic viscosity
ν	kinematic viscosity
ω	bubble frequency
ρ_g	gas density
ρ_m	magma density

Chapter 1

Introduction

This thesis contains an experimental study of two main problems in geophysical fluid dynamics: mixing in gravity currents and two-phase separated flow in a volcanic conduit. We present a new set of laboratory experiments to quantify the mixing process in axisymmetric gravity currents using a light attenuation technique (as shown in chapter 2 and 3). This provides a new understanding of the dilution rate of the currents as they mix with ambient fluid. In chapter 4, we explore the mixing within a volcanic conduit as a result of gas flow. This gives us a novel insight into the role of gas slugs in transporting thermal energy up a volcanic conduit, which is relevant for the long life of lava lakes and for open-vent volcanic systems such as occur at Stromboli volcano.

1.1 Gravity currents

1.1.1 Motivation

Gravity currents, also known as buoyancy or density currents, arise when two fluids of different densities meet. The heavy fluid spreads from its source below the less dense fluid, either generating a planar flow in a confined channel or a radially spreading flow in an unconfined domain. Such flows consist of a head region at the front which displaces the ambient fluid followed by a tail. Gravity currents arise in many environmental flows. Single-phase examples include an onshore breeze initiated by temperature differences between the onshore and offshore air masses and the hypopycnal flow arising when fresh river water enters the saline ocean (see Simpson, 1999).

Fig. 1.1 Photos of (left) a snow avalanche (image from Scientif38 2007, Wikipedia, 15 September 2017) and (right) turbidite deposit at Gorgoglione Flysch, South Italy (image from Geologist 2004, Wikipedia, 15 September 2017).

Multiphase gravity currents may include immiscible fluids of different densities such as in the case of oil spreading on a water surface (Hoult, 1972). Other geological problems concern systems in which the excess density of the fluid is provided by suspended particles. The mixture of interstitial fluid and particles has higher bulk density than the density of the surrounding ambient fluid. The mixture may have locally uniform properties if the volume fraction of solid is small and the particles are well-mixed within the fluid, as is the case for turbulent flows. Due to its high bulk density, such systems can create gravity currents even though the interstitial and the ambient fluid may have the same density. Examples of such a system in nature include volcanic ash flows, turbidity currents in the ocean or snow avalanches (figure 1.1a). Pyroclastic flows are formed as a result of the collapse of a volcanic plume, following an explosive volcanic eruption. The mixture of hot gas and ash provides excess buoyancy compared to the surrounding air which drives a horizontal flow (see Dufek, 2016; Roche *et al.*, 2013). The flow can propagate over long distances and cause destruction along its path such as happened to Pompeii during the eruption of Mount Vesuvius in 79AD. Similarly, turbidity currents, formed as a mixture of submarine sediment and water, can propagate many tens of kilometres along a sea floor and are believed to be the main contributor to sediment transport from a continental shelf to the abyssal plain (Kneller & Buckee, 2000; Meiburg & Kneller, 2010). Turbidity currents triggered by the 1929 Grand Banks Earthquake were responsible for the famous breakage of sub-marine cables (Piper *et al.*, 1988). The deposits from these sediments (figure 1.1b) are important host rocks for oil reservoirs worldwide. As

a result, understanding the mechanisms of sedimentation and the dynamics of the parental flows have become key research topics for the hydrocarbon industry. Snow avalanches, triggered by failure in the snowpack, can be dangerous and destructive. It has also been argued that global warming has contributed to an increase in damage caused by the flows (Ancey & Bain, 2015) and understanding the science of such flows may be useful in mitigating the associated risks.

1.1.2 Modelling gravity currents

Dimensional analysis

If there is a density difference, $\Delta\rho$, between two fluids, the buoyancy, also known as reduced gravity, is denoted by

$$g' = g\Delta\rho/\rho_o, \tag{1.1}$$

where g and ρ_o are the gravitational acceleration and a reference density, respectively. For flows with high Reynolds number, dimensional analysis suggests that the front velocity, $\mathrm{d}r_n/\mathrm{d}t$, can be described as being proportional to the square root of the product of this reduced gravity and the height of the current, h. The proportionality of this expression is commonly known as the Froude number, Fr, and can be expressed as

$$\frac{\mathrm{d}r_n}{\mathrm{d}t} = Fr\sqrt{g'h}. \tag{1.2}$$

This is often interpreted as the relative importance between buoyancy and inertia. For $Re >> 1$, we require that $Fr(g'h)^{1/2}h/\nu >> 1$, where h is the depth and ν is the kinematic viscosity of the flow. The theoretical value of Fr for inviscid flows in a deep ambient was determined to be $\sqrt{2}$ (Benjamin, 1968). In the case that the ambient fluid has a finite depth, Huppert & Simpson (1980) proposed an empirical relation for Fr as a function of the ratio between the depth of the current head and the ambient depth, which can be written as

$$Fr = \begin{cases} \frac{1}{2}\left(\frac{h}{H}\right)^{\frac{1}{3}} & \text{if } 0.075 \leq \frac{h}{H} < 1 \\ 1.19 & \text{if } \frac{h}{H} \leq 0.075 \end{cases}. \tag{1.3}$$

Integral models

Early attempts to describe the dynamics of gravity currents assumed that the current has no mixing with the ambient fluid. As a result, the volume of the current and the density difference between the current and the ambient fluid remain constant as the current evolves. The concept is widely used in box models in which the evolution of the gravity current is viewed as an equal-area transformation of a rectangular shape with time. For axisymmetric gravity currents, the transformation of a cylinder is considered instead. The models can be used to estimate the front location and the height of the currents but the detailed shape cannot be captured by this approach.

Two-dimensional gravity currents

Using a rectangular tank, we first consider gravity currents which are produced following the release of a finite volume dense fluid behind a lock of known size, $A = x_o h_o$. At time t the current may propagate a horizontal distance, $x_n(t)$, and have the height, $h(t)$. If there is no mixing taking place between the current and the ambient fluid, the product of these two length scales must be constant at all time and, therefore, $A = x_o h_o = x_n h$. Substituting this into the equation (1.2) we obtain the relation

$$\frac{\mathrm{d}x_n}{\mathrm{d}t} = Fr\sqrt{\frac{g'A}{x_n}}, \tag{1.4}$$

which can be integrated using the empirical estimate for Fr (equation 1.3). Just after the lock release, equation 1.3 suggests the dependency of Fr on the depth of the current, h_n as it is comparable to the ambient depth. As the current propagates, h_n gradually decreases until it reaches the point where $h_n/H < 0.075$, at which point, Fr becomes constant. The results from the integration of these two stages can be considered separately to give the frontal location as a function of time which can be expressed as

$$x_n = \begin{cases} \left(x_o^{\frac{7}{6}} + \dfrac{7}{12}\left(g'^3 A H^2\right)^{\frac{1}{6}} t \right)^{\frac{6}{7}} & \text{for } x_o \le x_n \le x_s = \dfrac{A}{0.075H} \\ \left(x_o^{\frac{3}{2}} + \dfrac{3}{2} Fr\left(g'A\right)\left(t - t_s\right) \right)^{\frac{2}{3}} & \text{for } x_s \le x_n \end{cases}, \tag{1.5}$$

where t_s is the time at which $x_n = x_s$, the horizontal distance at which the transition occurs. At large time, this can be approximated as

$$x_n \approx \left(\frac{3}{2} Fr (g' A t)\right)^{\frac{2}{3}} \text{for } t \gg t_s. \tag{1.6}$$

Axisymmetric gravity currents

The box model for axisymmetric gravity currents can be derived by considering dense fluid that is released from a cylindrical container. The volume of the dense fluid can be calculated from the volume of the cylinder, $V = \pi r_o^2 h_o = r_n h$, given that r_o is the radius of the cylinder. By comparison with equation (1.2), the speed of the front of axisymmetric non-mixing gravity currents can be written as

$$\frac{\mathrm{d}r_n}{\mathrm{d}t} = Fr \sqrt{\frac{g'V}{\pi r_n^2}}. \tag{1.7}$$

Following the same approach as before, the frontal location of these currents can be expressed as

$$r_n = \begin{cases} \left(r_o^{\frac{4}{3}} + \frac{2}{3} \left(\frac{g'^3 V H^2}{\pi} \right)^{\frac{1}{6}} t \right)^{\frac{3}{4}} & \text{for } r_o \leq r_n \leq r_s = \dfrac{V}{0.15\pi H} \\ \left(r_o^2 + 2Fr \left(\dfrac{g'V}{\pi} \right) (t - t_s) \right)^{\frac{2}{3}} & \text{for } r_s \leq r_n \end{cases}, \tag{1.8}$$

where t_s is the time at which $r_n = r_s$. At large time, this can be approximated as

$$r_n \approx (2Fr)^{\frac{1}{2}} \left(\frac{g'V}{\pi} \right)^{\frac{1}{4}} t^{\frac{1}{2}} \text{for } t \gg t_s. \tag{1.9}$$

One may substitute Fr=1.19 into equations (1.5), (1.6), (1.8) and (1.9), as suggested by Huppert & Simpson (1980). This model is in agreement with the scaling model proposed by Hoult (1972) based on experimental observations.

Assuming that the entrainment is negligible, the buoyancy and volume of the current remains constant over time. However, experiments have shown that the density and volume of gravity currents change significantly with time due to entrainment. Nonetheless, the box models can still provide a reliable estimate for the frontal location of the gravity currents. This might be because of the fact that the expression in equations (1.6) and (1.9) appears as the product of buoyancy and volume of the

currents, i.e. the total buoyancy, which is a conserved quantity. Entrainment causes a reduction in reduced gravity, due to dilution, but, in the meantime, the volume of the current increases as ambient fluid is mixed into the flow.

Shallow water model

A more complex model put forward to describe the dynamics of gravity currents are the shallow-water, or depth-averaged models. The shallow water equations assume that the vertical length scale is insignificant compared to the horizontal length scale of the flow; hence, the flow is described in terms of vertically averaged quantities. As the flow spreads out, the aspect ratio, h/x_n (or h/r_n in axisymmetric currents), becomes very small even if the current was released from a lock of a very high aspect ratio. The shallow water equations provide a set of depth-averaged equations that describe the height and horizontal velocity of the flow as a function of horizontal position and time.

Rottman & Simpson (1983) first applied the shallow water approximation to conventional saline gravity currents. The models were later extended to sediment-laden currents by Bonnecaze *et al.* (1995). The shallow-water approach assumes the flow is purely driven by inertia while vertical accelerations are negligible. In addition, the current is assumed to be highly turbulent and well mixed. This means that the suspended particles within the current have uniform volume fraction across the depth of the current. This approximation holds for fine sediments which can be suspended but becomes less accurate in the case of sediments with a coarser grain size.

A simple version of this shallow-water model called the single-layer system assumes further that the depth of current is much shallower than the depth of the overlaying ambient fluid and thus is not affected by it. However, when the ambient fluid is not sufficiently deep, the motions of the overlying ambient may influence the flow of the gravity current. In this case, a more complicated system, the two-layer system, is applied instead.

Considering the single-layer system, where the depth of the ambient fluid is assumed to be infinite, the depth-averaged continuity equation and the horizontal momentum equation can be written as

$$\frac{\partial h}{\partial t} + \frac{\partial (uh)}{\partial t} = 0, \tag{1.10a}$$

$$\frac{\partial u}{\partial t} + u\frac{\partial u}{\partial x} + g'\frac{\partial h}{\partial x} = 0. \tag{1.10b}$$

The Froude number condition at the front, $\mathrm{d}x_n = Fr\sqrt{g'h_f}$, is applied at the front location, x_f, where h_f is the height of the current near the front. The equivalent set of equations for axisymmetric currents are

$$\frac{\partial h}{\partial t} + \frac{1}{r}\frac{\partial (uh)}{\partial t} = 0, \tag{1.11a}$$

$$\frac{\partial u}{\partial t} + u\frac{\partial u}{\partial r} + g'\frac{\partial h}{\partial r} = 0. \tag{1.11b}$$

In order to solve this system, we may apply the initial condition:

$$h(x, t=0) = \begin{cases} h_o; & 0 \leq x \leq x_o, \\ 0; & x_o \leq x. \end{cases} \tag{1.12}$$

together with the no-flow boundary condition at $x = 0$:

$$\frac{\partial h}{\partial x}|_{x=0} = 0; \quad \text{and} \tag{1.13}$$

$$u(x = 0, t) = 0. \tag{1.14}$$

These conditions are also the same in the axisymmeric case except that they are applied at $r = 0$ rather than $x = 0$. The solution of these partial differential equations was first demonstrated by (Hoult, 1972). The equations admit similarity solutions in terms of a similarity variable, given by

$$\eta = \begin{cases} (g'A)^{-\frac{1}{3}} x t^{-\frac{2}{3}}; & \text{for planar currents,} \\ (g'V)^{-\frac{1}{4}} x t^{-\frac{1}{2}}; & \text{for axisymmetric currents.} \end{cases} \tag{1.15}$$

At the front, the similarity variable can be writen as the function of Froude number. This is given as

$$\eta_f = \begin{cases} \left(\dfrac{27Fr^2}{12 - 2Fr^2}\right)^{\frac{1}{3}}; & \text{for planar currents,} \\ \left(\dfrac{16Fr^2}{\pi(4 - Fr^2)}\right)^{\frac{1}{3}}; & \text{for axisymmetric currents.} \end{cases} \tag{1.16}$$

The solutions for the height and velocity profiles are then given by

$$h(\eta) = \frac{A}{x}\eta\left(\frac{1}{9}\eta^2 + \eta_f^{-1} - \frac{1}{27}\eta_f^2\right) \quad \text{and} \quad u(x,t) = \frac{2x}{3t}$$
$$\text{for planar currents,} \tag{1.17}$$

$$h(\eta) = \frac{V}{8r^2}\eta^2\left(\eta^2 + \left(\frac{2-Fr^2}{Fr^2}\right)\eta_f^2\right) \quad \text{and} \quad u(r,t) = \frac{r}{3t}$$
$$\text{for axisymmetric currents.} \tag{1.18}$$

This single-layer shallow water models can also determine the front location of the currents. It is given by

$$x_f(t) = \eta_f(g'A)^{\frac{1}{3}}t^{\frac{2}{3}}, \tag{1.19}$$

$$r_f(t) = \eta_f(g'V)^{\frac{1}{4}}t^{\frac{1}{2}}. \tag{1.20}$$

We can compare these results with the results suggested by the box models discussed earlier. Comparing equations (1.19) and (1.20) with equations (1.6) and (1.9) shows that both models suggest that the long-time front location increases as $t^{\frac{2}{3}}$ and $t^{\frac{1}{2}}$ for planar and axisymmetric currents, respectively. The coefficients suggested by the two models are, however, slightly different.

Although these modelling approaches have provided a useful insight into the dynamics of gravity currents, they assume that the density of the current is unchanged during the evolution of the flow. This is not the case for many geophysical flows. In fact, the density of the currents is found to be reduced as the ambient fluid is entrained and mixed into the currents during their propagation (Hacker *et al.*, 1996; Hallworth *et al.*, 1996; Sher & Woods, 2015). In order to predict the evolution of gravity currents, a model including the mixing of ambient fluid into the current is required. Here we explore the mixing of ambient fluid into axisymmetric currents. This work complements the parallel study of two-dimensional gravity currents by Sher & Woods (2015, 2017).

1.1.3 Entrainment in a turbulent plume

Entrainment of ambient fluid into a turbulent flow has long been observed and investigated more thoroughly in the case of vertical turbulent flows, known as plumes, in comparison to the case of horizontal flows (gravity currents). Reviewing how en-

trainment has been investigated and modelled in these vertical flows can be useful to extend the similar approach to cover the study in gravity currents. Plumes are vertical turbulent flows that arise from localised sources that are driven by buoyancy contrast between the source fluid and the ambient. In contrast, vertical flows that are driven by the initial momentum of the source fluid are referred to as jets (Turner, 1979). Examples of these vertical turbulent flows include volcanic plumes in the atmosphere upon volcanic eruptions, hydrothermal plumes on the sea floor, etc. One of the pioneering works includes the analysis by (Morton *et al.*, 1956) where they recognised a quasi-steady state of such flows. It is observed that the dynamics of the flows, averaged over a long time scale, can be represented in terms of horizontally-averaged mass, Q, momentum, M, and buoyancy, B, fluxes. This can be summarised in the forms:

$$Q = 2\pi \int r\rho v \mathrm{d}r, \quad M = 2\pi \int r\rho v^2 \mathrm{d}r \quad \text{and} \quad B = 2\pi \int r g' v \mathrm{d}r \tag{1.21}$$

where $v(r, z)$ and $\rho(r, z)$ are the vertical velocity and density of the fluid as a function of the vertical position, z, and the radial position, r of the plumes. Here the equation for the buoyancy conservation is required in order to account for the varying buoyancy due to mixing with the ambient fluid (cf. 1.10). Recall here that g' is the local buoyancy arising from density contrast between the dense plume and the ambient fluid (1.1). In the limit where the density change is small compared to the background density, we can write the dynamics of the plumes in terms of specific mass, q, momentum, m and buoyancy, f, fluxes at different heights, z, as

$$q(z) = b^2 \bar{v}, \quad m(z) = b^2 \bar{v}^2 \quad \text{and} \quad f(z) = \overline{g'} b^2 \bar{v} \tag{1.22}$$

where b is the effective radius of the plume, $\bar{v}$ is the horizontally-averaged vertical speed and $\overline{g'}$ is the horizontally-averaged buoyancy. Assuming that fluids are incompressible and the density contrast between the two fluids is small, we may apply the Boussinesq approximation, which assumes that the relative density variations are sufficiently small that they are only dynamically significant in the buoyancy force. The engulfment of ambient fluid parcels due to turbulent eddies causes mixing between the ambient fluid and the fluid within the plumes. As a result, the mass flux increases with height as more fluid is entrained into the plume. On time scales long enough compared to the eddy-turnover time, we only consider the mean horizontal inflow velocity of ambient fluid that becomes incorporated into the plume, u_{ent}. This is proportional to the

vertical speed of the plume and can be written as

$$u_{\text{ent}} = \varepsilon \bar{v}(z) \tag{1.23}$$

where ε is the entrainment coefficient. Considering the changes in mass, momentum and buoyancy as the fluid travels up the plumes, the conservation relations of mass, momentum and buoyancy can be written as

$$\frac{\mathrm{d}q}{\mathrm{d}z} = 2\varepsilon b\bar{v} \qquad = 2\varepsilon m^{1/2}, \tag{1.24}$$

$$\frac{\mathrm{d}m}{\mathrm{d}z} = \overline{g'}b^2 \qquad = \frac{\overline{g'}q^2}{m}, \tag{1.25}$$

$$\frac{\mathrm{d}f}{\mathrm{d}z} = \frac{\mathrm{d}}{\mathrm{d}z}\left(\overline{g'}b^2\bar{v}\right) = -N^2 q, \tag{1.26}$$

where $N^2 = -\dfrac{g}{\rho_{\text{a}}}\dfrac{\mathrm{d}\rho_{\text{a}}}{\mathrm{d}z}$ represents the ambient stratification arisen due to decrease in ambient density, ρ_{a}, with increasing height, z. For a uniform ambient density ($N = 0$), the buoyancy flux remains constant and equal to the source flux. These equations have a similarity solution that can be written as

$$q = \left(\frac{6\varepsilon}{5}\right)\left(\frac{9\varepsilon}{10}\right)^{1/3} f_o^{1/3} z^{5/3}, \tag{1.27}$$

$$m = \left(\frac{9\varepsilon}{10}\right)^{2/3} f_o^{2/3} z^{4/3}, \tag{1.28}$$

$$f = f_o, \tag{1.29}$$

where f_o is the source buoyancy flux. Laboratory experiments have been conducted in order to determine the entrainment coefficient, ε. This has been determined to be within the range of 0.10 to 0.16 for plumes and 0.065 to 0.080 for jets as has been summarised by (Carazzo *et al.*, 2006), based on a top hat velocity profile (velocity is constant at a given height within the flow and is zero everywhere outside the flow).

1.1.4 Entrainment in a gravity current

By analogy to the entrainment hypothesis developed for plumes (1.23), the entrainment hypothesis can also be written in terms of the volume flux for a planar and an

axisymmetric gravity current as

$$\frac{\mathrm{d}(\overline{u}h)}{\mathrm{d}x} = \varepsilon\overline{u} \quad \text{and} \quad \frac{\mathrm{d}(\overline{u}hr)}{\mathrm{d}r} = \varepsilon\overline{u}r, \tag{1.30}$$

respectively, where $\overline{u}$ is the depth-averaged streamwise velocity. Motivated by the early work on entrainment of ambient fluid in plumes and jets, Ellison & Turner (1959) conducted an experiment on mixing in a gravity current travelling down an inclined slope. The entrainment coefficient has been proposed to follow an empirical relationship

$$\varepsilon = \frac{0.08 - 0.1Ri}{1 + 5Ri} \quad \text{for} \quad Ri \leq 0.8, \tag{1.31}$$

where Ri is known as the Richardson number which is a non-dimensional number that compares the stability of buoyancy stratification to the shear velocity of the current. This is in the form

$$Ri = \frac{g\,(\Delta\rho/\rho)}{u^2/h}\cos\alpha, \tag{1.32}$$

where α is the angle of an inclined slope. Based on experimental studies in currents, both saline and sediment-laden currents, several other empirical formulae relating Ri to the mixing coefficients have been proposed. Many of these appear to suggest that entrainment in the case of horizontal flows is very small. However, Princevac *et al.* (2005) studied katabatic flows and found that in the field data, ε appears to be larger than those values predicted by laboratory-based experiments. They also commented that the experimental study by Ellison & Turner (1959) was conducted at low Re number which could lead to underestimates of the mixing when being used to describe field-scaled turbulent flows with large Re.

In addition to the entrainment along the back of the gravity current which is the result of shear instability across the top boundary of the gravity current, entrainment of the ambient fluid into the head of a gravity current was reported by Prandtl (1952). Following this finding, several experimental studies have demonstrated the dilution and volume increase as the flow propagates, confirming the mixing between the currents and the ambient fluid. In order to quantify the amount of mixing in a gravity current, Hallworth *et al.* (1996, 1993) used a neutralisation technique by which an alkaline gravity current intrudes into acidic ambient fluid along the bottom boundary and a

universal indicator was added to the current. The universal indicator changes colour owing to the mixing and the time at which the neutralisation happens was determined.

The span-wise averaged density field within the current was determined by Hacker *et al.* (1996) using a light attenuation technique. This technique allows estimates of the volume of the current and also the dilution of the current as a function of distance from the source. Marino *et al.* (2005) and Sher & Woods (2015) applied the technique to measure the depth-averaged density profiles in saline currents propagating along a channel to see how they change over time.

Since the pioneering studies of entrainment in gravity currents by Ellison & Turner (1959), a number of experiments have been carried out (Britter & Simpson, 1978; Varjavand *et al.*, 2015) to quantify the entrainment of ambient liquid into a steady gravity current. For these currents, the mixing has been focussed on the mixing at the back of the currents and described to be the result of shear instability across the top boundary of the gravity current. Experimental studies on entrainment have mostly been performed to investigate planar gravity currents, while there are relatively fewer experiments investigating mixing in axisymmetric gravity currents. The main purpose of this study, therefore, is to develop a new experimental technique to understand the mechanisms of mixing and to quantify the amount of entrainment in the case of axisymmetric gravity currents.

1.1.5 Research outline

Although the flow and mixing behind the head of a gravity current has been modelled both experimentally and theoretically, the impact of entrainment due to ambient fluid being displaced by the propagating front has not been considered. Our experimental study presented in **chapter 2** focuses on the mixing in the head region of the flow as well as the associated impacts of this mixing on the flow dynamics in a finite volume axisymmetric gravity current. The current develops following release of a dense fluid initially located behind a lock gate. The width of the tank increases in the downstream direction from the lock gate, resembling a wedge shape. Using this apparatus, a side view of a sector of an axisymmetric gravity current can be examined. The light attenuation technique is applied to a systematic series of experiments to measure the evolution of the dilution of a dye tracer due to mixing with colourless ambient fluid. Digital images of the flows allow us to quantify the amount of light being absorbed by the dye which can be mapped back to the actual concentration of dye tracers. Calibration curves determining the correlation between the dye concentration and the

light intensity can be made based on light intensity images of the tank filled with fluid of known concentration. Since the width of the experimental tank varies, the light intensity can be different from place to place even when the tank is filled with a homogeneous dye concentration. In this case calibration curves must be determined locally. Once the dye concentration is known, the amount of dilution can be determined and this allows us to convert back to the span-wise averaged buoyancy, g', of the evolving flow.

In addition to the dye attenuation measurements, we performed additional dye studies by injecting different colours of dye into different parts of the flows. This visualises the motion of fluid within the current and illustrates the mechanisms of the entrainment of ambient fluid. Together with the results from light attenuation technique, we show that there is a substantial amount of ambient fluid which mixes into the current. By measuring the volume change of the current with time, we calculate a mixing coefficient representing the effectiveness the mixing of ambient fluid into the current. Later in the chapter, we derive self-similar solutions that include the mixing at the nose of the currents.

In **chapter 3** we use the same experimental techniques to study the mixing in high Reynolds number axisymmetric gravity currents initiated from a steady flux of dense fluid. For these currents, a steady tail region is observed behind the head of the currents. In addition to the technique used in the study of finite volume gravity currents presented in chapter 2, we track the speed of structures within the tail region and interpret this as the speed of the successive eddies within the currents. The estimated speed of fluid within the current provides crucial information for quantifying the mixing along the top boundary of the current. Based on these results, we measure the volume change of the current with time and calculate the mixing coefficient associated with entrainment at the nose. We then compare our experimental results to the theoretical model proposed by (Johnson *et al.*, 2015).

After some work has been conducted on gravity currents, we have decided to apply the light-attenuation technique to investigate another geophysical problem in nature, demonstrating that the light-attenuation technique is an important and useful method that can be used to study various geophysical fluid-mixing problems. The other section of this thesis investigates the role of gas bubbles in mixing the liquid magma within a volcanic conduit which we propose to be a potential mechanism that can transfer sufficient heat from subsurface magma chamber towards the top of the conduits.

Fig. 1.2 Photos of lava lakes at (left) Marum crater, Ambrym, Vanautu (image from Cai Tjeen Willink 2011, Wikipedia, 15 September 2017) and (right) Nyiragongo, Congo (image from Geophile71 2009, Wikipedia, 15 September 2017).

1.2 Heat supply to lava lakes

1.2.1 Motivation

Lava lakes are a rare feature on Earth characterised by a large body of molten lava, usually basaltic, being confined within a crater or broad depression (US Geological Survey, 2016). Many lava lakes persist over tens of years and remain molten. This is believed to be caused by the interaction between the surface lava and the subsurface magma chamber. One conceptual model requires large-scale convection driven by a density contrast between the the lake and a magma chamber, which may be caused by the combination of cooling, crystallisation or degassing of melts in the upper portion of the system (Francis *et al.*, 1993; Kazahaya *et al.*, 1994; Stevenson & Blake, 1998).

The lake level is known to fluctuate over different time scales. Small-scale cyclic fluctuation was reported for Erebus (Oppenheimer *et al.*, 2009), Erta 'Ale (Spampinato *et al.*, 2008; Vergniolle & Bouche, 2016) and Nyiragongo (Spampinato *et al.*, 2013). Lava lakes sometimes exhibit episodic cycles of drainage and recharge as reported at Nyiragongo (Burgi *et al.*, 2014; Tazieff, 1994), for example.

The surface of lava lakes often consists of a mosaic of solidified plates separated by incandescent cracks that expose hot molten lava underneath (figure 1.2b). Gas plumes are also observed along these cracks. The mosaic plates may be stationary or slowly drift towards the rim at velocities of order 0.1 m s^{-1} (Calkins *et al.*, 2008; Patrick *et al.*, 2016).

The conceptual model of a magmatic exchange flow (the convection) within the conduit explains some of these features reported for lava lakes. However, it usually considers the gas phase within the conduit to flow homogeneously with the magma, at least until the very top part of the convective cell. Here massive additional volatile exsolution due to decompression reduces the bulk density of the melt and causes the degassed melts to sink back down the conduit. On the other hand, there have been reports of large gas bubbles bursting at the surface of the lake. These bubbles are believed to originate from a deeper level, and possibly from the magma chamber. These large bubbles are likely to rise independently of the basaltic melts and will disrupt the homogeneous exchange flow in the upper few hundred metres of the conduit. There is therefore a challenge about the nature of the flow and heat transfer in the upper part of the conduit.

1.2.2 Heat loss at a lava lake

In this section, we review the heat budget to estimate the total heat loss at a lava lake system. The heat loss is balanced by the thermal supply from the underlying hot magma system. If this is assumed to occur through an exchange flow convective system, then the product of the magnitude of the exchange flow and the cooling near the surface can be assessed (Francis *et al.*, 1993; Harris *et al.*, 1999; Harris & Stevenson, 1997; Le Guern *et al.*, 1979; Spampinato *et al.*, 2013). However, in the upper part of the conduit, this exchange flow may not operate as effectively, and the heat transfer may be controlled by the mixing produced by the bubbles, as we propose later in the chapter. We now review the modes of heat loss from the lake to assess the magnitude of this heat flux.

Radiative heat flux ($\dot{Q}_{\text{rad}}$)

At the surface of a lava lake, heat may be lost to the atmosphere by radiation. This heat flux can be calculated by the relationship:

$$\dot{Q}_{\text{rad}} = A_{\text{lake}} \sigma \varepsilon \left(\Sigma f_i T_i^4 \right), \tag{1.33}$$

where A_{lake} is the surface area of the lake, σ is the Stefan-Boltzmann constant, ε is emissivity and f_i is the fractional area of material at a brightness temperature of T_i. The quantity $T_e = \sqrt[4]{\Sigma f_i T_i^4}$ is known as the effective temperature which may be used as the representative temperature of the lava lake surface.

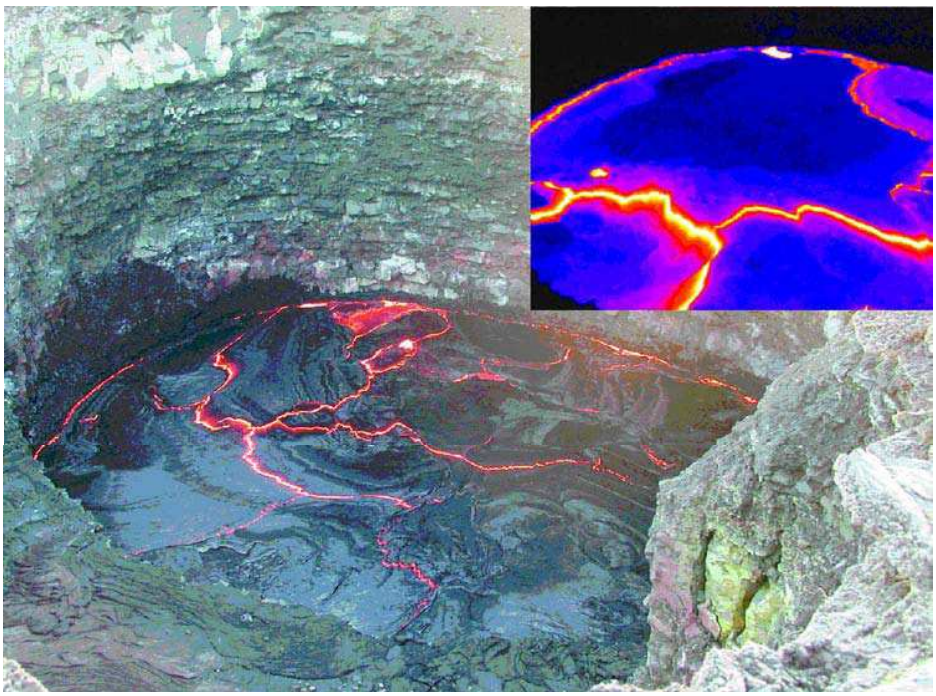

Fig. 1.3 A digital image of Erta 'Ale lava lake taken in February 2001 showing a moderately active surface. Several incandescent cracks in between solidified crusts can be observed. Inset shows a thermal image obtained from the same location but taken 15 mins earlier. The figure is taken from Oppenheimer & Yirgu (2002).

The detailed temperature distributions over the lava surface can be captured by various techniques varying from ground-based instruments (Calkins *et al.*, 2008; Oppenheimer & Yirgu, 2002; Spampinato *et al.*, 2013, 2008) to thermal remote sensing (Harris *et al.*, 1999; Harris & Stevenson, 1997; Wright & Flynn, 2004). Ground-based measurements such as tripod mounted thermal cameras may provide better spatial resolution (figure 1.3). Satellite based thermal observations, on the other hand, provide regularly captured images but with lower spatial resolution. They may also include errors owing to solar reflection during day time and clouds in some weather conditions.

Convective heat flux ($\dot{Q}_{\text{conv}}$)

Temperature differences between the lava surface and the air can drive some convection of the cold air above the hot lava surface which can carry away additional heat from the lava lake. However, this form of heat loss depends heavily on the wind speed and surface roughness. Nonetheless, though the wind speed data is available in their studies, Spampinato *et al.* (2013), believed that free convection is more appropriate in their study as the lava lake of interest (Nyiragongo) was not directly exposed to

the wind since the surface was located 500 m below the crater rim. The heat loss by convection of air with temperature T_{air} over a rigid boundary of temperature T_s of surface area A_{lake} is

$$\dot{Q}_{\text{conv}} = A_{\text{lake}} h \left(T_s - T_{\text{air}}\right), \tag{1.34}$$

where h is the heat transfer coefficient of the air. The value of $h = 10$ $\text{Wm}^{-2}\text{K}^{-1}$ for free convection was used in the calculation by Spampinato *et al.* (2013) while Harris & Stevenson (1997) and Harris *et al.* (1999) used a different approach where h can be defined through the Nusselt number, Nu, the thermal conductivity of fluid, k, and the length scale of convection the thickness of the thermal boundary layer, L,

$$h = Nu\frac{k}{L}. \tag{1.35}$$

Using the definition of Nu for turbulent flow, the equation for $\dot{Q}_{\text{conv}}$ can be written as

$$\dot{Q}_{\text{conv}} = 0.14 A_{\text{lake}} k_{\text{air}} \left(\frac{g\alpha_{\text{air}}\rho_{\text{air}}}{\mu_{\text{air}}\kappa_{\text{air}}}\right)^{\frac{1}{3}} \left(T_s - T_{\text{air}}\right)^{\frac{4}{3}}, \tag{1.36}$$

where g is the gravitational acceleration. Parameters α_{air}, ρ_{air}, μ_{air} and κ_{air} are the expansivity, density, dynamic viscosity and thermal diffusivity of air which may vary slightly depending on temperature and pressure. For air at 25 °C, the parameters $k_{\text{air}}, \alpha_{\text{air}}, \rho_{\text{air}}, \mu_{\text{air}}$ and κ_{air} have values 2.43×10^{-2} $\text{Wm}^{-1}\text{K}^{-1}$, 3.67×10^{-3} K^{-1}, 1.293 kg m^{-3}, 1.72×10^{-5} Pa s and 1.90×10^{-5} m^2s^{-1}, respectively. As a simple estimate, Wright & Flynn (2004) suggested that this heat budget may be equivalent to 30-75% of the corresponding heat loss by radiation based on previous theoretical (Head & Wilson, 1986; Neri, 1998) and field studies (Harris *et al.*, 1999; Oppenheimer & Yirgu, 2002; Spampinato *et al.*, 2013; Wooster *et al.*, 1997).

Conductive heat flux ($\dot{Q}_{\text{cond}}$)

In addition to heat loss at the surface of lava lake via radiation and convection, heat may be lost to the surrounding host rock by conduction. The radial heat flux from a cylinder is given by

$$\dot{Q}_{\text{cond}} = -kA_r\frac{\mathrm{d}T}{\mathrm{d}r} = -2\pi r L k_r \frac{\mathrm{d}T}{\mathrm{d}r} \tag{1.37}$$

where k is the thermal conductivity and A_r is the surface area of a cylinder which depends on the length, L, and radius, r. The equation can be rearranged and integrated to estimate the heat flux associated with heat conduction at a volcanic conduit. Harris & Stevenson (1997) estimated the heat loss by this process at Stromboli and Vulcano (open-vent volcanos) using the equation in the form

$$\dot{Q}_{\text{cond}} = 2\pi k_r L \frac{T_m - T_r}{\ln\left(r_\infty / r_c\right)}, \tag{1.38}$$

where k_r and L, are thermal conductivity of the host rock and magma depth, respectively. $T_m - T_r$ is the temperature contrast between the magma in the conduit and the host rock. r_c is the conduit radius and r_∞ is the radius at the point where the temperature falls to T_r. Assuming the temperature falls to 100 °C 150 m away from the conduit centre (cf. Harris & Stevenson, 1997), the heat loss at the conduit wall for a conduit size of $r_c = 2$ m and 1 km long filled with 1000 °C magma would be of the order of a few MW.

At a lava lake system, the conductive heat loss to the host rock may occur at both the floor of the lake and the walls of volcanic conduit. However, heat loss by the radiation and convection at the lava lake surface are typically on the order of 10-1000 MW due to large surface area of the lava lake. Most previous estimates have assumed $\dot{Q}_{\text{cond}}$ to be negligible and that the lake is well insulated on these boundaries (Spampinato *et al.*, 2013).

Losses due to hydrological processes ($\dot{Q}_{\text{hyd}}$)

When analysing the thermal budget in lava flow, Wooster *et al.* (1997) suggested that heat exchange may happen due to interaction with subsurface water and also the precipitation. Water can be heated up by hot magma and transported away or even vaporised. However, this process is relatively small compared to heat loss by other means (Wooster *et al.*, 1997).

1.2.3 Heat supply by magma convection

The different mechanisms of heat loss mentioned above (§1.2.2) imply that the system continuously loses heat with time. However, lava lakes often persist over many years or tens of years. One explanation is that heat is supplied by magma convection in the volcanic plumbing system; hot magma migrates and carries heat up the conduit,

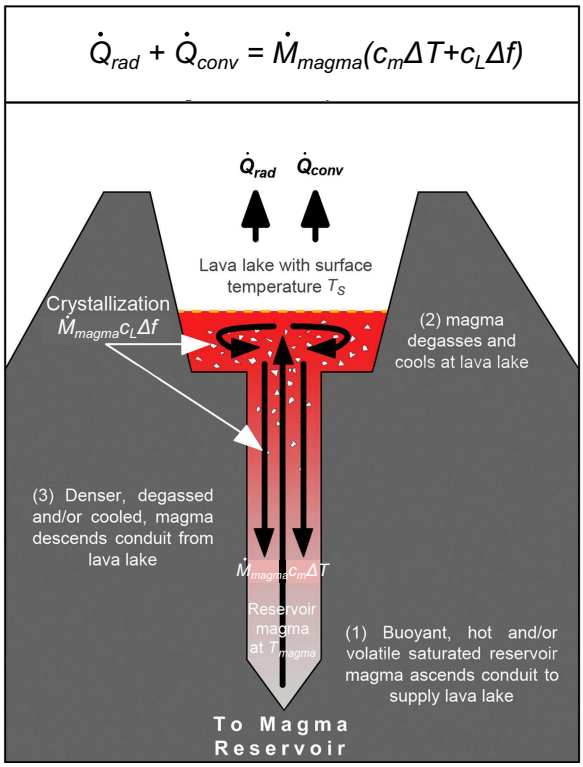

Fig. 1.4 A generic thermal and mass balance model based on magma convection (taken from Harris *et al.*, 1999, relabelled based on our notations). The model implies exchange flow within the conduit and replenishment of magma in the lake. The total heat loss at the surface of the lava lake ($\dot{Q}_{\rm rad} + \dot{Q}_{\rm conv}$) can be balanced by cooling ($\dot{M}_{\rm magma} c_m \Delta T$) and crystallising fresh magma ($\dot{M}_{\rm magma} c_L \Delta f$) arriving at the lake due to the exchange flow.

releases some heat and volatile gases at shallow level and sinks back down as it is cooled and becomes denser. In addition to cooling down, magma may also crystallise which acts as an extra heat source at shallow levels.

Previous studies (Harris *et al.*, 1999; Harris & Stevenson, 1997; Le Guern, 1987; Spampinato *et al.*, 2013) have appealed to a convective exchange flow to estimate the flux of magma in the conduit by balancing the total heat loss to the minimum magma flux, $\dot{M}_{\rm magma}$, required to sustain the system via magma cooling ΔT and crystallisation of a fraction Δf of the melt,

$$\Sigma \dot{Q} = \dot{M}_{\rm magma} \left(c_m \Delta T + c_L \Delta f \right), \tag{1.39}$$

where c_m and c_L are heat capacity and latent heat of crystalisation of liquid magma respectively. The heat balance analysis is summarised in figure 1.4.

The magma temperature should remain above the solidus, the critical temperature below which magma is entirely solid, in order to maintain the fluid-like flow. Using this argument, Harris *et al.* (1999) chose $\Delta T = 150 - 200°C$ and set $\Delta f = 0.3 - 0.45, 0.29$ and 0.023 for the lava lakes at Erebus, Erta 'Ale and Pu'u 'Ō'ō , respectively, based on mass fractions of phenocrysts and microphenocrysts in rock samples determined from previous petrological work (Bizouard *et al.*, 1980; Dunbar *et al.*, 1994; Garcia *et al.*, 1992; Kyle, 1977).

In the absence of these constraints, some previous works considered two end-member scenarios describing endogeneous growth of volcanoes. The first model considers that degassed magma intrudes as dykes suggesting a slight cooling down of magma by 50 °C and that it experiences 25% crystallisation while the second considers the formation of cumulates within the magma chamber, suggesting a cooling by up to 400 °C and complete crystallisation (Francis *et al.*, 1993; Spampinato *et al.*, 2013; Wright & Pilger, 2008). However, investigating CO_2-H_2O ratios in melt inclusions, believed to entrap original magma at the pressure at which the rock is formed, Witham (2011) showed that magma is more likely to be recycled or mixed within the conduit rather than forming intrusions.

Laboratory experiments for low *Re* exchange flows confirmed that such convection is possible (Beckett *et al.*, 2011; Huppert & Hallworth, 2007; Stevenson & Blake, 1998) although some mixing between the descending and ascending flows within the conduit has been observed for miscible fluid of low to intermediate viscosity, (Huppert & Hallworth, 2007). If sufficient mixing occurs, this will reduce the convective flux and may eliminate the density contrast required to drive the bidirectional flow (Witham, 2011).

It is unclear where the top of the conduit convective cell occurs. Most studies assume that convection might extend to within the lava lake region since horizontal motion of magma has been observed at the surface (Harris, 2008). By studying the temporal change in surface motion at Halema'uma'u lava lake, Patrick *et al.* (2016) commented that it is possible that observable surface motion is dependent on deeper lake circulation even though the up-welling from deeper in the lake, and possibly the conduit, acts as the source for such observable flow. The schematic representation for this model is shown in figure 1.5a.

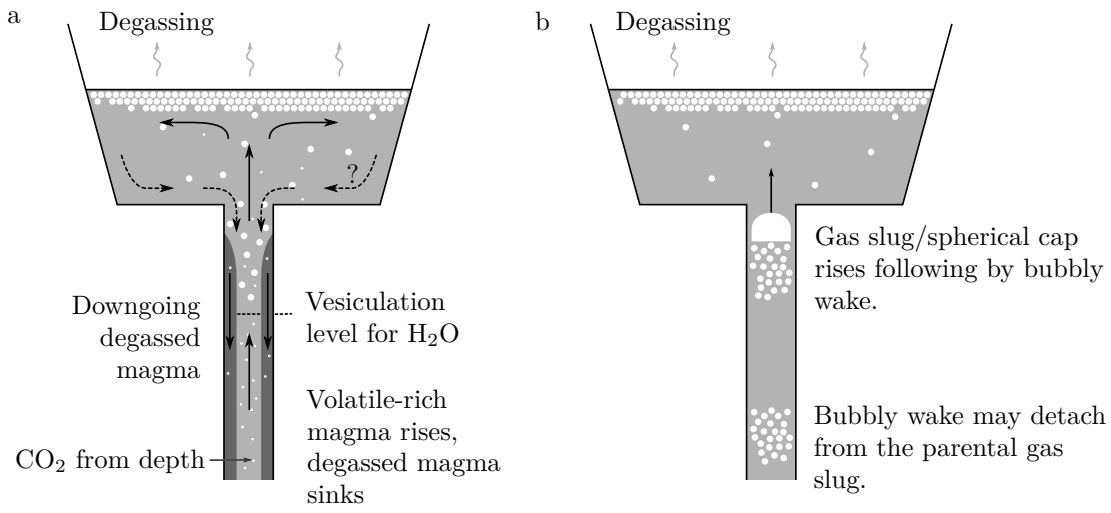

Fig. 1.5 Diagrams showing models for (a) bi-directional flow (adapted from Stevenson & Blake (1998)) and (b) bubble rising in the conduit (adapted from Bouche *et al.* (2010)). For the bi-directional flow model, it might be unclear where the overturn actually occurs. Some authors believed that the overturn may happen within the lava lake as inferred from horizontal motion at the surface.

1.2.4 Heat supply by gas bubbles

The conventional bi-directional flow assumes bubbles are suspended within magma and move along with the magma convection. This assumption is relevant especially if the gas bubbles are sufficiently small. However, as bubbles grow either by exsolusion or decompression, the bubble size can reach a point at which the slip speed of the bubbles relative to the liquid magma is sufficient that bubbles separate from the liquid magma. Bouche *et al.* (2010) suggested from their acoustic study at Erta 'Ale that due to the high Reynolds number of these large bubbles, they form unstable, turbulent, bubbly wakes. They related the arrival of this bubbly magma to the observation of a magma fountain at the surface. They also proposed that the periodic arrival of these hot bubbly pulses of magma is the mechanism that brings up the heat from depth and keeps it in molten state (figure 1.5b). However, the actual thermal energy carried with the bubbles has not been quantified.

The source depth of these large bubbles is not fully constrained by data. The model for heat being supplied by a large gas slug is compatible with the conventional bi-directional flows if the slugs form at shallow level. This might be true at Stromboli where geophysical signals show a seismic and acoustic source at ∼250 m below the

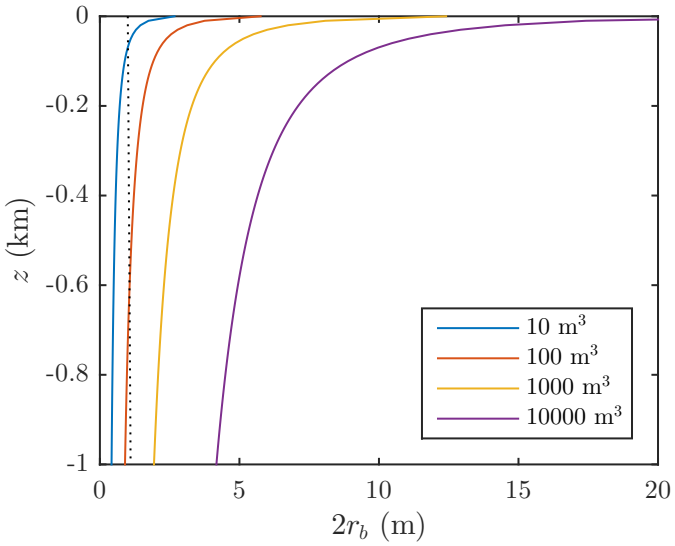

Fig. 1.6 A plot for predicted bubble diameter, $2r_b$, at different depths based on the bubble volume observed at the surface within the range 10-1000 m^3. The calculation assumes the bubbles are spherical and are compressed at depth due to magmastatic pressure. The dotted line illustrates that for a given conduit size of 4 m, a 10 m^3 (volume at the surface) bubble would be conduit-filling in the top 100 m. Bubbles with larger mass would become conduit-filling at a deeper level.

vents (Ripepe *et al.*, 2002; Vergniolle & Brandeis, 1996). However, gas composition analysis during the periodic Strombolian explosions, believed to be the result of gas slugs, revealed the bubble source as deep as 3 km while the shallow source for geophysical signals was argued to be the result of a permanent structural discontinuity that modifies flow pattern of gas slugs (Burton *et al.*, 2007). Provided that gas slugs do form at deep level, bi-directional flows will be disturbed, stirred and potentially erased. Considering the typical bubble frequency observed at the surface at Stromboli, this leaves only $\approx$ 15 minutes for the convection to be restored before the whole system is disturbed again by the next arriving bubble (Vergniolle & Gaudemer, 2015).

The volume of large gas bubbles at the lake surface determined from acoustic study of gas bursting is reported to range from 36-700 m^3 at Erta 'Ale (Bouche *et al.*, 2010) and 1000-24000 m^3 at Erebus (Johnson *et al.*, 2008). Assuming magmastatic pressure,

$$P = P_o - \rho_m g z, \tag{1.40}$$

where ρ_m is the magma density, g is the gravitational acceleration, z is the depth and P_o is the reference pressure at $z = 0$. If the temperature is approximately unchanged as a bubble travels up the conduit, Boyle's law suggests that $P \propto 1/V$, where $V = (4/3)\pi r_b^3$ is the volume of a spherical bubble of radius r_b. figure 1.6 shows the estimated diameter for a spherical bubble at different depths for a bubble of volume 10 - 10^4 m^3 observed at the surface. The diameter of the volcanic conduit is unknown at many lava lakes but is possibly within the range of 2 m, as reported for Stromboli (Vergniolle & Brandeis, 1996), to 15 m as estimated at Nyiragongo, based on the lava draining time for the lake (Burgi *et al.*, 2014). For a system with conduit diameter of 4 m (dotted line) and bubble volume at the surface of the size 10 m^3, it can be seen from the figure that the bubble will be conduit-filling in the top 100 m. In fact, large bubbles within the conduit may exist as a spherical cap (Bouche *et al.*, 2010) whose radius is expected to be larger than the equivalent spherical radius. In this case, the depth at which large bubbles fill the conduit might extend to a deeper level. From the range of reported bubble volumes at the surface and the typical diameter for volcanic conduits, we expect that conduit-filling bubbles exist for at least the top few hundred metres below the surface. Given an estimated depth of Erta 'Ale lava lake within the range 32-43 m (Bouche *et al.*, 2010), it is expected that the conduit-filling bubbles originate within the conduit. Within this region, the magma convection will be disturbed by the rising bubbles and the exchange flow model is unlikely to persist (see experiments later in chapter). However, lava lakes do maintain their unfrozen state for many decades, and so heat is likely to be transferred through the upper part of the conduit by some other means. Although the concept that heat is supplied by bubble-related processes has been proposed by Bouche *et al.* (2010), no modelling or quantification has been carried out. In this study we explore the process of heat transfer by the liquid-gas separated flow whose gas bubbles are of comparable size to the volcanic conduit.

1.2.5 Experimental two-phase flow in a vertical conduit

Flow regimes

Gas and liquid flow within a long tube can undergo different flow patterns depending on the gas and liquid flux and also liquid viscosity. The liquid and gas bubbles are expected to undergo homogeneous flow if the liquid phase has a high viscosity which prevents bubbles from decoupling from the background motion, for example, with evolved silicic and highly viscous magma (Gonnermann & Manga, 2012). On the

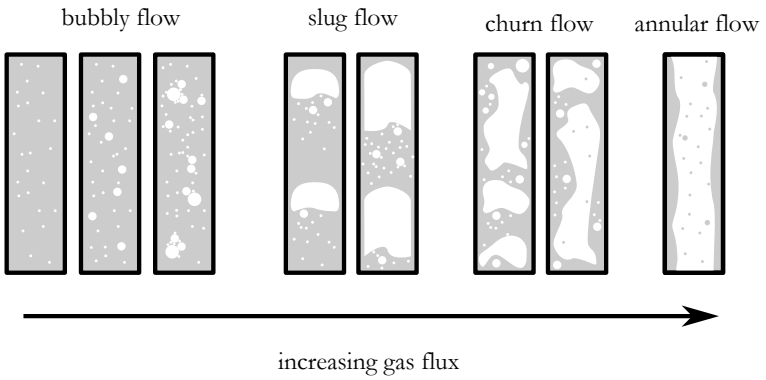

Fig. 1.7 Idealised vertical gas-liquid flow regime in vertical conduits (adapted from Pioli *et al.*, 2012). Liquid is shown in gray and gas bubbles are shown in white. For low gas flux, small gas bubbles may rise independently and bubbles have uniform size distribution. Increasing gas flux promotes bubble coalescence creating bubbles of different sizes. In slug flow, large bubbles become spherical-cap and fill up the conduit diameter. Increasing gas flux further, the large bubble becomes elongated and has the shape that resembles a Taylor bubble. Gas bubbles becomes unstable with further increase in gas flux which characterise churn flow regime. At annular flow conditions, the fluid may be dragged upwards by the gas motion.

contrary bubbles can separate from low-viscosity magma. In the laboratory, the flow patterns for water-air flows have been described as bubbly, slug, churn or annular depending on the gas flux through the system (Fernandes *et al.*, 1983; Harmathy, 1960; Nicklin, 1962; Taitel *et al.*, 1980).

Bubbly flows, formed at low gas flow rates, are characterised by small gas bubbles dispersed in the liquid and which rise independently of the magma. The rise speed of bubbles is found to increase with larger bubble diameter. With larger gas flux, bubble coalescence is promoted and larger gas bubbles are created. Conduit-filling bubbles – called Taylor bubbles (owing to pioneering experimental studies by Davies & Taylor, 1950) or gas slugs – characterise slug flows (Nicklin, 1962). These gas slugs are separated by regions of pure liquid in the conduit. The gap between two gas slugs reduces with increasing gas flux until the point where the flow becomes unstable and a churn flow develops. At the highest gas flux, the gas flows through the centre of the tube and has enough energy to drag the liquid film along the wall as the gas rises: this is known as core-annular flow. Figure 1.7 summarises the idealised flow regimes reported for experimental two-phase flow.

Small bubbles of various sizes (less than a few cm) rising through a conduit under the bubbly flow regime can rise to the surface and escape to the atmosphere. They are believed to account for the quiescent degassing observed at volcanos (Vergniolle &

Gaudemer, 2015). On the other hand, active degassing events, known as Strombolian eruptions, are usually described as a process in which bubbles which fill the conduit burst at the surface (Vergniolle & Brandeis, 1996; Vergniolle & Gaudemer, 2015). The flow within the conduit can be described as a slug flow regime which will be the main focus for this study.

Rise speed of gas slug

Bubbles whose radius is similar to that of the confining conduit are mostly referred to as Taylor bubbles. Bubbles with smaller size, but still of high Reynolds number, are mostly referred to as spherical caps. As a conduit-filling bubble rises, its front displaces liquid ahead of it and the liquid is forced to fall along conduit wall forming a liquid film between the gas bubble and the solid wall. The falling liquid film reaches the liquid pool at the bottom end of the bubble and forms a wake region behind the leading bubbles. The wake can be bubbly and turbulent if the liquid viscosity is sufficiently low, otherwise a laminar wake is expected, in which case, mixing is suppressed.

The rise speed of a single gas slug in a system with no background flow, u_o, can be written using the definition of Froude number, Fr, in the form

$$u_o = Fr\sqrt{g'd_c} = 0.35\sqrt{g'd_c}, \tag{1.41}$$

where $g' = g(\rho_l - \rho_g)/\rho_l$ is the reduced gravity and d_c is the conduit diameter. g' is defined as a function of the gas density, ρ_g, liquid density, ρ_l and gravitational acceleration, g. In most two-phase flow cases, $\rho_g \ll \rho_l$ and hence, $g \approx g'$.

The value for $Fr = 0.35$ has been determined both theoretically and experimentally (Nicklin, 1962) for air-water flows as well as other turbulent gas-liquid flows. With more viscous liquid, a more general model (Viana *et al.*, 2003) for the bubble rise speed based on experimental data has been proposed involving a complex function of Eötvös number (balance of gravity and surface tension), Eo, and Reynolds number based on the buoyancy forces, Re_B, which are defined as

$$Eo = \frac{\rho_l g d_c^2}{\sigma} \quad \text{and} \tag{1.42}$$

$$Re_B = \frac{\rho_l\sqrt{g d_c^3}}{\mu}, \tag{1.43}$$

where σ and μ are the surface tension and dynamic viscosity of the liquid, respectively.

In experimental slug flows created by constant gas and liquid fluxes, the background flow is no longer stationary but modified by the superficial gas and liquid speed. The ascent speed of a large bubble has been found to follow an empirical relationship (Nicklin, 1962)

$$u_b = 1.2\frac{(\dot{V}_g + \dot{V}_l)}{A} + u_o = 1.2\frac{(\dot{V}_g + \dot{V}_l)}{A} + 0.35\sqrt{g' d_c}, \tag{1.44}$$

where $\dot{V}_g, \dot{V}_l$ and A are the volumetric gas flow rate, liquid flow rate and the cross-sectional area of the conduit, respectively. The volume flux over conduit area, $\dot{V}/A$, is known as the superficial speed for each phase. This can be seen as the sum between the background velocity, $(\dot{V}_g + \dot{V}_l)/A$, and the rise speed of bubbles, (1.41). The pre-multiplying coefficient 1.2 is interpreted as the ratio of the maximum centreline to the cross-sectionally averaged vertical velocity and is applicable for turbulent flows (Nicklin, 1962) while a pre-multiplying coefficient of 2 is suggested for laminar flows.

In the geological context, it is difficult to investigate bubble motions within the conduit. Instead, the gas speed above the volcanic vent can directly be measured using visual or thermal photos or videos. More sophisticated devices including radar and sodar have been attempted. However, it has been shown experimentally that air can quickly entrain into the hot gas and this affects the observable vertical gas velocity. The measured gas velocity above the vent can, therefore, be significantly different from that within the conduit (Vergniolle & Gaudemer, 2015).

As a result, the speed of gas bubbles in the vent has mostly been estimated based on a number of assumptions. With the exchange flow model, it has mainly been assumed that the gas-magma flow is homogeneous and hence the gas speed is determined from the speed of magma. In contrast, separated flow is characterised by gas slugs rising with larger speed. The rise speed given by (1.44) has been found to describe slug flows successfully in many laboratory experiments and industrial applications (Morgado *et al.*, 2016; Nicklin, 1962; Taitel *et al.*, 1980). However, at volcanic vents, the gas fluxes are relatively small compared to the conduit size and hence, the superficial speed term, $\dot{V}/A$, becomes insignificant compared to the single slug rise speed term, u_o. The gas slugs are likely to rise as separated and individual bubbles whose speed is given by (1.41) provided that the flow is sufficiently turbulent. Using typical parameters for magmatic flows ($\sigma = 0.4$ N/m, $\rho_l = 2600$ kg/m^3, $\mu = 500$ Pa s and $1 < d_c < 10$ m), Seyfried & Freundt (2000) showed that flows within the conduit may either be inviscid, $Re_B > 300$, or transitional, $2 < Re_B < 300$ (James *et al.*, 2006) where Re_B

is Reynolds numbers based on the buoyancy forces of the liquid phase. For the latter regime, the magma viscosity cannot be completely ignored and the speed of the gas slugs is expected to be slightly lower than that suggested by equation (1.41).

In the second part of this thesis, we extended the use of the light attenuation technique to explore the liquid mixing in a vertical conduit under the influence of ascent bubbles. The system is analogous to liquid-gas separated flows which can be the case in many volcanic settings. The main purpose of this study is to develop an experimental technique that can quantify the rate at which the liquid mixes up the conduit under the influence of the gas flows. Together with our proposed mathematical models, the experimental results are then used to illustrate that our proposed mechanism can supply sufficient heat which allows lava lakes to persist over time.

1.2.6 Research outline

In order to explore the role of gas bubbles on the dynamics of such flows, **in chapter 4**, we present a new experiment to describe liquid-gas separated flow, analogous to the flow within a volcanic conduit feeding many lava lakes. In particular, we focus on the role of large bubbles on mixing the fluid in the conduit through the turbulent mixing in the wakes of successive bubbles. In turn we argue that this will disrupt the convective exchange flow but will also lead to heat transfer itself by a turbulent dispersion process. In order to demonstrate this turbulent dispersion, the light attenuation technique is applied to measure how dye tracer originally injected at the bottom of the conduit migrates along the conduit, even through there is no net flow of the liquid. With a constant supply of gas at the bottom, dye is gradually dispersed towards the top of the conduit. By analogy, we argue that in a volcanic conduit this dispersion will lead to heat transfer along the conduit. The dispersion coefficient is then determined as a function of gas flux and bubble speed. The results are then used to estimate the heat flux arriving at the top of a volcanic conduit as a result of slug flow. The model is compared to the heat loss at the surface of a lava lake situated on top of the conduit and shown to be consistent with field observations.

Chapter 2

Finite volume release axisymmetric gravity currents

2.1 Abstract

We present new experiments to measure the rate of entrainment of ambient fluid into a high Reynolds number, axisymmetric, turbulent gravity current. The current is produced by a rapid release of a finite volume of aqueous salt solution from a lock of length r_o into a diverging channel, $r > 0$, of angle 9.5°, filled with a finite depth, H, of fresh water. This resembles the evolution of gravity currents in the absence of a confined channel, such as turbidity currents when they exit a submarine canyon to an abyssal plain. Experiments using dye tracers show the dense fluid reaches the nose of the flow, rises up, mixes with the ambient and moves backwards relative to the nose forming a circulation in the head region. The evolving density and the volume of the flow are measured using a light attenuation technique. Due to mixing of the ambient fluid and the dense gravity current, it was found that the volume of the current increases as $V \sim 0.2 r_n^{7/4} r_o^{1/4} H$ while the maximum depth of the head decreases as $h_n \sim 0.5 H (r_o/r_n)^{1/4}$, where r_n is the location of the front of the current. Combining these results, it can then be estimated that the recirculating current fluid mixes with a fraction $\varepsilon = 0.33 \pm 0.09$ of the ambient fluid that is directly ahead of the current and displaced upwards by it. Some of the mixed fluid supplies the tail of the flow, while the remainder recirculates into the head, which becomes progressively more dilute. In accord with Huppert and Simpson (1980), the experiments show that the position of the front increases with time as $r_n \approx (1.28 \pm 0.05) B^{1/4} t^{1/2}$, where B is the total buoyancy of the flow. The maximum value of the vertical integral of the buoyancy

$(\overline{g'h})_n$ is determined and is found to decrease with position of the nose according to the relation $(\overline{g'h})_n \approx (0.89 \pm 0.12) Br_n^{-2}$, consistent with a Froude number 0.86 ± 0.07. The measurements are then compared with a new idealised self-similar solution of the depth averaged equations which accounts for the mixing at the nose, the vertical shear in the velocity and the lateral stratification of the buoyancy within the current.

2.2 Introduction

Turbulent gravity currents are produced when a finite volume of dense fluid is rapidly released from a source above a horizontal boundary into an environment of lower density. The dense fluid spreads horizontally under gravity along the lower boundary of the flow domain, displacing the original fluid in place. Gravity currents have been studied in considerable detail, using a combination of laboratory experiments and mathematical models owing to their importance in frontal dynamics, volcanic eruptions, turbidity currents, and many environmental flows (Kneller & Buckee, 2000; Prandtl, 1952; Simpson, 1999; Sparks *et al.*, 1997). Many papers have examined two dimensional gravity currents in a confined parallel sided channel, exploring the ratio of the propagation speed of the front, $\mathrm{d}r_n/\mathrm{d}t$, with the product of the buoyancy and depth, $g'h$, as expressed by the Froude number, Fr, $\mathrm{d}r_n/\mathrm{d}t = Fr(g'h)^{1/2}$. Various solutions of shallow water equations have been presented to describe these flows, often assuming that there is no mixing with the ambient fluid (cf. Benjamin 1968; Bonnecaze *et al.* 1995; Chen 1980; Slim & Huppert 2004).

Huppert & Simpson (1980) carried out experiments to examine the motion of axisymmetric gravity currents produced by a discrete release of fluid of total buoyancy B, and established that provided the Reynolds number is sufficiently high, the front of the current advances as $r_n = 1.3B^{1/4}t^{1/2}$. Hallworth *et al.* (1996, 1993) and Hacker *et al.* (1996) measured the entrainment of ambient fluid into gravity currents, and established that the head becomes progressively more dilute with distance. Hallworth *et al.* (1996) used an acid-alkali system with which the mixing in the head could be measured by assuming the head is well mixed and recording the position of the head at which a pH indicator in the head changed colour. Using this approach, they reported a gradual decrease in the volume of the head with distance. Patterson *et al.* (2006) carried out some PIV experiments to explore the velocity structure of the current and this demonstrated that the front of an axisymmetric gravity current involves a vortical flow which facilitates the mixing between the current fluid recirculating over the

top of the nose and the ambient fluid displaced by the nose. Cantero *et al.* (2007*a*,*b*) presented a series of direct numerical simulations of axisymmetric gravity currents, illustrating the importance of the vortex rings and cleft and lobe instabilities at the front of the flow in driving mixing. Adduce *et al.* (2012) and Johnson & Hogg (2013) modelled the mixing into two dimensional gravity currents using a parameterised entrainment law all along the upper surface of the flow, while Özgökmen *et al.* (2009) have presented numerical simulations of the mixing.

Although these have been very valuable contributions, there is more to be learnt about the process of mixing and entrainment into axisymmetric gravity currents through detailed measurement of the buoyancy as a function of position in the current and time after the lock release. This is the primary purpose of the present chapter. We use a light attenuation technique to measure the evolving salinity of the fluid in aqueous saline gravity currents (cf. Hacker *et al.*, 1996). For the low salt concentrations used in our experiments, the salinity is directly proportional to the buoyancy (Turner, 1979) and the Boussinesq approximation applies. We also follow pulses of dye in the current and the ambient fluid to establish how the mixing occurs. Using our new experimental data, we find that a fraction $\varepsilon \sim 0.33 \pm 0.09$ of the fluid ahead of the current, which is displaced by the current, mixes with the recirculating current fluid. This mixed fluid is distributed between the wake and head of the flow, producing a vertically and radially stratified flow. We establish scalings for the speed, height, vertically averaged buoyancy and Froude number of the head, based on our experimental data. We then compare the experimental depth and buoyancy profiles in the flow with an idealised self-similar solution derived from the depth averaged equations of motion, in which we account for the mixing at the head and the vertical shear and stratification in the flow.

2.3 Experimental Method

A series of turbulent laboratory gravity currents were generated through the release of a finite volume of aqueous salt solution into a 3m long perspex tank with free surface at the top. The width of the tank increases from 0 to 50cm along the length of the tank, until reaching the end wall. The two long side walls subtend an angle of approximately $\sim 9.5^\circ$ (figure 2.1). The details of the parameters for each experiment are shown in Table 2.1, including the depth of the fluid, H, the radius of the lock gate, r_o, and the aspect ratio of the source, H/r_o, as well as the initial buoyancy associated

Exp.	r_o (cm)	H (cm)	g'_o (cm/s^2)	Aspect ratio H/r_o	Detail of dye injection	t_o	$\mathcal{R}$	Fr	Re $\times 10^3$	
A	36	18	33.35	0.5	a	-2.35	1.24	0.86	20–2	●
B	36	18	47.68	0.5	a	-2.28	1.25	0.80	20–2	●
C	36	18	54.84	0.5	a	-1.72	1.23	0.79	20–2	●
D	36	18	33.35	0.5	a	-2.45	1.24	0.84	20–0.6	●
E	36	18	26.29	0.5	a	-2.50	1.24	0.84	20–0.6	●
F	36	36	26.29	1.0	a	-3.30	1.33	0.85	50–5	●
G	36	36	40.52	1.0	a	-3.30	1.34	0.94	50–5	●
H	36	36	40.52	1.0	a	-3.30	1.37	0.90	50–5	●
I	36	36	40.52	1.0	a	-2.30	1.31	0.89	50–5	●
J	36	26	40.52	0.7	a	-2.00	1.26	0.84	40–3	●
K	36	15	40.52	0.4	a	-2.25	1.25	0.76	10–0.5	●
L	36	30	40.52	0.8	a	-2.10	1.26	0.84	50–5	●
M	36	36	40.52	1.0	b	-2.5	1.26			
N	36	36	40.52	1.0	c	-3.0	1.27			

Table 2.1 Table of experiments illustrating the range of aspect ratio and dimensions of the lock. a. light attenuation experiment; b. dye injected into head of the flow; c. dye injected into the ambient fluid. Column of colours indicates colours of data shown in subsequent graphs. The quantities t_o, $\mathcal{R}$ and Fr are properties of the current which are defined in section 3.3. In the table, for each experiment, we list the asymptotic values of $\mathcal{R}$ and Fr for $r_n > 3r_o$ (figure 2.5a,b)

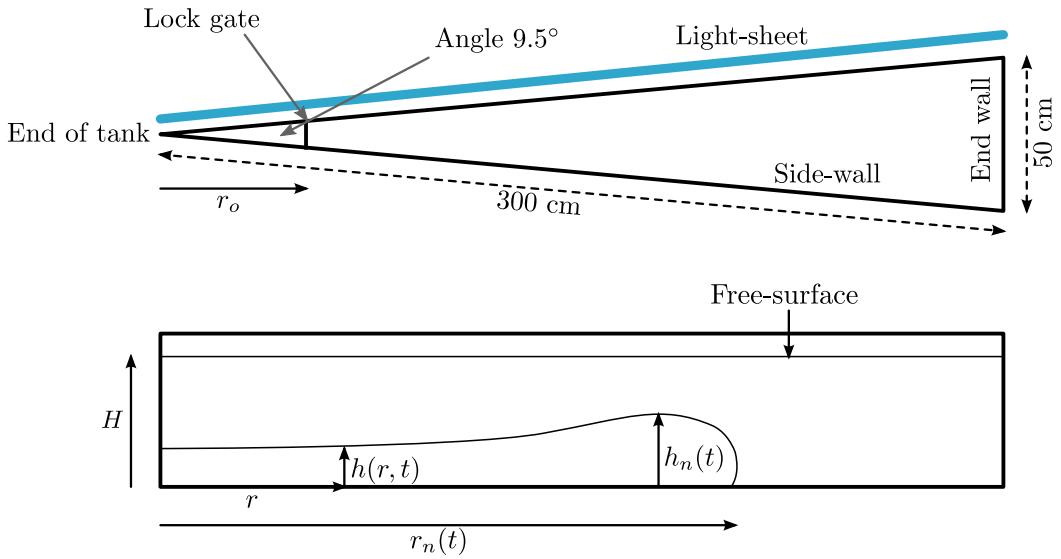

Fig. 2.1 Schematic diagram of the experimental tank, showing a top view and a side view of the tank. Figure also illustrates the depth h of the current at radius r, the maximum depth h_n, the position of the nose of the current r_n, and the radius of the lock gate, r_o.

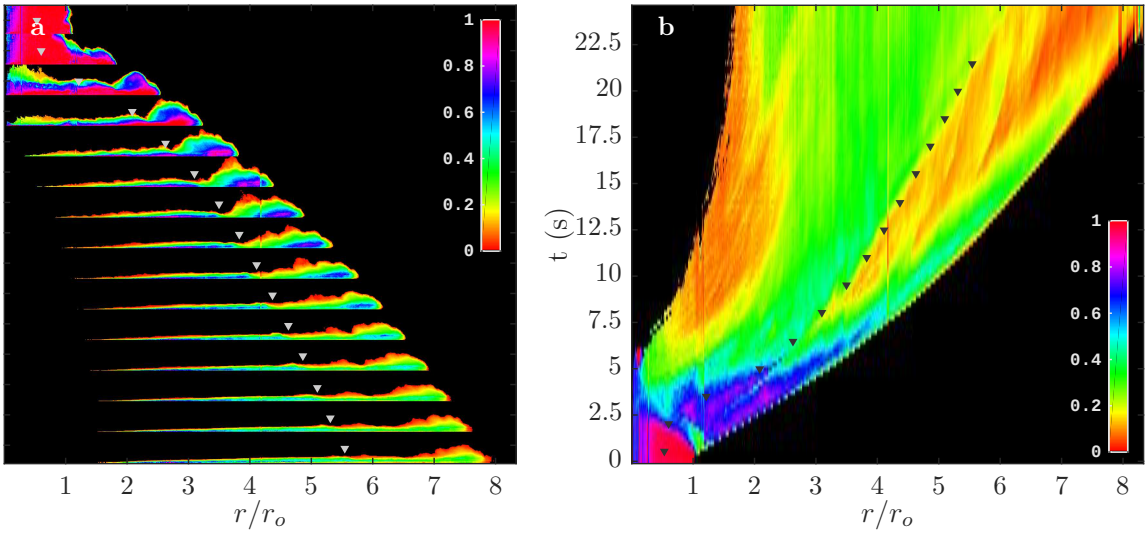

Fig. 2.2 (a) Photographs of a saline gravity current illustrating the evolution of the buoyancy, shown by false-colour contours, as the current from experiment H (Table 2.1) advances along the flume. Images are taken at equal time intervals of 1.5s. The x-axis shows the position in the current as a function of the number of lock lengths. The colour scale represents the value g'/g'_o which is the local buoyancy, g', measured as a fraction of the original buoyancy, g'_o. (b) Evolution of the depth averaged buoyancy of the flow as a function of position and time. The horizontal axis represents horizontal position, r/r_o, and the vertical axis is time. The colours represent the depth averaged buoyancy of the gravity current, with the legend illustrating the fraction of original buoyancy of the fluid which was released from behind the lock gate. The triangles in the figure denote the horizontal position at which the volume of the current in the region between the back of the lock and the triangle equals 25% of the total volume of the current (see figure 2.6b).

with the salinity, $g'_o = g(\rho_s - \rho_w)/\rho_w$ where g is the acceleration due to gravity, ρ_s is the density of the saline water behind the lock gate and ρ_w is the density of the fresh water (ambient fluid). The volume and buoyancy in our experiments overlap those used in many of the previous experimental studies of axisymmetric gravity currents (Hallworth *et al.*, 1996; Huppert & Simpson, 1980; Patterson *et al.*, 2006) as well as the numerical study of Cantero *et al.* (2007*a*). In many of the experiments, the aqueous solution was initially dyed with a known mass of red TRS food dye, and the tank was back-lit using a matrix LED light panel (W&Co Displays and Signs). In order to measure the dilution of the current associated with the mixing, solutions with different concentration of dye were placed in the experimental tank, in sequence, and the red-green-blue (RGB) light intensity was recorded for each such solution at each point on one of the vertical walls of the tank using a Nikon D90 RGB DSLR camera.

The images were analysed using a MATLAB script to generate calibration curves relating light intensity to the salinity, s, and hence buoyancy, $g' = g\mathcal{S}s$, where $\mathcal{S}$ is the solutal expansion coefficient, following an approach analogous to Hacker *et al.* (1996), Fragoso *et al.* (2013) and van Sommeren *et al.* (2012). Since the width of the channel varies with radius, we used different local calibration curves, dividing the tank wall into individual regions each spanning 1cm by 1cm. The experimental images can then be analysed to determine the distribution of buoyancy within the tank, accounting for the effects of the varying width of the tank on the light attenuation by using the local calibration curves. The buoyancy data we obtain is a span-wise average. However, owing to the small angle subtended by the two side walls of the tank, the variation in the radius across a span, as measured from the rear of the lock gate, is less than 0.5% of the radius. We therefore interpret our data as providing an approximation for the radial distribution of buoyancy. The camera was set to take either 2 or 4 frames per second with shutter speed 1/100, aperture F4.8 and ISO 640. The precise timing of the images was checked carefully in a control experiment. The camera recorded 10 pixels per cm in the vertical and horizontal directions throughout the flow domain. Most of the currents attained high Reynolds number, $Re = \frac{h_n}{\nu}\frac{dr_n}{dt} > 5000$ where ν, h_n and r_n are the kinematic viscosity, maximum depth of the current and position of the nose respectively. We estimate that the image calibration method used to convert light intensity to buoyancy has an error less than 8% (appendix A) for all experiments and this is reflected in the error bars presented in our analysis.

2.4 Experimental Observations

Figure 2.2a illustrates the time evolution of the gravity current for experiment H (Table 2.1). The sequence of false colour images correspond to the buoyancy of the fluid in the tank at intervals of 1.5s after release of the lock gate. Immediately after lock release, while the position of the nose, r_n, is close to the source, $r_n < 2.5r_o$, the current adjusts to a head-tail structure. Subsequently, as the front advances through the region $2.5r_o < r_n < 8r_o$, the current becomes progressively less dense and stratified in both the vertical and horizontal direction. The maximum density arises in the lower part of the head of the flow. With time, the head region develops a strong vortical structure, with the dense fluid lower in the head reaching the front of the head, and rising up over the head. Here it mixes with ambient fluid as it recirculates backwards relative to the head. In figure 2.2b, we illustrate the evolution of the vertically averaged buoyancy of the current as a function of radius. In the figure, a series of triangles are shown, such that the volume of the current between the back of the lock and the triangle is a fraction 0.25 of the total volume of the current. The image illustrates that the vertically averaged buoyancy of the current in the region ahead of the triangles progressively decreases with time and increases in the radial direction, with the vertically averaged buoyancy being largest just behind the leading front of the current. In panel a, it can be seen that in the region upstream of the triangles, the current is very thin and in this region the flow appears to become controlled by bottom friction. The fluid which lags behind in this bottom layer appears to be relatively dense fluid from the base of the flow as may seen in panel b, where the vertically averaged buoyancy increases upstream of the triangles.

2.4.1 Mechanism of Mixing

In order to build up understanding of how the mixing occurs, we have carried out a series of experiments in which we inject and then track a small volume of dye in both (i) the current and (ii) the ambient fluid. Figure 2.3a illustrates the advance of a yellow gravity current advancing into a clear ambient fluid (experiment M, Table 2.1). In this experiment, a pulse of red dye was injected at $r = 3r_o$ into the current, when the nose of the current reached the position $r_n = 3.5r_o$. The dye pulse is observed to migrate forwards relative to the front of the current and on reaching the front of the current, the dyed fluid rises to the top of the current and recirculates backwards relative to the front. Here it seems to mix with some of the ambient fluid originally ahead of

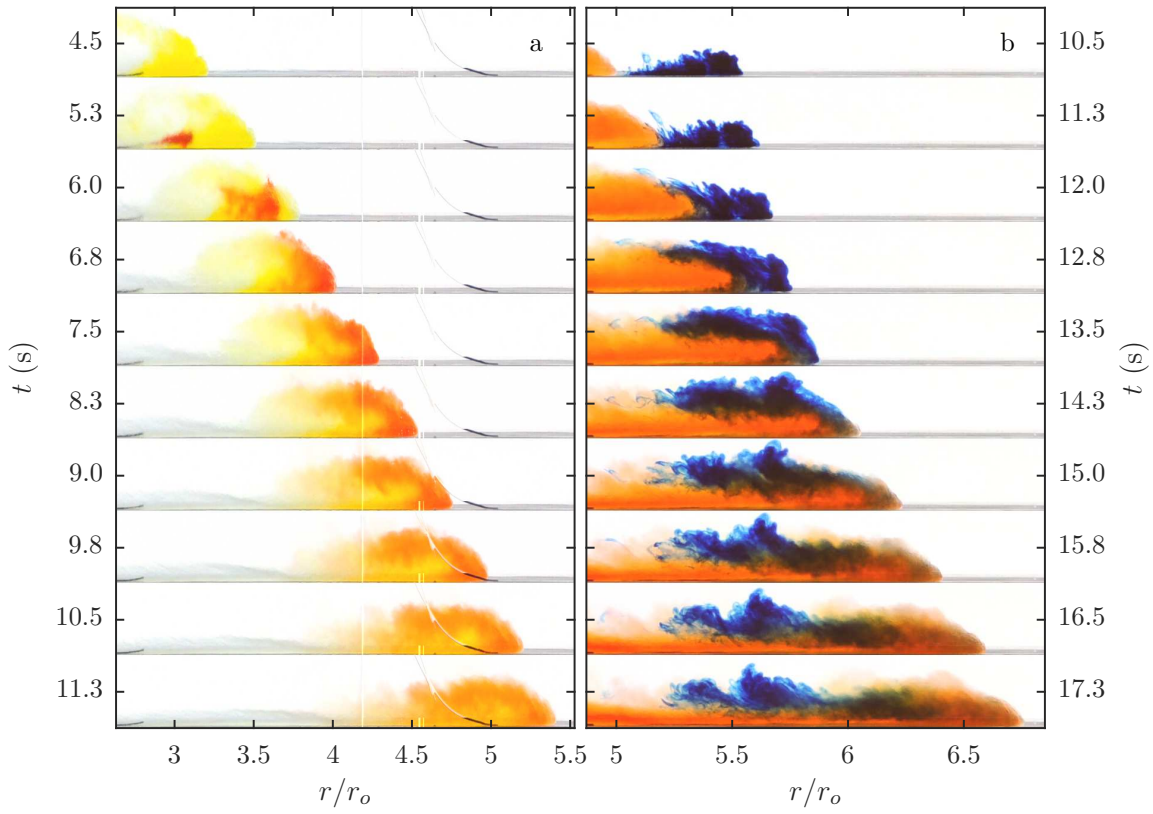

Fig. 2.3 Series of images of the current at successive times. (a) Transport of a pulse of red dye injected just behind the front of the flow in the head (Exp. M). This shows how the dyed fluid in the current advances to the front of the flow, and then recirculates over the top of the current. Here it mixes with the ambient fluid which is displaced up over the advancing head of the flow. (b) Transport of dyed blue ambient fluid injected just ahead of the front of the red current (Exp. N). Some of the ambient fluid displaced by the current remains above the current after the head has passed by, and hence does not mix with the current, while the remainder mixes into the current, recirculating in the flow.

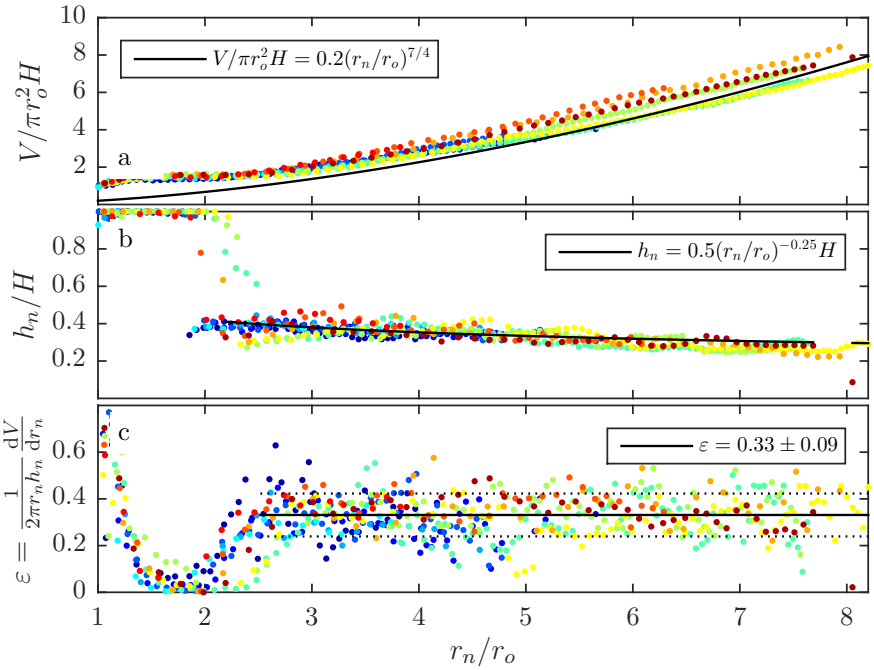

Fig. 2.4 Variation as a function of r_n/r_o of (a) the volume of the current; (b) the height of the head of the current in the region $r_o < r_n < 8r_o$ and (c) the entrainment coefficient ε defined by (2.3) and estimated from the experimental data shown in panels a and b. Colours represent results from different experiments as coded in table 2.1.

the current which is displaced up and over the current. Similar mixing behaviour was observed in numerous other experiments in which dye was injected behind the front of the current but with the front of the current located at different radial distances from the lock.

We also added dye to the ambient fluid to provide a complementary perspective on the mixing in the head region of the flow. As seen in figure 2.3b, the red gravity current in experiment N (Table 2.1) displaced a region $5.2r_o < r < 5.5r_o$ in which the ambient fluid originally ahead of the current was dyed blue. The images show that the dyed blue ambient fluid rises over the current and there is some mixing with the recirculating current fluid. The mixed fluid migrates backwards relative to the advancing head and becomes partitioned into the head and tail of the current. Meanwhile, the remainder of the displaced ambient fluid (blue) rises up over the head, and comes to rest once the head has passed by.

2.4.2 Entrainment coefficient

Using the light attenuation technique, we have measured the instantaneous volume of the whole current and the maximum depth of the head as a function of the radius of the front of the current by determining those pixels for which the concentration of dye is in excess of the original value (figures 2.4a,b). Once we have measured the volume, V_e, in our experimental sector model, of angle ϕ, we convert this to an equivalent volume V of a fully axisymmetric current, $V = (2\pi/\phi)V_e$. We also define the total buoyancy B as that of the equivalent fully axisymmetric current, $B = (2\pi/\phi)B_e$ where $B_e = g'_o V_e$ is the actual total buoyancy of the fluid behind the lock gate. In the figure, the volume, $V(t)$, and maximum depth, $h_n(t)$, are presented in dimensionless form, $V/(\pi r_o^2 H)$ and h_n/H. Although there is some fluctuation in the volume and depth measurement associated with the time-dependent billow structures on the upper surface of the flow (figure 2.2), to reasonable approximation, for $r_n > 2.5r_o$, the data follow the approximate relations

$$V = (0.2 \pm 0.02)\pi r_n^{7/4} r_o^{1/4} H, \tag{2.1}$$

$$h_n = (0.5 \pm 0.02)H(r_o/r_n)^{1/4}. \tag{2.2}$$

If we assume that the fluid entrained into the current originates from the fluid displaced by the head of the flow, as indicated by the dye studies, and we define ε to be the fraction of this fluid which is entrained into the flow, we can write

$$\frac{\mathrm{d}V}{\mathrm{d}t} = 2\pi\varepsilon r_n h_n \frac{\mathrm{d}r_n}{\mathrm{d}t}. \tag{2.3}$$

Noting $\mathrm{d}V/\mathrm{d}t = (\mathrm{d}V/\mathrm{d}r_n)\,(\mathrm{d}r_n/\mathrm{d}t)$, and using the data shown in figure 2.4(a,b), we find that for $2.5r_o < r_n < 7r_o$, the entrainment coefficient $\varepsilon = 0.33 \pm 0.09$ (figure 2.4c). The approximate scaling laws (2.1) and (2.2), which combined with equation (2.3), suggest $\varepsilon = 0.35 \pm 0.04$ are consistent with this direct measurement from the data. We note that in the region $r_o < r_n < 1.4r_o$, the entrainment coefficient decreases rapidly from about 0.7 to 0.05. This is associated with the mixing across the near vertical interface produced from the removal of the lock gate. The mixing then remains small as the flow slumps from the lock and the head becomes established. Then, as the head

moves through the region $2r_o < r_n < 2.5r_o$, ε increases to the value $\varepsilon = 0.33 \pm 0.09$ which applies for $r_n > 2.5r_o$.

2.4.3 Scaling Laws for the Head

We also measured the position of the nose, $r_n(t)$, and the maximum value of the vertical integral of the buoyancy as a function of time. In figure 2.5a, we illustrate the variation of the ratio

$$\mathcal{R} = \frac{r_n(t)}{B^{1/4}(t + t_o)^{1/2}} \tag{2.4}$$

with r_n/r_o, and find that after an initial transient, $\mathcal{R} \rightarrow 1.28 \pm 0.05$ consistent with the value 1.3 reported by Huppert & Simpson (1980). In calculating $\mathcal{R}$, for each experiment, we have estimated a value of the virtual origin in time, t_o, by plotting r_n^2 as a function of time, t, and finding the time $-t_o$ at which the best fit straight line through the data intersects the time axis. This corresponds to the difference between the initial adjustment phase after removing the lock gate, when $r_n < 2.5r_o$, and the idealised release of a point source of buoyancy of zero volume. We find that t_o decreases in magnitude from -3.5s to -1.5s, as the aspect ratio of the source, H/r_o, decreases from 1.0 to 0.4. These values are considerably shorter than the 25-30s typically required for the current to travel to a distance $r_n \approx 7 - 8r_o$.

Earlier studies have proposed that the Froude number at the head of the current is a constant. Using our light attenuation data, we have measured the maximum value of the vertical integral of buoyancy in the current. This maximum occurs near the front of the current (figure 2.6b), and combining this with the speed of the nose we can calculate the Froude number, Fr, as given by

$$\frac{\mathrm{d}r_n}{\mathrm{d}t} = Fr\sqrt{(\overline{g}'h)_n} \quad \text{where} \quad (\overline{g}'h)_n = \max\left(\overline{g}'h = \int_0^{h(r)} g'dy\right). \tag{2.5}$$

Here $g'(r, y, t)$ is the buoyancy in the current and equation (2.5)b defines the vertically averaged buoyancy, $\overline{g}'$. The variation of Fr as a function of the dimensionless time for our experimental currents A-L (Table 1) is shown in figure 2.5b. It is seen that for $r_n > 2.5r_o$, $Fr \rightarrow 0.86 \pm 0.07$, once the current has passed through an initial adjustment region. Combining equation (2.4) and (2.5), we find $(\overline{g}'h)_n \approx (0.89 \pm 0.12)B/r_n^2$.

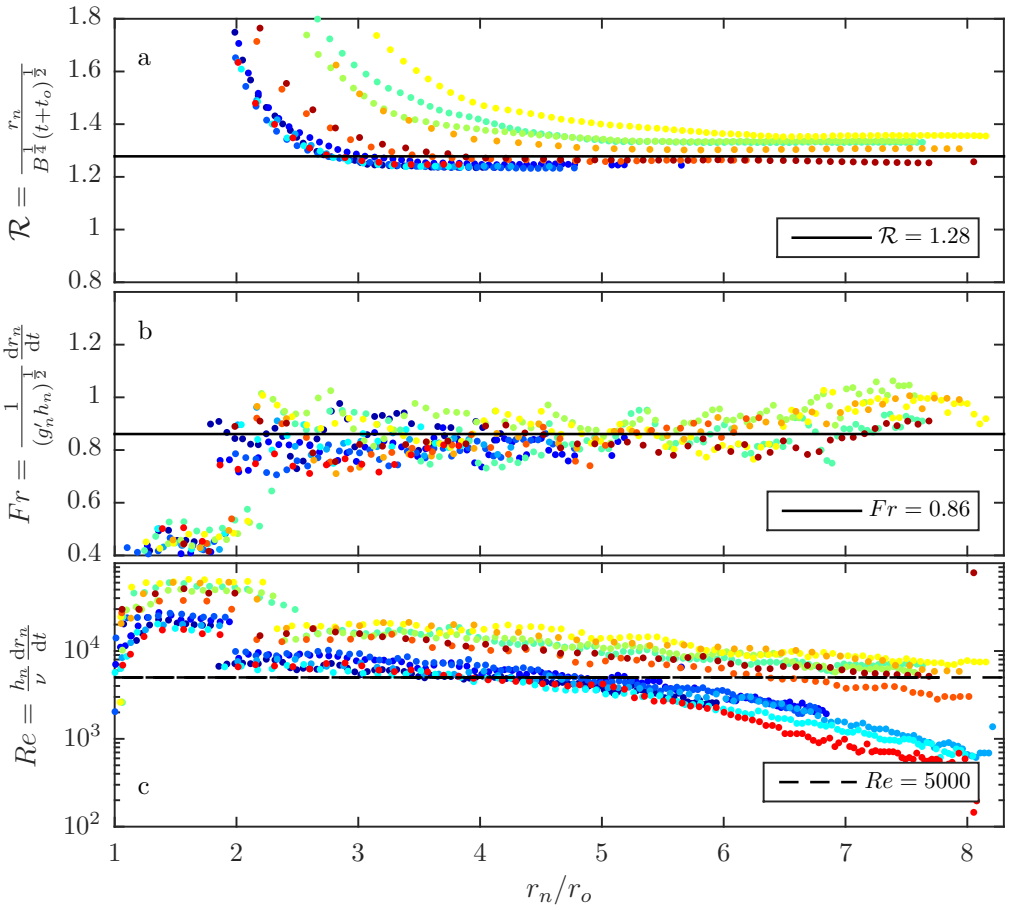

Fig. 2.5 Data from experiments A-L (Table 2.1) illustrating (a) the variation with time of $\mathcal{R} = r_n(t)/B^{1/4}(t+t_o)^{1/2}$, where r_n is the position of the nose of the current as a function of time; (b) the variation with time of the Froude number, $Fr = \left(\frac{\mathrm{d}r}{\mathrm{d}t}\right)_n (\overline{g'_n} h_n)^{-\frac{1}{2}}$, where $(\overline{g'}h)_n$ is the maximum value of the vertical integral of buoyancy as a function of the position in the current; (c) the variation of the Reynolds number in the head with time. The data that fall below $Re = 5000$ appear to be influenced by friction, and are not shown in panels a-b. Colours represent results from different experiments as coded in table 2.1.

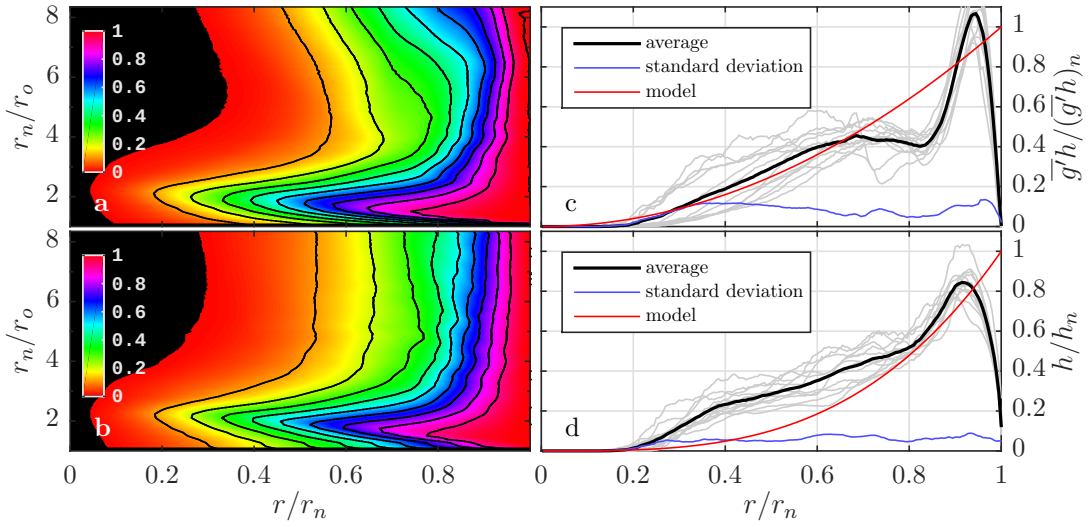

Fig. 2.6 Variation with position r/r_n of (a) the buoyancy in the current between the source and radius r as a fraction of the total buoyancy, $\int_0^r r\overline{g'}hdr/\int_0^{r_n} r\overline{g'}hdr$ (Exp. H), (b) the volume of the current in the region between the source and the position r as a fraction of the total volume, $\int_0^r rhdr/\int_0^{r_n} rhdr$ (Exp. H), (c) profiles of the dimensionless vertical integral of buoyancy (eqn 5a) and (d) profiles of the dimensionless depth (eqn 5b). (a,b) The black contour lines denote the horizontal location where the fraction of (a) the total buoyancy or (b) the total volume exceeds the value 0.1, 0.2, ..., 1.0. (c,d) Gray profiles denote the time-average for each of the experiments A-L. The ensemble averages, standard deviations from these ensemble averages and the prediction of the simplified similarity solution (eqn 12) are shown in black, blue and red profiles, respectively.

For each of the experiments shown in figure 2.5(a-c), the Reynolds number at the head of the flow, remained in excess of 5000 (figure 2.5c). In other experiments, for which the initial volume of fluid was smaller, we found that once the Reynolds number at the head falls below a value of about 5000, the value of $\mathcal{R}$ (2.4) gradually decreased with distance along the tank. We focus on flows with higher Reynolds number, although given the size of our experimental system, this limits the study to currents for which $r_n < 8r_o$. Over this range our experimental data appear to follow the scaling laws as proposed in equations (2.1)-(2.4) but it would be of interest to carry out experiments in a larger facility with much larger currents.

2.4.4 Structure of the current

In the contour plot, figure 2.6 (a), we show how the buoyancy in the current between the source and radius r, as a fraction of the total buoyancy, $\int_0^r rg'hdr/\int_0^{r_n} rg'hdr$, varies with the position in the current, r/r_n (horizontal axis), and also with time, as

represented by the position of the nose, r_n/r_o (vertical axis). Similarly, in panel (b) we show how the fractional volume of the current in the region between the source and the position r, $\int_0^r rhdr/\int_0^{r_n} rhdr$, varies with position r/r_n and time, as represented by r_n/r_o. The black contour lines denote the position in the current, r/r_n, at which the fraction of the total buoyancy (a) or of the total volume (b) exceeds the values 0.1, 0.2, ..., 1.0 respectively, as a function of time, as represented by r_n/r_o. Figure 2.6(a,b) were calculated for experiment H, but are typical of all experiments A-L (table 3.1).

Profiles of the dimensionless vertical integral of the buoyancy and of the dimensionless depth, as given by

$$\overline{g'}h(r,t)/(\overline{g'}h)_n(t) \quad \text{and} \quad h(r,t)/h_n(t) \tag{2.6}$$

have been averaged over the time during which $2.5 < r_n/r_o < 7$, for each of the experiments A-L. The time-average profiles are shown as light grey lines in figures 2.6(b,d). The ensemble average of these profiles are shown as the solid black line, and the standard deviation associated with the difference between the individual profiles and this ensemble average is indicated by the blue line.

The strong vortical motion in the leading part of the current can be seen to have an important influence on the profiles; there is in fact a local minimum in the depth integrated buoyancy in the region $0.7 < r/r_n < 0.9$.

Figure 2.6b shows that for $r > 2.5r_n$, the contours of constant fractional volume have an approximately constant position in the current as the current advances and grows (figure 2.4a). However, figure 2.6a shows that there is some variation with time of the position within the current at which different fractions of the total buoyancy of the current occur. In particular, as the current advances forward, a progressively larger fraction of the buoyancy appears to be left in the wake of the flow. The line of triangles in figure 2.2, located at $r \approx 0.7r_n$, seem to delineate a transition from a deeper active part of the flow, $r \geq 0.7r_n$ to a shallow wake, $r < 0.7r_n$. Figures 2.6(a,b) also illustrate that while $2.5 < r_n/r_o < 7$, this active leading part of the current, $0.7r_n < r < r_n$, accounts for about 75% of the current volume and in excess of 75% of the buoyancy of the current. Owing to the slow loss of buoyancy from the front of the current into the wake (figure 2.6a), the current is not strictly self-similar. However, given the scalings in the head of the current (figures 2.4, 2.5), and given that the contours of fractional volume of the current are approximately independent of time for $2.5 < r_n/r_o < 7$ (figure 2.6b), it is of interest to compare the data with

some new self-similar solutions of the depth-averaged equations which account for the entrainment in the head (2.3).

2.5 A depth averaged model

By applying the Boussinesq approximation and considering the entrainment occurs at the head of the inviscid flow, the local equations for the mass, momentum and buoyancy conservations are in the form

$$\nabla \cdot \mathbf{u} = 0, \tag{2.7a}$$

$$\rho \frac{\partial \mathbf{u}}{\partial t} + \rho \mathbf{u} \cdot \nabla \mathbf{u} = -\nabla p + \rho \mathbf{g}, \tag{2.7b}$$

$$\frac{\partial g'}{\partial t} + \mathbf{u} \cdot \nabla g' = 0, \tag{2.7c}$$

where the velocity of the fluid in the axisymmetric case is given by $\mathbf{u} = u\hat{\mathbf{r}} + w\hat{\mathbf{z}}$. The equation for conservation of mass of the current (2.7a) in the axisymmetric case is

$$\frac{1}{r}\frac{\partial ru}{\partial r} + \frac{\partial w}{\partial z} = 0. \tag{2.8}$$

Using Leibniz's rule, the no-penetration condition $w(0) = 0$ and knowing that the motion of the top surface of the current is given by

$$\frac{\partial h}{\partial t} + u(h)\frac{\partial h}{\partial r} = w(h), \tag{2.9}$$

the continuity equation, (2.8), can be integrated across the depth of the flow, h, to obtain

$$\frac{\partial h}{\partial t} + \frac{1}{r}\frac{\partial}{\partial r} r \int_0^h u \mathrm{d}z = 0. \tag{2.10}$$

We then consider the r-momentum equation in the conservation form (2.7b). Combining this with (2.8), the r-momentum equation becomes

$$\frac{\partial u}{\partial t} + \frac{1}{r}\frac{\partial ru^2}{\partial r} + \frac{\partial uw}{\partial z} = -\frac{1}{\rho}\frac{\partial p}{\partial r}. \tag{2.11}$$

The pressure gradient term can be taken to be hydrostatic as the current is considered to be long and thin, we then write

$$p(z,r,t) = p_o(r,t) + \int_z^H \rho_o g \mathrm{d}z' + \int_z^h \rho_o g' \mathrm{d}z' \tag{2.12}$$

where $p_o(r,t)$ is the ambient pressure along a horizontal surface of height H where $H > h$, ρ_o is the ambient density and $g' = g(\rho - \rho_o)/\rho_o$ is the buoyancy. We can then integrate the r-momentum equation across the depth of the flow, h.

$$\int_0^h \left[\frac{\partial u}{\partial t} + \frac{1}{r}\frac{\partial r u^2}{\partial r}\right] \mathrm{d}z + u(h)w(h) = -\int_0^h \frac{1}{\rho}\frac{\partial p}{\partial r}\mathrm{d}z \tag{2.13}$$

Using Leibniz's rule on the LHS and substituting (2.12) into the RHS of the (2.13) with the aid of Boussinesq approximation implying $\rho_o/\rho \approx 1$ everywhere except in the buoyancy term, this leads to

$$\begin{aligned} \frac{\partial}{\partial t}\int_0^h u \mathrm{d}z + \frac{1}{r}\frac{\partial}{\partial r}\int_0^h r u^2 \mathrm{d}z - u(h)\left(\frac{\partial h}{\partial t} + u(h)\frac{\partial h}{\partial r} - w(h)\right) \\ = -\int_0^h \frac{\partial}{\partial r}\left[\int_z^h g' \mathrm{d}z'\right]\mathrm{d}z - \frac{h}{\rho}\frac{\partial p_o}{\partial r} \end{aligned} \tag{2.14}$$

The term in the bracket on the LHS is zero as suggested by (2.9). This leads to the final form for the momentum equation as

$$\frac{\partial}{\partial t}\int_0^h u \mathrm{d}z + \frac{1}{r}\frac{\partial}{\partial r}\int_0^h r u^2 \mathrm{d}z = -\frac{\partial}{\partial r}\int_0^h \int_z^h g' \mathrm{d}z' \mathrm{d}z - \frac{h}{\rho}\frac{\partial p_o}{\partial r} \tag{2.15}$$

Lastly, we can integrate the buoyancy conservation equation across the depth of the flow and combine this with the continuity equation (2.8) and the boundary condition (2.9). This results in

$$\frac{\partial}{\partial t}\int_0^h g' \mathrm{d}z + \frac{\partial}{\partial r}\int_0^h u g' \mathrm{d}z = 0. \tag{2.16}$$

Based on the equations (2.10), (2.15) and (2.16), we may write the conservation of mass, momentum and buoyancy equations in terms of shape factor α, β and γ and the vertically averaged radial velocity, $\overline{u}$ as follows (cf. Bonnecaze *et al.* 1995; Chen

1980)

$$\frac{\partial h}{\partial t} + \frac{1}{r}\frac{\partial (r h \bar{u})}{\partial r} = 0, \tag{2.17a}$$

$$\frac{\partial (h\bar{u})}{\partial t} + \frac{1}{r}\frac{\partial \left(\beta r h \bar{u}^2\right)}{\partial r} = -\frac{\partial \left(\gamma h^2 \overline{g'}\right)}{\partial r} - \frac{h}{\rho}\frac{\partial p_o}{\partial r}, \tag{2.17b}$$

$$\frac{\partial (h\overline{g'})}{\partial t} + \frac{\partial (\alpha h \overline{g'} \bar{u})}{\partial r} = 0 \tag{2.17c}$$

where ρ is a representative density, p_o the pressure, and the depth averaged properties are defined as

$$h\bar{u} = \int_0^h u \mathrm{d}z \ ; \tag{2.18a}$$

$$\beta h \bar{u}^2 = \int_0^h u^2 \mathrm{d}z \ ; \tag{2.18b}$$

$$h\overline{g'} = \int_0^h g' \mathrm{d}z \ ; \tag{2.18c}$$

$$\alpha h \overline{g'} \bar{u} = \int_0^h u g' \mathrm{d}z \ \text{ and} \tag{2.18d}$$

$$\gamma h^2 \overline{g'}(r,t) = \int_0^h \int_z^h g'(r,z,t) \mathrm{d}z' \mathrm{d}z. \tag{2.18e}$$

In contrast to earlier models (Bonnecaze *et al.*, 1995; Chen, 1980), we have included the coefficients α, β and γ (2.18) which arise from the vertical gradient of the horizontal velocity and the buoyancy in the flow, as illustrated in figures 2.2 and 2.3 (cf. Kneller & Buckee 2000). α and β represent the advection speed of the reduced gravity and momentum relative to that of the vertically averaged flow. In principle these coefficients may vary along the direction of flow, for example in the nose region.

As a result of the entrainment (2.3), we can integrate (2.17) to show that the vertically averaged mean fluid speed at the front, $\bar{u}(r_n)$ is given by

$$\bar{u}(r_n) = (1-\varepsilon)\frac{dr_n}{dt}. \tag{2.19}$$

This relation is consistent with the entrainment which occurs in the nose since there is a vertical shear in the flow (figure 2.3). The conservation of buoyancy requires that

$$2\pi \int_0^{r_n} r h(r,t) \overline{g'}(r,t) dr = B. \tag{2.20}$$

Guided by the scalings given in (2.1) - (2.4), it may be shown that in the simplified situation in which α, β and γ are assumed to be constant and independent of position, then these equations have self-similar solutions of the form

$$h(r,t) = \mathcal{H} H \left(\frac{r_o}{r_n}\right)^{\frac{1}{4}} \eta^{\omega}; \tag{2.21a}$$

$$\overline{g'}(r,t) = \mathcal{G}\frac{B^{\frac{1}{2}}}{tH}\left(\frac{r_o}{r_n}\right)^{-\frac{1}{4}} \eta^{2-\omega}; \tag{2.21b}$$

$$\bar{u}(r,t) = \mathcal{U} B^{1/4} t^{-\frac{1}{2}} \eta. \tag{2.21c}$$

where $\eta = r/r_n(t)$, $r_n(t) = \mathcal{R} B^{1/4} t^{1/2}$ and ω, $\mathcal{G}, \mathcal{H}$, and $\mathcal{U}$ are constants. Equations (2.17a), (2.17c), (2.19) and (2.20) then require that

$$\mathcal{G}\mathcal{H} = \frac{2}{\pi \mathcal{R}^2} \quad ; \tag{2.22a}$$

$$\mathcal{U} = \frac{(1-\varepsilon)\mathcal{R}}{2} \quad ; \tag{2.22b}$$

$$\alpha = \frac{1}{1-\varepsilon} \quad ; \tag{2.22c}$$

$$\omega = \frac{8\varepsilon - 7}{4\varepsilon} \quad \text{and} \tag{2.22d}$$

$$Fr = \frac{\mathcal{R}}{(4\mathcal{G}\mathcal{H})^{1/2}}. \tag{2.22e}$$

Note that this solution is consistent with (2.17b) and can be used to determine the pressure.

Given we have found $\mathcal{R} = 1.28 \pm 0.05$ and $\varepsilon = 0.33 \pm 0.09$ (figures 2.4, 2.5), the solution (2.21)-(2.22) suggests that $\mathcal{U} = 0.42 \pm 0.1$, $\alpha = (1-\varepsilon)^{-1} = 1.5 \pm 0.2$, $Fr = 1.0 \pm 0.1$ and $\omega = 3.3 \pm 1$. This estimate for the Froude number, $Fr = 1.0 \pm 0.1$ overlaps with the independent measurement of Fr shown in figure 2.5b, 0.86 ± 0.07, although is a little higher.

These simplified similarity solutions which conserve the total buoyancy, do therefore capture the speed and the buoyancy of the front, as well as the gradual increase in the total volume through entrainment. In figure 2.6(c, d), we compare the dimensionless solutions 2.21 $h(r,t)/h(r_n,t) = \eta^{\omega}$ and $\overline{g'}(r,t)h(r,t)/\overline{g'}(r_n,t)h(r_n,t) = \eta^2$ with the experimental measurements of the depth and vertically averaged buoyancy along the current (2.5). As expected, the simplified solutions do not capture the full structure of the head, which is strongly influenced by the recirculation, but they do predict an increase in depth and buoyancy towards the front of the flow. It may be that by

accounting for some variation in the shape factors α, β, γ in the head of the current, more of the structure may be determined, although this is beyond the scope of our measurements. Also, as r_n increases, figure 2.6a suggests that the flow evolves from such a self-similar constant buoyancy solution owing to the gradual loss of buoyancy from the head into the wake (cf. figure 2.6a).

2.6 Discussion

We have presented a new suite of experiments in which we measure the nose speed and the depth and evolving buoyancy throughout an axisymmetric gravity current produced by the release of a finite mass of dense fluid from behind a lock gate. We find that as the current advances it entrains a fraction 0.33 ± 0.09 of the ambient fluid which is displaced over the head of the flow. The current includes a region of recirculation near the head, which drives this mixing. To good approximation, the position and depth of the head follow the scaling laws $r_n \sim (1.28 \pm 0.05)B^{1/4}t^{1/2}$, $h_n \sim 0.5H\,(r_o/r_n)^{1/4}$ and the effective Froude number of the head of the flow is about 0.86 ± 0.07.

A depth averaged model for the flow which accounts for the entrainment at the front, and the vertical shear in the velocity and buoyancy, leads to some new self-similar solutions which predict the increase in volume of the current with time, and also the increase in depth and salt content towards the front of the flow. However, the simplified model does not capture all the detailed structure of the recirculating flow in the head.

Our experiments have focussed on flow spreading in a sector of a circle with angle 9.5° in order that we can measure the buoyancy using the light attenuation technique (figure 2.1). Numerical simulations by Cantero *et al.* (2007*a*) for a fully axisymmetric current illustrate the importance of the vortex ring structures which stretch and break up in the azimuthal direction. It would be interesting to develop an experimental technique to measure the mixing in such fully axisymmetric gravity currents for comparison with the present work.

The mixing process we have described has numerous implications for large-scale density driven flows in nature and the environment whose Reynolds numbers are sufficiently high ($Re > 5000$). For example, in a current produced by a sudden release of dense gas, we predict that the concentration in the head will rapidly fall to 0.2 - 0.3 of the initial value as the flow spreads to distances of 6 - 7 times the original size of

the gas release (figure 2.2b). This modelling can therefore inform hazard assessment associated with dangerous concentrations of the gas. The work also has important implications for more complex geophysical and geological flows, and this will form the topic of further research.

Chapter 3

Steady flux axisymmetric gravity currents

3.1 Abstract

We present new experiments to measure the rate of entrainment of ambient fluid into a high Reynolds number, axisymmetric, turbulent gravity current. A steady flux of aqueous salt solution is initially generated as a descending forced plume. This evolves into a gravity current upon its impingement on the floor. It then propagates into a diverging channel of angle 9.5°, filled with fresh water resulting in effective source Froude numbers, Fr_o, in the range 1 - 2. A light attenuation technique is used to measure the evolving buoyancy of the flow as it propagates and mixes with the ambient fluid. Dye studies are conducted to illustrate the mechanisms of mixing. The front position increases with time as, $r_n \approx 1.33 B_o^{1/4} t^{3/4}$. Behind the head, the steady body is observed. Time-averaged velocity profiles are estimated using a Radon transform to track structures within this region. Fluid along the back is found to entrain along the top boundary of the body region with entrainment coefficient of 0.03-0.09. At the front, a fraction of fluid being displaced by the front propagation is entrained into the head of the current slightly decreases from 0.22 ± 0.01 to 0.18 ± 0.01 as Fr_o increases from 1.0 to 1.8. The front position and current depth is then compared to a previously proposed theoretical model (Johnson *et al.*, 2015).

3.2 Introduction

Turbulent gravity currents arise when dense fluid spreads under gravity along a horizontal boundary displacing a less dense fluid. Gravity currents are found in many environmental and geophysical flows including the dense gas flow, fronts between warm and cold air, dense ash flows and turbidity currents on the sea floor (see Simpson, 1999). There have been many studies of dynamics of such flows using a combination of mathematical models and experimental techniques to understand the dynamics of these flows (Kneller & Buckee, 2000; Prandtl, 1952; Simpson, 1999; Sparks *et al.*, 1997). In studying the motion of gravity currents, there are end member models representing currents produced by a sudden release of dense gas following an explosion, or a continuous source of dense fluid from a large reservoir.

Many experimental studies have focussed on two-dimensional flows spreading along a flume, generated by the release of a finite volume from behind a lock gate (Fragoso *et al.*, 2013; Hacker *et al.*, 1996; Sher & Woods, 2015; Shin *et al.*, 2004) or, in some studies, a constant flux of dense fluid (Hogg *et al.*, 2005; Linden & Simpson, 1990).

An important aspect of experiments measuring the dynamics of gravity currents is that there is a substantial amount of mixing of the ambient fluid displaced by the flow into the head of the flow. Sher & Woods (2015, 2017) have studied this dilution in two dimensional gravity currents produced by a finite volume release and a continuous source of dense fluid, while Hallworth *et al.* (1996) and our works in chapter 2 measured this dilution in an axisymmetric current produced by the release of a finite volume of fluid. Hallworth *et al.* (1996) also found that with a constant flux of source fluid, the density of the head remained relatively high, and that it was not diluted to very low values through mixing. However, there was evidence of mixing. Numerical models of axisymmetric gravity currents (Cantero *et al.*, 2007*b*) have also found that there is mixing of ambient fluid into the flow. Here we present a series of new experiments using a light attenuation technique to measure the dilution of a gravity current produced by a constant localised source of dense fluid which spreads to form an axisymmetric current.

There have also been a number of theoretical models proposed in the literature in which it is assumed that there is no mixing of ambient fluid into the flow. The models also assume that the velocity and density are independent of depth within the flow. This leads to governing equations in which the characteristic speed of mass, momentum and buoyancy within the current are the same. It has been shown that

with uniform vertical profiles, the model does not admit similarity solutions with the scaling $r_n \sim B_o^{1/4} t^{3/4}$ for the position of the nose. Slim & Huppert (2011) and Johnson *et al.* (2015) proposed a model in which there is a discontinuity in the current just behind the head of the flow. This leads to the prediction that the head advances at a rate which scales as $r_n \sim B_o^{7/25} Q_o^{-1/25} t^{4/5}$, while the tail of the flow assumes a steady structure supplying fluid to the head. The predictions of such models can, however, change fundamentally if the density and velocity are not uniform with depth in the current, or if the mixing of ambient fluid into the head of the flow is included in the shallow water formulation. Measurement of the actual properties of the flow in experimental gravity currents can provide information about for the nature of such mixing and the vertical structure of the flow.

Although these flows have been studied in some detail, there remain some fundamental questions about mixing of ambient fluid into the current and the effect of this dilution on the dynamics. High resolution digital cameras can measure changes in light attenuation through a gravity current containing dye. In turn this can be used to make a map of the evolving density structure of a gravity current. Together with measurements of the vertical structure of the horizontal velocity in a gravity current, a picture can then be developed of the flow and mixing within a gravity current. This is the purpose of the present experimental work.

3.3 Experimental method

A series of laboratory experiments were performed in a Perspex radial sector tank of angle 9.5^o with maximum length of 300 cm (figure 3.1). The tank was filled with fresh water to the height of 36 cm. Saline solution of a known salt concentration, and hence density, was pumped into the tank through a hose directed vertically downwards with the nozzle tip located at 9 cm above the floor and a radial distance of 5-8 cm from the central corner of the tank. With the supply flux of dense fluid, a downward vertical jet is formed and is then converted into a gravity current once the jet reaches the bottom of the tank. The initial buoyancy associated with this source fluid is given by $g'_j = g(\rho_s - \rho_w)/\rho_w$, where g is the acceleration due to gravity, ρ_s is the density of the initial saline solution and ρ_w is the density of the fresh water (ambient fluid). Subscript j denotes the properties of the jet source. The mean flow rate was calculated from the volume of fluid being fed into the experimental tank over the total time for each experiment and converted to the equivalent flow rate per radian, Q_j, as reported

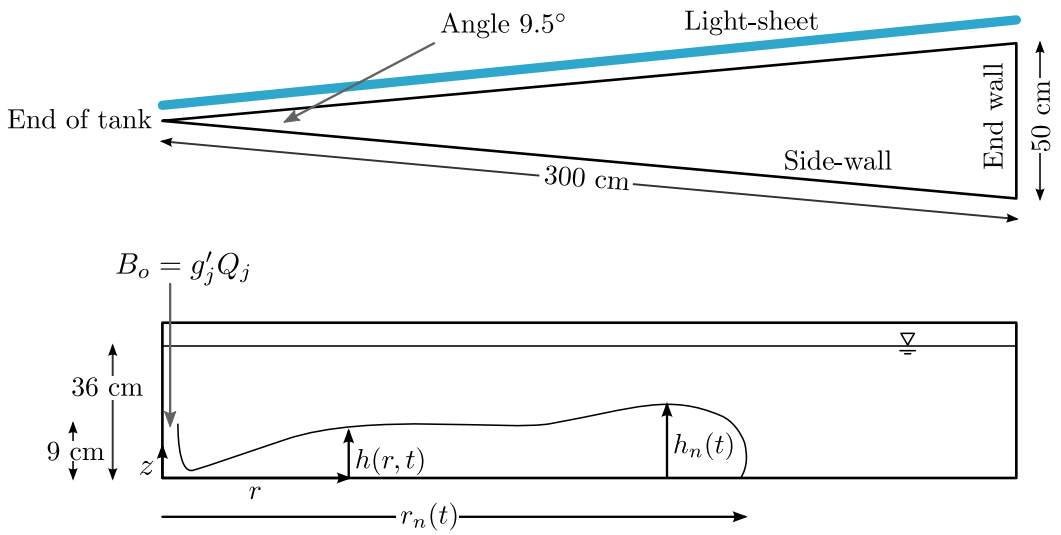

Fig. 3.1 Schematic diagram showing the top and side views of the experimental tank.

Exp.	g'_j (cm s^{-2})	Q_j $\times 10^3$ (cm^{3}s^{-1}rad^{-1})	$\overline{g'_o}$ (cm s^{-2})	Q_o $\times 10^3$ (cm^{3}s^{-1}rad^{-1})	Fr_o	$\langle Fr_n \rangle$	$\langle \mathcal{R}_C \rangle$	type of experiment	
A	84.07	1.12	14.15	6.63	1.15	0.81	1.31	a	●
B	69.36	1.06	12.03	6.11	1.11	0.77	1.32	a	●
C	54.84	1.07	9.58	6.14	1.21	0.79	1.34	a	●
D	46.21	1.10	7.24	7.02	1.16	0.74	1.29	a	●
E	26.29	1.09	4.29	6.69	1.44	0.72	1.30	a	●
F	12.26	1.15	1.72	8.19	1.51	0.65	1.25	a	●
G	69.36	1.71	21.96	5.42	1.09	0.92	1.37	a	●
H	41.89	1.65	11.26	6.15	1.29	0.88	1.38	a	●
I	12.26	1.67	2.48	8.24	1.75	0.75	1.34	a	●
J	26.29	2.58	n/a	n/a	n/a	n/a	n/a	b	
K	54.84	2.17	n/a	n/a	n/a	n/a	n/a	c	
L	54.84	2.21	n/a	n/a	n/a	n/a	n/a	b,c	

Table 3.1 Table of experiments illustrating the range of initial volumetric flux and buoyancy used in this study. The quantities Fr_o, $\mathcal{R}_C$ and Fr_n are properties of the current which are defined in section 3.4.1, 3.5.1 and 3.5.2, respectively. In the table, for each experiment, we list the asymptotic values of Fr_n, $\mathcal{R}_o$ for $\hat{t} > 5$. The colour codes given for experiments A-I are used in the subsequent plots in this chapter.

in table 3.1 and the source buoyancy flux can be determined from the product of the two, $B_o = g'_j Q_j$. On entering the tank the fluid descends from the nozzle to form a forced plume, which entrains some ambient fluid. As this reaches the base of the tank, the flow begins to spread radially along the base of the tank forming a gravity current. There is a considerable amount of mixing prior to the flow becoming horizontal and so we measure the flow following the mixing to provide the source conditions for the ensuing gravity current.

To visualise and track the flow, the tank was back-lit by a matrix LED light panel (W&Co Displays and Signs). A series of images of the experimental currents were taken using a D90 RGB DSLR camera (2 photos per second with shutter speed 1/100 s, 4.8 aperture and ISO 400) located approximately 6 m away from the tank.

In each experiment, a known amount of red TRS food dye was added to the aqueous salt solution. The instantaneous height of the current, $h(r, t)$, can be measured based on a threshold light intensity (appendix A). As the current mixes with the clear ambient fluid, the dye intensity falls. The amount of light absorbed by the dye depends on the concentration. Prior to each experiment, a calibration curve was generated using a systematic series of diluted solutions, for each of which we measured the light attenuation. Following an approach analogous to Hacker *et al.* (1996) and in chapter 2, the light intensity images were converted into dye concentration using a MATLAB script. The dye concentration is directly proportional to the salt content of the fluid, averaged across the tank. Since the width of the tank increases with radius, fluid with the same dye concentration appears darker in the region of larger width. Thus, the conversion from light attenuation to dye concentration was performed locally in each small area spanning 1 cm $\times$ 1 cm of the tank wall, using different local calibration curves. The buoyancy data are span-wise averages. Given the small angle subtended by the two side walls of the experimental tank, the variation in the radius across a span is as small as 0.5% of the radius and so the data provides an approximation for the radial distribution (azimuthal averaged) of buoyancy (chapter 2). By measuring the total mass of dye in the system compared to the original mass of dye in the injected fluid we estimate the light attenuation technique is accurate to within an error of 10% (appendix A).

To visualise how the mixing occurs, a series of additional experiments were conducted in which small parcels of dye were injected into (i) fluid within the current, or (ii) the ambient fluid. By tracking the motion of this dye, we obtain a Lagrangian picture of the flow field and can infer the process of mixing ambient fluid into the flow.

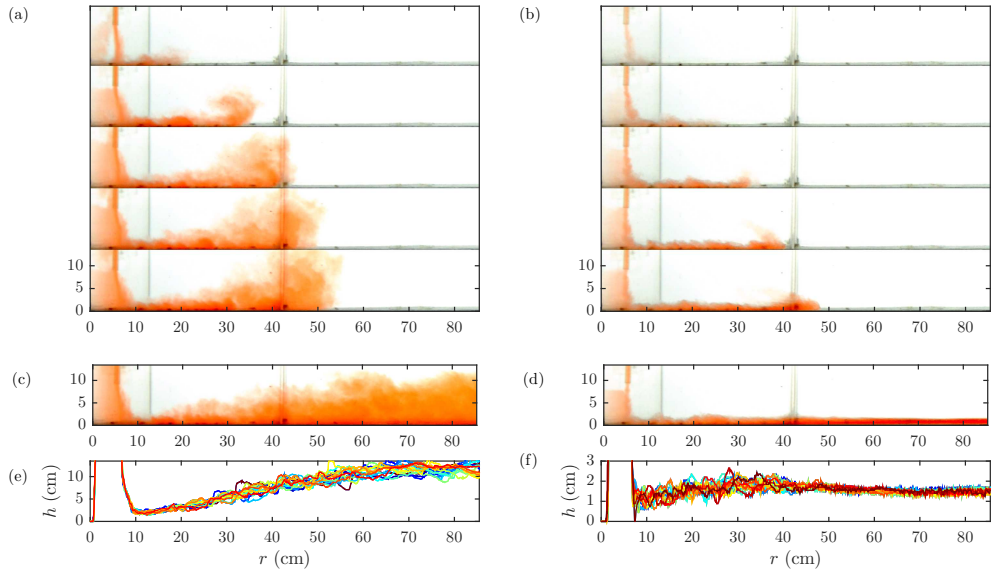

Fig. 3.2 Photographs of the currents near the source region ($r < 85$ cm) comparing the initiation of the flow generated from high and low, Q_j, in the left and right panels, respectively. In (a), the head may grow as big as 10 cm compared to (b) which develop only small head and the current appears to be laminar. Panels (c) and (d) show a photograph of the corresponding currents at large time. Panels (e) and (f) show the height profile at $t = 12.5 - 20$ s within the region $r < 85$ cm. During this time, the head of the current has already propagated downstream beyond the scope of the panel. The height profiles show that behind the head, the depth of the current appears to be quasi-steady.

3.4 Experimental observations

3.4.1 Current development near the source

Once the dense fluid exits the nozzle, it forms a buoyant jet that impinges on the floor beneath and spreads laterally. The fluid then travels horizontally away from the apex forming an axisymmetric gravity current. For currents with sufficiently large Q_j ($> 1 \times 10^3$ cm^{3}s^{-1}rad^{-1}), the supply fluid forms a strong vortex at the front (figure 3.2a). Fluid supplied from the source appears to accumulate near the front and the head starts to grow. After a couple of seconds, a steady body region is formed behind the head. Figure 3.2(c,e) shows that within this steady region, the height of the flow increases approximately with radius, r, for $0 < r < 60$ cm. Subsequently at larger r, the height h becomes approximately constant along the length of the current except in the region immediately behind the leading front of the flow where it is slightly larger.

The Reynolds numbers, $Re = u_n h_n/\nu$, where u_n is the speed of the leading front, h_n is the maximum depth near the front region and ν is the kinematic viscosity of the head have been estimated to have a value in excess of 8000 for all experiments with $Q_j > 1 \times 10^3$ cm^{3}s^{-1}rad^{-1}. An experiment with smaller Q_j ($\sim 1 \times 10^2$ cm^{3}s^{-1}rad^{-1}) has been attempted (figure 3.2b,d,e) but the current has $Re \sim 750$. This suggests that the flow is laminar and thus, is not included in this study.

Our main interest in the present work is the evolution of the flow as it spreads out over the floor of the tank. We have therefore measured the flow rate just downstream of this inflow adjustment region, in order to estimate the effective source conditions for the ensuing gravity current. In all experiments, a steady deepening region of the current develops in the region $r < 60$ cm for all experiments (figure 3.2c) and so $r = 60$ cm was chosen to be the representative radius where the inflowing current has adjusted and the flow downstream evolves as a gravity current. We define the effective buoyancy after the inflow mixing one to be the average buoyancy at $r_o = 60$ cm,

$$\overline{g'_o} = \frac{\int \langle g'(r_o, z) \rangle \mathrm{d}z}{h_o}, \tag{3.1}$$

where $\overline{\cdot}$ denotes spatial averaging, $\langle \cdot \rangle$ denotes time averaging and $h_o = \langle h(r_o) \rangle$. To ensure that the unsteady head region is not included in the calculation for ensemble average in (3.1), only data at large time when $r_n > 150$ cm is used. The subsequent effective source for the gravity current after the inflow mixing zone can be determined from $B_o = g'_j Q_j = \overline{g'_o} Q_o$ as the buoyancy must be conserved. From this, we may determine the depth averaged fluid velocity at r_o knowing $Q_o = \bar{u}_o h_o r_o$. For each current, the Froude numbers based on the effective source conditions are calculated using

$$Fr_o = \frac{\bar{u}_o}{(\overline{g'_o} h_o)^{1/2}}. \tag{3.2}$$

These effective source conditions are reported in table 3.1 for each experiment. It is found that although the buoyancy flux has been varied from ~ 20 cm^{4}s^{-3}rad^{-1} (exp. I) to ~ 120 cm^{4}s^{-3}rad^{-1} (exp. G), the effective source Froude number only varies within the range 1 - 2.

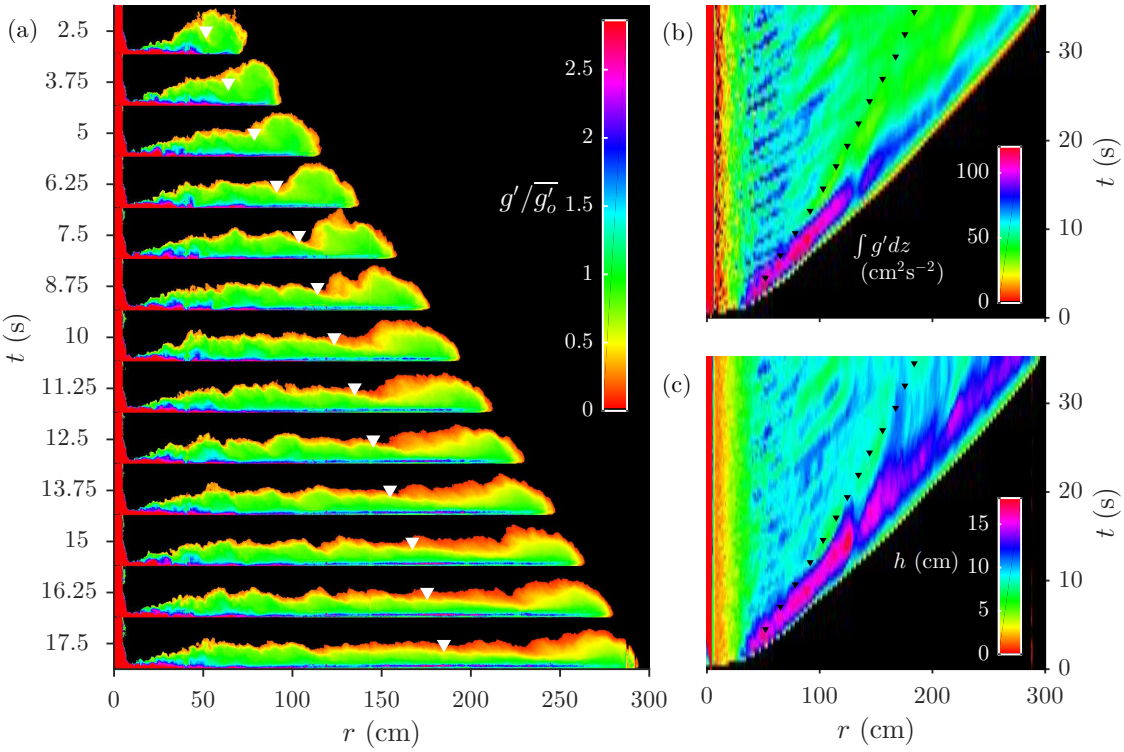

Fig. 3.3 (a) Photographs of a saline gravity current (exp. C) illustrating the evolution of the normalised buoyancy in the current, shown by false-colour contours, as it advances along the flume. Images are taken at time intervals of 1.25 s. Evolution of (b) the vertical integral of the buoyancy, $\int g'dz$, and (c) height, h, are shown as functions of radius on the x-axis and time on the y-axis. Near the front, the maximum integral buoyancy tends to decrease significantly while the maximum depth is approximately constant suggesting dilution within the front. The inverted triangles (black/white) indicates the separation at which 65% of total volume at each time is located. This boundary is later used in §3.6.3 to define the boundary between the head and the body of the current in our study.

3.4.2 Evolution of the flow

Figure 3.3a shows the time evolution of a gravity current for experiment C. The false colour corresponds to the buoyancy of the fluid in the tank, normalised by the effective source buoyancy, $\overline{g'_o}$. Following the inflow adjustment region, the current becomes very dilute relative to the source inflow, as shown in the region $r < 60$cm of figure 3.3a, which illustrates the change in flux within the adjustment region. With time, the head region develops a strong vortical structure that drives the dense fluid to reach the front and rise up over the head. The buoyancy of the fluid within the head is always as large as $\overline{g'_o}$ suggesting that dense fluid from the tail reaches the head. On arriving at the front, the dense fluid mixes with the ambient fluid and forms a diffuse and dilute wake, with $g' < 0.5g'_o$, that can be seen along the top boundary of the current after $t = 7.5$ s, $r \approx 150$ cm.

Figure 3.3b shows the evolution of vertical integral of the buoyancy to be compared with figure 3.3c, the depth of the current, with time. The fact that the depth near the front stays approximately constant while the vertical integral of the buoyancy decreases with distance from the source from approximately 100 to 75 cm^2s^{-1} confirms the importance of mixing in the head region.

3.4.3 Mechanism of mixing

Figure 3.4 shows the images from a current which is initially dyed yellow but which becomes colourless with time (experiments K). In this experiment, red and blue dyes are injected into the ambient fluid at $r = 125$ and 175 cm respectively. At $t = 10$ s, the yellow current head displaces the red ambient fluid, causing the red dye to rise up over the dense yellow head. A fraction of the red dye is entrained and mixes into the head. However, this mixed fluid is gradually left behind and a streak of red dye is left on top of the continuing current in the tail region. Similar behaviour can also be seen in the blue dye. The mixed fluid (red and blue) does not penetrate the whole depth of the current as the bottom-most part of the current remains of similar colour to that supplied from the source. This illustrates that the colourless source fluid, replenished from the source, is able to reach the head of the flow without significant dilution.

In figure 3.5a, we show another experiment in which the source fluid is also dyed yellow, but which is replaced with colourless source fluid part way through the experiment (experiment L), and in which the current displaces a parcel of blue dye in the ambient fluid. In figure 3.5b, the structure of the current is shown in the reference

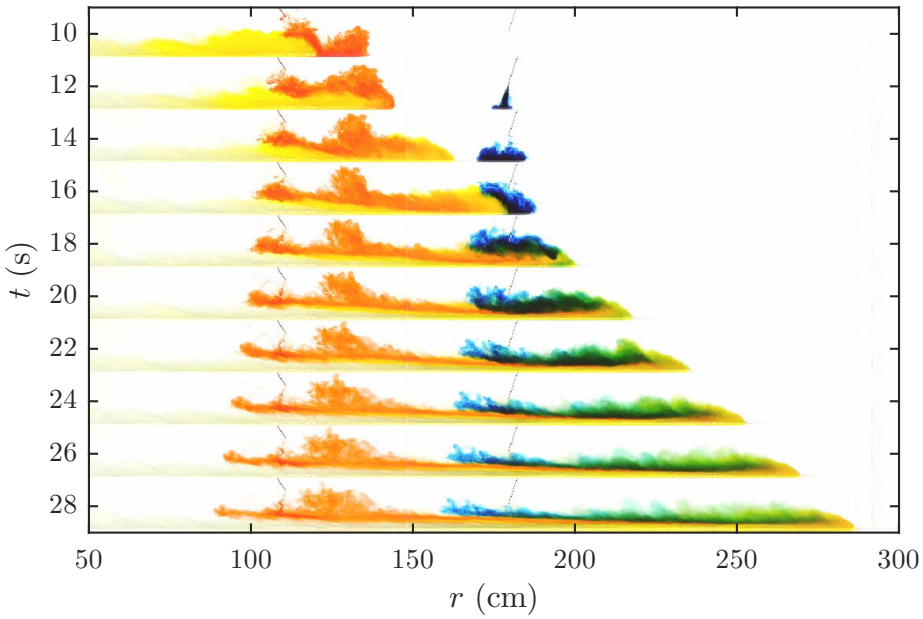

Fig. 3.4 A gravity current initially dyed yellow but which becomes colourless with time displaces a parcel of red dye located at $r = 125$ cm. Red dye is entrained into the head and travel together with the propagation of the front. The front then displaces blue dye located at $r = 175$ cm. The red and blue dyes do not seem to penetrate the whole depth as the bottommost of the current remains yellow-colourless during the whole flow.

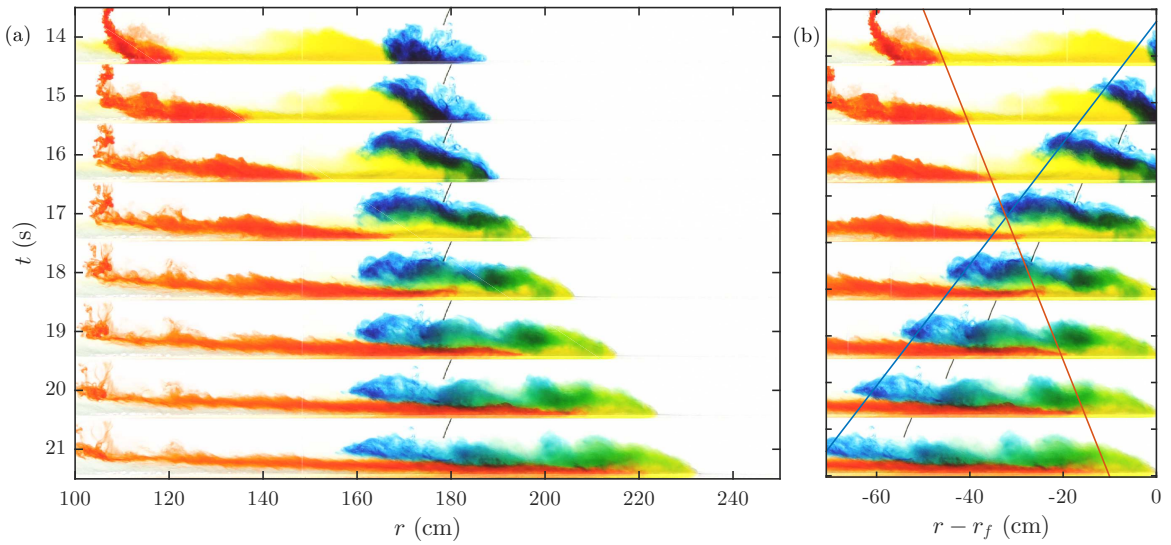

Fig. 3.5 (a) Photos displayed for $100 < r < 250$ cm shows blue dye being displaced by the head of yellow gravity current. A fraction of it mixes into the head and moves with the front of the gravity current. At the same time, red dye is injected behind the head into the body region but can eventually reach the front. Within the body, the fluid at the bottom appears to travel faster than the top part which can be seen by the shear of injected red dye. (b) The same current but is shown relative to front of the current. The advance of the red and blue dyes are traced and shown in the corresponding lines.

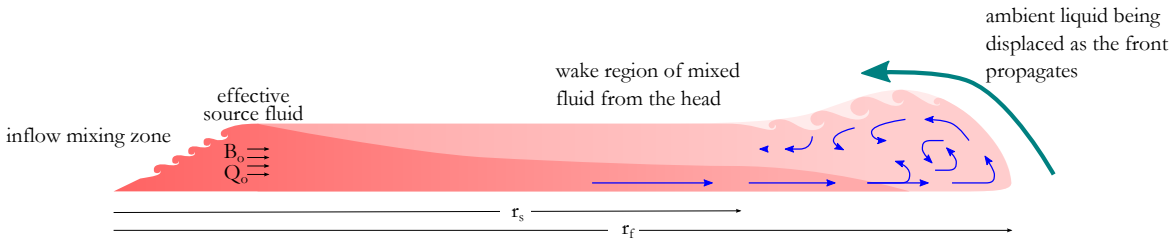

Fig. 3.6 Schematic diagram of mixing in an axisymmetric gravity current.

frame of the head of the current. While the blue dye is being displaced, red dye was injected into the current at the tail approximately 45 cm behind r_n. The red fluid quickly moves towards the head and enters the head region at $\sim$ 20 cm behind the leading front. The red dye continues to travel downstream and eventually reaches the leading front where it starts to roll up, mix with the ambient and recirculate. The dense fluid (red) and the wake formed by the fluid left behind as the head region (blue) do not appear to mix very intensely but appear to form two distinct layers. Figure 3.6 illustrates the overall flow pattern of the dynamics of the flows in axisymmetric gravity currents as observed in these experiments.

3.5 The properties near the front

3.5.1 Front position, r_n

In order to interpret our results, it is useful to compare our results with theoretical models of gravity currents produced by a steady source of fluid. One of the classical approaches to model the motion of gravity currents has been to use dimensional analysis. With a constant source volume flux Q_o and buoyancy flux B_o, the position of the nose, $r_n(t)$, can be expressed in terms of the dimensional relation

$$r_n = B_o^{1/4} t^{3/4} f\left(B_o^{3/4} t^{5/4}/Q_o\right) \tag{3.3}$$

where the dimensionless grouping $B_o^{3/4}t^{5/4}/Q_o$ illustrates that the flow may depend on both the initial buoyancy flux and the initial volume flux. The scaling $r_n = \lambda B_o^{1/4} t^{3/4}$ is consistent with the concept that the flow is independent of the source volume flux (Bonnecaze *et al.*, 1995; Britter, 1979; Kaye & Hunt, 2007), but the dimensionless group, $B_o^{3/4}t^{5/4}/Q_o$, shows that the evolution of the flow can also depend on the source volume flux, as shown by Sher & Woods (2017) in the case of a two-dimensional gravity current. Normalising the length and time scales based on the volume and buoyancy flux, $L = (Q_o^3/B_o)^{1/5}$ and $T = (Q_o^4/B_o^3)^{1/5}$, the non-dimensional position of the fronts can be written as

$$\hat{r}_n(\hat{t}) = \hat{t}^{3/4} f(\hat{t}) \tag{3.4}$$

where $\hat{r}_n L = r_n$ and $\hat{t}T = t$. In contrast to this conventional power law, Slim & Huppert (2011) argued that the evolution of an axisymmetric gravity current is rather

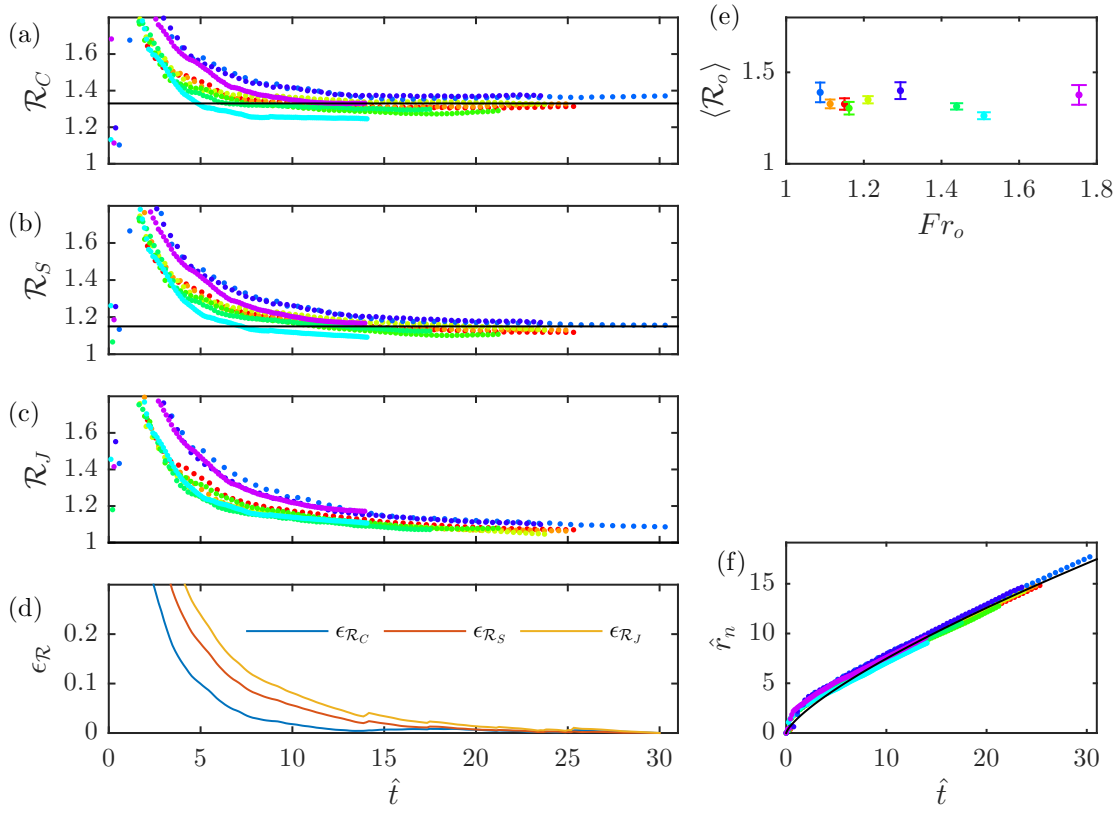

Fig. 3.7 (a-c) The ratio of the coefficients provided by different power laws (3.6) have been compared. Black lines in (a) and (b) show the averaged values of the asymptotic $\mathcal{R}$ for different experiments while $\mathcal{R}_J$ does not seem to converge to a constant within our range of study. (d) Deviations of $\mathcal{R}$ to the associated asymptotic values, $\mathcal{R}(\hat{t}_{\max})$. It appears that $\mathcal{R}_C$ converges to its asymptotic value faster than $\mathcal{R}_S$ and $\mathcal{R}_J$. (e) The time averaged (with error bars representing standard deviation) ratios from the conventional power law: $r_n \sim t^{3/4}$ as a function of Fr_o for $\hat{t} > 5$. (f) The frontal position as a function of time. The black line shows the predicted r_n using $r_n = 1.33 B_o^{1/4} t^{3/4}$. For (a-c) and (e), the results from different experiments are plotted in different colours as coded in table 3.1.

non-self-similar and suggested instead that $\hat{r}_n(\hat{t}) \sim \hat{t}^{4/5}$. Later, Johnson *et al.* (2015) commented that their solutions do not satisfy the conditions at the rear of the head exactly. They suggested that the next largest term should also be included which consequently leads to the front positions to be in the form

$$\hat{r}_n(\hat{t}) = r_{no}\hat{t}^{4/5} + r_{n1}\hat{t}^{3/5} + O(\hat{t}^{2/5}), \tag{3.5}$$

where r_{no} and r_{n1} are some constants that depend on frontal Froude number, Fr_n, source Froude number, Fr_o, and source radius, r_o. Exact expressions for r_{no} and r_{n1} based on these parameters are shown in §3.7.1.

In figure 3.7a, we have plotted the value of the ratio $\mathcal{R}_C = \hat{r}_n/\hat{t}^{3/4}$, associated with the conventional power law, as a function of normalised time, $\hat{t}$, for different experiments (shown as different colours as coded in table 3.1). The figure suggests that after an initial transient, $\mathcal{R}_C$ asymptotes to a constant. The value of the constant varies within the range 1.25-1.38 for the currents with Fr_o of 1.0-1.8. (figure 3.7e) with the averaged value of 1.33. This is consistent with previous experimental studies (Britter, 1979; Kaye & Hunt, 2007).

Figure 3.7b and c show evolution with time of the experimental values of the ratios $\mathcal{R}_S = \hat{r}_n/\hat{t}^{4/5}$ and $\mathcal{R}_J = \hat{r}_n/(r_{no}\hat{t}^{4/5} + r_{n1}\hat{t}^{3/5})$, which are associated with the non-self-similar models suggested by Slim & Huppert (2011) and Johnson *et al.* (2015), respectively. For the latter model (figure 3.7c), r_{no} and r_{n1} are calculated for each experiment based on their corresponding Fr_n (see §3.5.2), Fr_o and r_o. The expressions for the ratios associated with the three models can be summarised as

$$\mathcal{R}_C(\hat{t}) = \frac{\hat{r}_n(\hat{t})}{\hat{t}^{3/4}}; \quad \mathcal{R}_S(\hat{t}) = \frac{\hat{r}_n(\hat{t})}{\hat{t}^{4/5}}; \quad \mathcal{R}_J(\hat{t}) = \frac{\hat{r}_n(\hat{t})}{r_{no}\hat{t}^{4/5} + r_{n1}\hat{t}^{3/5}} \quad . \tag{3.6}$$

Figure 3.7d shows the difference between the scaling and the experimental data over experiments A-I of the three ratios to their corresponding asymptotic value calculated for each experiment, $\mathcal{R}(\hat{t}_{\max})$. This is in the form

$$\epsilon_{\mathcal{R}}(\hat{t}) = \frac{1}{N}\sum_{i=1}^{N}\sqrt{\left(\frac{\mathcal{R}(\hat{t}) - \mathcal{R}(\hat{t}_{\max})}{\mathcal{R}(\hat{t}_{\max})}\right)^2}, \tag{3.7}$$

where N is the number of the experimental data, $\mathcal{R}$ is each different ratio of the experimental and predicted value of r_n (3.6) and $\mathcal{R}(\hat{t}_{\max})$ is the asymptotic value calculated using the mean of the last 5 data points for each $\mathcal{R}$. The square root

represents the deviation of each $\mathcal{R}(\hat{t})$ from their corresponding asymptotic values. The time series are then averaged over different experiments A-I.

It is worth noting that each experiment is normalised by different time and length scales, leading to calculated $\mathcal{R}$ being valid at different values of $\hat{t}$ for each experiment. To estimate the averaged profiles of the ensemble over the nine experiments (figure 3.7d) using (3.7), we first interpolated the data within the range $\hat{t} < \hat{t}_{\max}$ for each experiment so that $\mathcal{R}$ can be determined at any $\hat{t} < \hat{t}_{\max}$. However, with increasing $\hat{t}$, there are fewer available experimental data to calculate the ensemble averaged profiles. This leads to slight anomalies at $\hat{t}_{\max}$ of each experiments, such as $\hat{t} \approx 14$, when the experiment I (denoted by •) ended. Nonetheless, the ensemble averages of these $\epsilon_{\mathcal{R}}$ curves can illustrate and compare the accuracy of these different models used to describe the front propagation.

From figure 3.7d, it can be observed that all the power laws tend to converge to their corresponding values at large time. However, it seems that $\mathcal{R}_C$ (blue) associated with the conventional power law converges to the asymptotic value faster than $\mathcal{R}_S$ (red) and $\mathcal{R}_J$ (yellow). For example, by the time $\hat{t} = 5$, $\mathcal{R}_C$ already approaches 10% of its asymptotic value while the corresponding time for $\mathcal{R}_S$ and $\mathcal{R}_J$ to approach the 10% of their asymptotic values are at $\hat{t} = 8$ and $\hat{t} = 10$, respectively.

3.5.2 Frontal Froude number

By knowing the positions of the nose of the currents, we can calculate the frontal speed using the relation, $u_n = \mathrm{d}r_n/\mathrm{d}t$. Figure 3.8a shows the result for the instantaneous front speed normalised by velocity scale, $L/T = (B_o^2/Q_o)^{1/5}$, as a function of normalised time. The scaled data appear to collapse to a single curve which can be approximated by differentiating equation 3.4 which is plotted in the figure for comparison.

We used the data from light-attenuation experiments to calculate the maximum value of the vertical integral of the buoyancy, $(\overline{g'}h)_n$, as a function of position along the current which is found to occur near the front (figure 3.3c). Combining these results, we calculate the Froude number of the head, Fr_n, as given by

$$\frac{\mathrm{d}r_n}{\mathrm{d}t} = Fr_n(\overline{g'}h)_n^{1/2} \quad \text{where} \quad (\overline{g'}h)_n = \max\left(\overline{g'}h = \int_0^{h(r)} g'\mathrm{d}z\right) \tag{3.8}$$

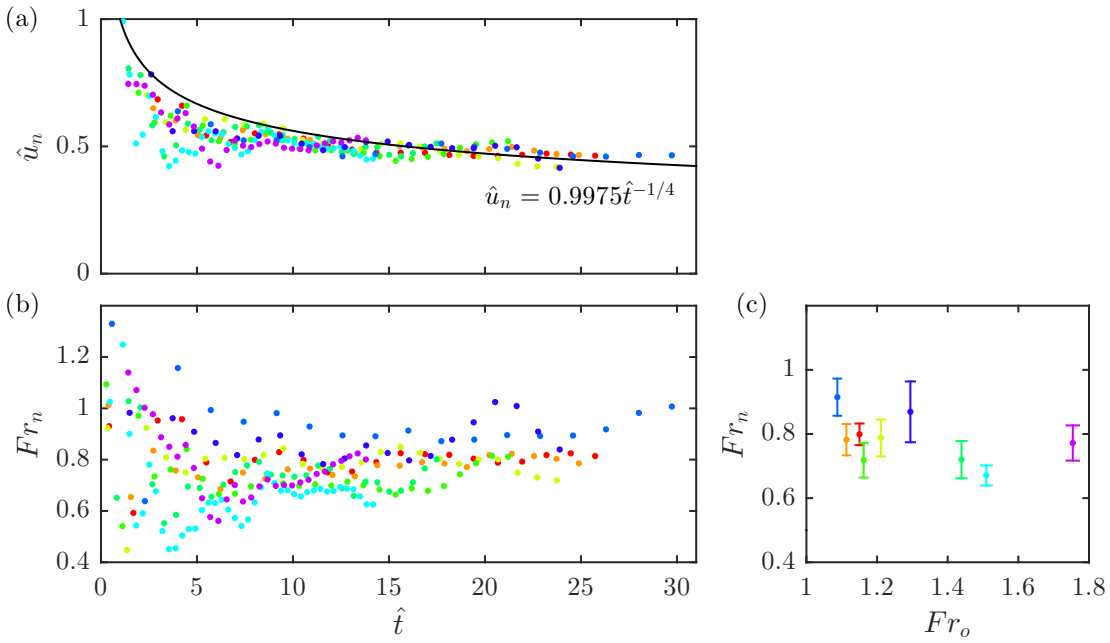

Fig. 3.8 Variation as a function of normalised time of (a) instantaneous frontal velocity together with predicted frontal velocity based on conventional scaling: $\hat{r}_n = 1.33\hat{t}^{3/4}$, shown in black line; and (b) frontal Froude numbers estimated from the experimental data. (c) Time-averaged for $\hat{t} > 5$ for experimental frontal Froude numbers as a function of the effective source Froude numbers. Colours represent results from different experiments as coded in table 3.1.

For each experiment, Fr_n appear to converge to a constant of the value within the range 0.7-1.0. The time-averaged Fr_n after $\hat{t} > 5$ show that Fr_n slightly decreases from 0.92 ± 0.07 to 0.75 ± 0.09 with increasing Fr_o from 1.09 to 1.75.

3.6 Entrainment coefficients

3.6.1 Estimating velocity profiles

Figure 3.3(b,c) show that there is a regular series of fronts moving downstream towards the front of the current. The gradient of these fronts varies with radius but is approximately the same at all times. The false-colour contrast for these fronts decreases at larger r and becomes indistinguishable to the background buoyancy beyond $r > 150$ cm. These fronts can be interpreted as the apparent front of the eddies generated by the effective source which mix and become diluted with the surrounding fluid. The successive fronts can also be observed by plotting an equivalent time series of g' at different depth, z, which is shown in figure 3.9(a).

The speed of these fronts can be determined by using Radon transform (Murphy, 1986) which estimates the gradient of straight lines observed in these time series of g'. If we write this image as a function of radius and time, $f(r,t)$, the Radon transform computes the line integrals of this function along parallel paths in a certain direction. Such a projection can be determined along any angle, θ. In general, the mathematical representation for the Radon transform of $f(r,t)$ will be the line integral of f parallel to the t'-axis

$$R_\theta(r') = \int_{-\infty}^{\infty} f(r'\cos\theta - t'\sin\theta, r'\sin\theta + t'\cos\theta)\mathrm{d}t'$$

where

$$\begin{bmatrix} r' \\ t' \end{bmatrix} = \begin{bmatrix} \cos\theta & \sin\theta \\ -\sin\theta & \cos\theta \end{bmatrix} \begin{bmatrix} r \\ t \end{bmatrix}$$

and is graphically illustrated in the figure 3.9(b). Applying this concept to our data, we follow the Radon transform algorithm using a built-in Matlab Radon function for image-processing which first divides pixels, $f(r,t)$, into four sub-pixels prior to projecting each sub-pixel separately 3.9(c). By remapping our image into a Radon domain, the angle at which high-valued pixels are aligned will have a high value in the Radon domain since there are many high-valued pixels involved in the integration. In contrast, the integration along other directions will be lower as it results from the sum

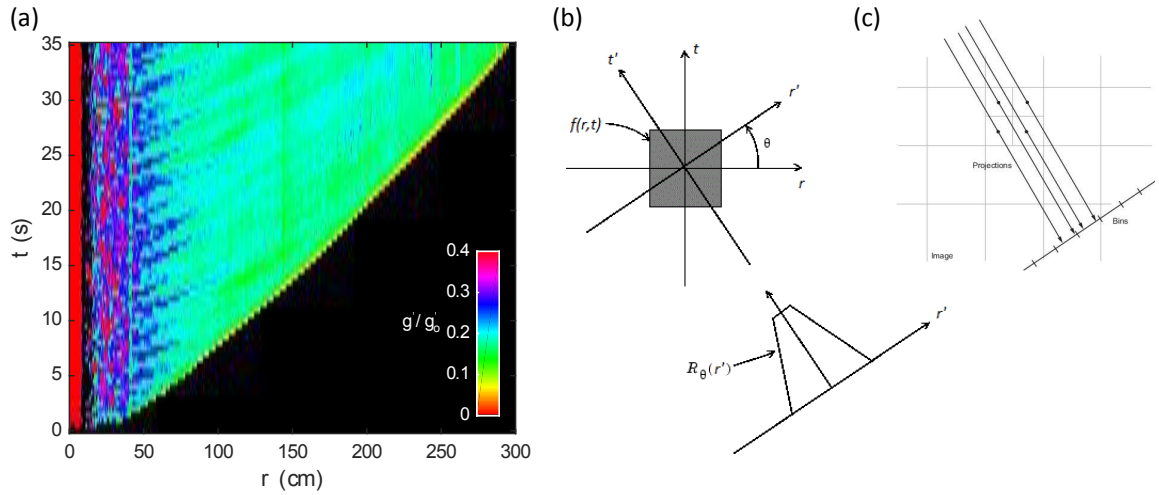

Fig. 3.9 (a) Time-series image of buoyancy, g', at $z = 2$ cm. Successive eddies can be seen in the image as streaks dense liquid (blue) on top of the background buoyancy (green). (b) Graphical illustration of how time-series image, $f(r,t)$, can be transformed into a Radon domain, $R_\theta(r')$. (c) Following the built-in Matlab Radon transform function, the image pixels are first divided into four sub-pixels before being remapped into the projected axis.

of both low and high-valued pixels. By detecting the angle at which the maximum integration occurs, we can infer this as the gradient of the features in the original image, $f(r,t)$. The angles associated with the 97% of the maximum integrations have also been determined to give the reliability for each estimated dominant angle. However, as we notice that the slopes of these features, though approximately independent of time, seem to vary with radial distance from the source. For each time series of g' at a particular depth, we used a window of ± 10 cm around each selected r to estimate time-averaged velocity at each depth and radius, $\langle u(r,z)\rangle$, in the region $60 < r < 150$ cm.

Figure 3.10 shows the estimated (time-averaged) velocity and buoyancy profiles at $r = 60, 80, 100, 120$ and 140 cm for experiment A. Our data shows that beyond the adjustment region, the flow has become stratified both in buoyancy and radial velocity. The maximum buoyancy is located just above the floor while the maximum velocity seems to be located at a slightly higher level. Above their maximum value, the buoyancy and velocity decrease upwards. The buoyancy profile may reach zero slightly above the time-averaged depth of the current (yellow line) due to depth fluctuation. Near the top surface, tracking eddies becomes difficult as the buoyancy contrast to the background becomes small. Fluid velocity outside the flow cannot be measured using our experimental technique and thus, the depth at which the fluid radial velocity

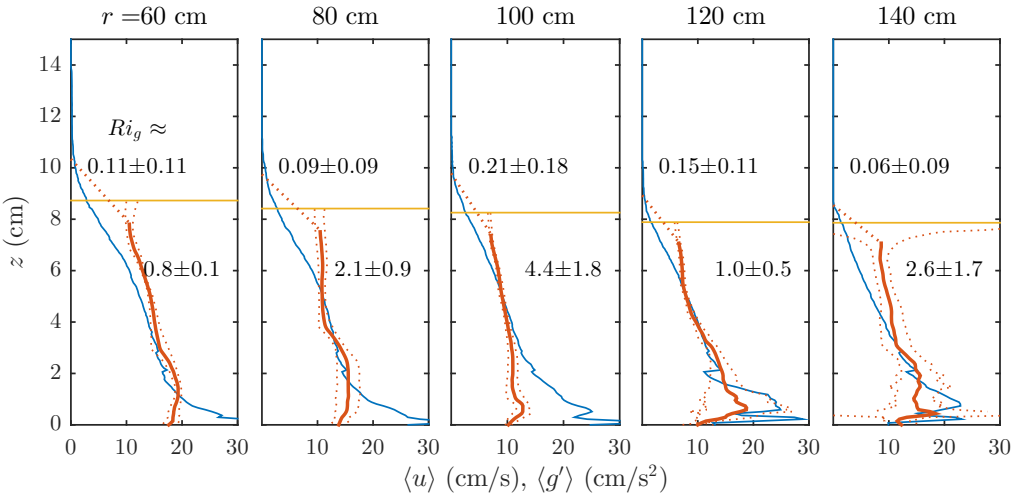

Fig. 3.10 Vertical profiles of time-averaged velocity (red) and buoyancy (blue) of fluid within the body region of the gravity current. The red dotted lines show the error bounds associated with the predicted velocity profiles. The yellow lines show the time-averaged depth, h_r, of the current at the corresponding radial position. The fluctuation in depth of the current leads to non-zero buoyancy above this height. Near the top boundary, tracking eddies fails to suggest reliable speed of the flow. Hence, velocity profiles are extrapolated from the velocity at $z = 0.9h_r$ and assumed to reach zero where time-averaged buoyancy reaches zero. The numbers show the gradient Richardson number, Ri_g, associated to the two regions: $z > 0.9h_r$ and $0.1h_r < z < 0.9h_r$, calculated using the averaged gradient corresponding to each zone.

becomes zero is uncertain. One might suggest that it may be above the time-averaged depth of the current as the current may drag the ambient fluid above it. However, by tracing injected dye parcels in planar gravity currents, Sher & Woods (2017) found that the detected velocity becomes zero at about the depth of zero buoyancy. We assume that this is also true for radial velocity in our studies and the velocity profiles in the region $z > 0.9h_r$ are extrapolated based on this assumption. The difficulty in determining speed also occurs at large r, where the buoyancy contrast between eddies to the background becomes small. This leads to increase in error with increasing r, yet the technique provides a reliable speed for the body of the current within the region $60 < r < 150$ cm for our experiments.

Using vertical profiles of time averaged velocity and concentration shown in figure 3.10, we estimated gradient Richardson number, Ri_g, at different radial locations within the tail region:

$$Ri_g(r, z) = \frac{\mathrm{d}\langle g' \rangle / \mathrm{d}z}{-\left(\mathrm{d}\langle u \rangle / \mathrm{d}z\right)^2}, \tag{3.9}$$

where $\mathrm{d}\langle g'\rangle/\mathrm{d}z$ and $\mathrm{d}\langle u\rangle/\mathrm{d}z$ are determined using averaged gradients in the region $0.1h_r < z < 0.9h_r$. The estimated Ri_g is always higher than critical Richardson number, $Ri_{\mathrm{crit}} = 0.25$, below which the flows are expected to be unstable (Miles, 1961). This suggests that mixing within this steady tail region is small. However, a thin region with significant velocity shear may exist at the top region as shown in the extrapolation in the region $z > 0.9h_r$. Ri_g associated to the region $z > 0.9h_r$ is also calculated and appears to be slightly lower than 0.25 within this region which would suggest potential mixing along the thin layer at the top boundary of the currents, but possibly not throughout the whole depth of the currents. Nonetheless, a different assumption for the velocity profiles will result in a larger Ri_g which suggests that the flow is rather stable even at the interface.

3.6.2 Entrainment in the body region

Considering the steady tail region, the total radial volume flux is the integral of radial speed across the depth

$$Q_r = \int_0^{h_r} ru\mathrm{d}z = ru_r h_r, \tag{3.10}$$

where u_r is the vertical averaged radial speed. Using the velocity profiles determined by the method described in §3.6.1, radial flux of the current is seen to increase with radius as shown in figure 3.11a. By this method, the volume flux determined at $r =$ 60 cm is found to be within 15% error of the effective source flux defined at this same radius, Q_o, (section §3.4.1) for most experiments. We found that the estimated volume flux appears to increase for all experiments and can reach a factor of ∼1.2-1.8 of Q_o by $r = 150$ cm. We note here that the anomalously high value Q_r at $100 < r < 120$ cm is resulted from the error in estimated velocity in the wake region of the flow. Figure 3.11b shows the time-averaged depth of the current in the tail which is approximately constant behind the head except for experiment F whose depth slightly increase with radius until ∼100 cm.

Figure 3.11c shows the approximated depth-averaged speed, $u_r = Q_r/(rh_r)$, calculated for each experiment. Although the large error associated with estimated Q_r appears to lead to relatively large fluctuation in the estimated u_r, all experiments show a general gradually decreasing trend for u_r with increasing r, from $u_r \approx 10 \pm 2$ cm s^{-1} at $r = 60$ cm to $u_r \approx 8 \pm 3$ cm s^{-1} at $r = 150$ cm.

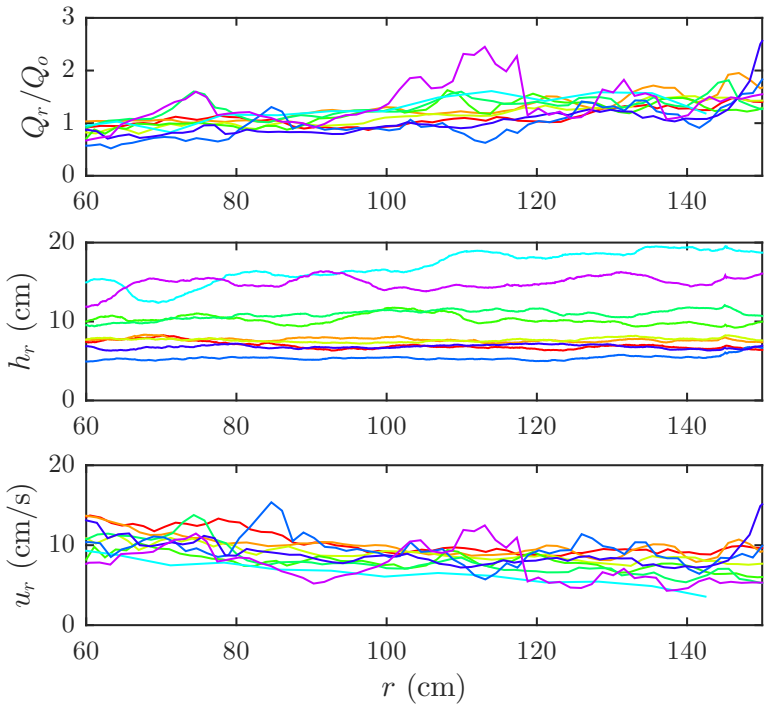

Fig. 3.11 Plots show the properties within the tail of experimental gravity currents. (a) The radial fluxes are calculated from the velocity profiles and normalised by the corresponding effective source fluxes defined at r =60 cm. The general trend shows an increasing source flux with radius which can reach a value of 1.2-1.8 of Q_o at $r = 150$ cm. (b) The time-averaged depths show that the depth of each current is approximately constant in the tail region. (c) The depth-averaged velocities, $\bar{u}_r$, calculated from $Q_r = ru_rh_r$ show a generally decreasing trend with radius for each experiment. Colours represent results from different experiments as coded in table 3.1.

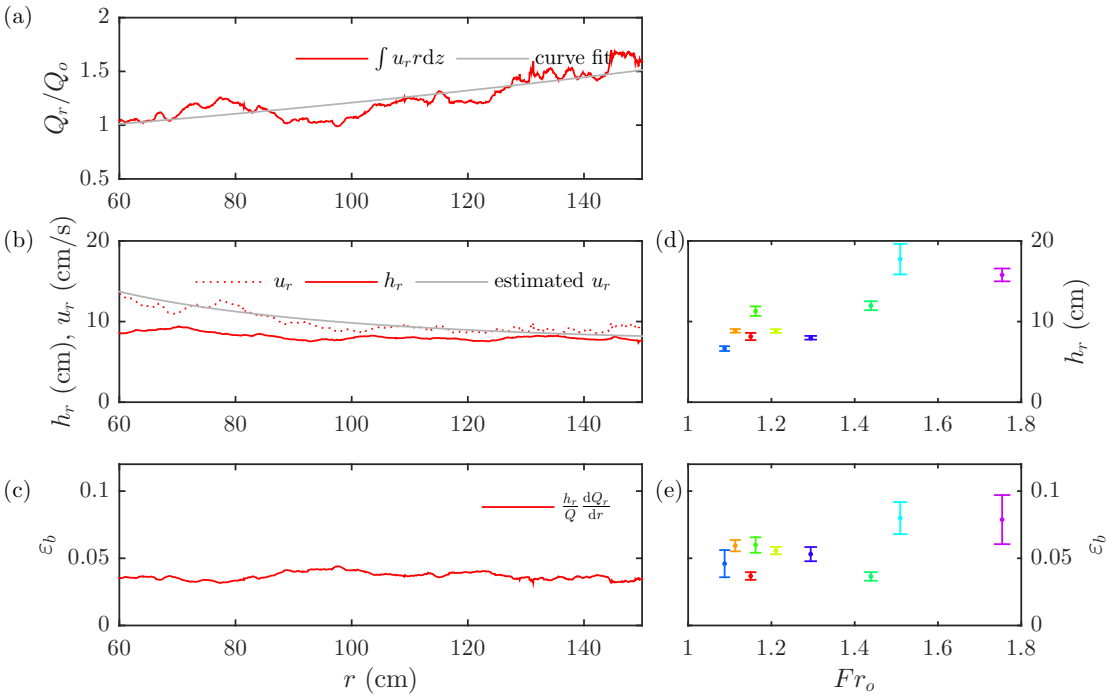

Fig. 3.12 (a-c) Plots from experiment A showing measured time-averaged properties within the tail region of (a) the normalised volume flux at different radii, $\int ru\mathrm{d}z/Q_o$, and the curve fit associated with it; (b) h_r and u_r together with the estimated u_r determined from the curve fit of Q_r shown in (a), using $Q_r = ru_rh_r$; and (c) the approximation of the mixing coefficient along the back of the current, $\varepsilon_b = (h_r/Q_r)\,(\mathrm{d}Q_r/\mathrm{d}r)$, where $\mathrm{d}Q_r/\mathrm{d}r$ is determined from the curve fit of Q_r. The radial-averaged values, within the range $60 < r < 150$ cm, of h_r and ε_b from different experiments are shown as a function of Fr_o in (d) and (e), respectively. The error bars show standard deviations and the different experiments are plotted in different colours as coded in table 3.1.

The increase in radial volume flux reflects the result of mixing within this steady tail region. If we assume the entrainment velocity is proportional to the mean radial speed of the flow, the change of volume flux with radius can be written as

$$\frac{\mathrm{d}Q_r}{\mathrm{d}r} = \varepsilon_b u_r r \tag{3.11}$$

where ε_b is the entrainment coefficient along the back of the current within the tail region. The expression for ε_b can be rewritten as

$$\varepsilon_b = \frac{h_r}{Q_r}\frac{\mathrm{d}Q_r}{\mathrm{d}r}, \tag{3.12}$$

by combining (3.10) and (3.11). In order to estimate the value for $\mathrm{d}Q_r/\mathrm{d}r$, a curve fit, whose derivative can be calculated, is determined for each experiment. The curve fit is shown as dashed yellow line in figure 3.12a for the experiment A compared to the data (blue) as an example.

Figure 3.12c shows the estimated $\varepsilon_b(r)$ using the data for Q_r, time-averaged height and $\mathrm{d}Q_r/\mathrm{d}r$ determined from the curve fit in figure 3.12a. ε_b is found to be approximately constant within the region $60 < r < 150$ cm. The radial average value of ε_b is found to grow, from approximately 0.03 to 0.09, with increasing Fr_o as shown in figure 3.12e.

3.6.3 Entrainment in the front region

Using the height profile determined from each photograph, we determine an instantaneous volume of the current,

$$V(t) = \int_0^{r_n} rh(r,t)\mathrm{d}r. \tag{3.13}$$

Normalising volume by L^3 and time by T shows a reasonable collapse for all the data (figure 3.13a). The instantaneous rate of volume change, $\mathrm{d}V/\mathrm{d}t$, can be determined from the volume change at successive times. Figure 3.13b shows $\mathrm{d}\hat{V}/\mathrm{d}\hat{t}$ as determined from the experimental data as a function of $\hat{t}$. This is found to scatter around a linear trend shown by a black line for all experiments. Note that in dimensional form, $\mathrm{d}\hat{V}/\mathrm{d}\hat{t} = (\mathrm{d}V/\mathrm{d}t)/Q_o$.

Considering the mixing mechanisms, the volume change of the currents comprises three parts: the source flux, the ambient fluid entrained along the top boundary of

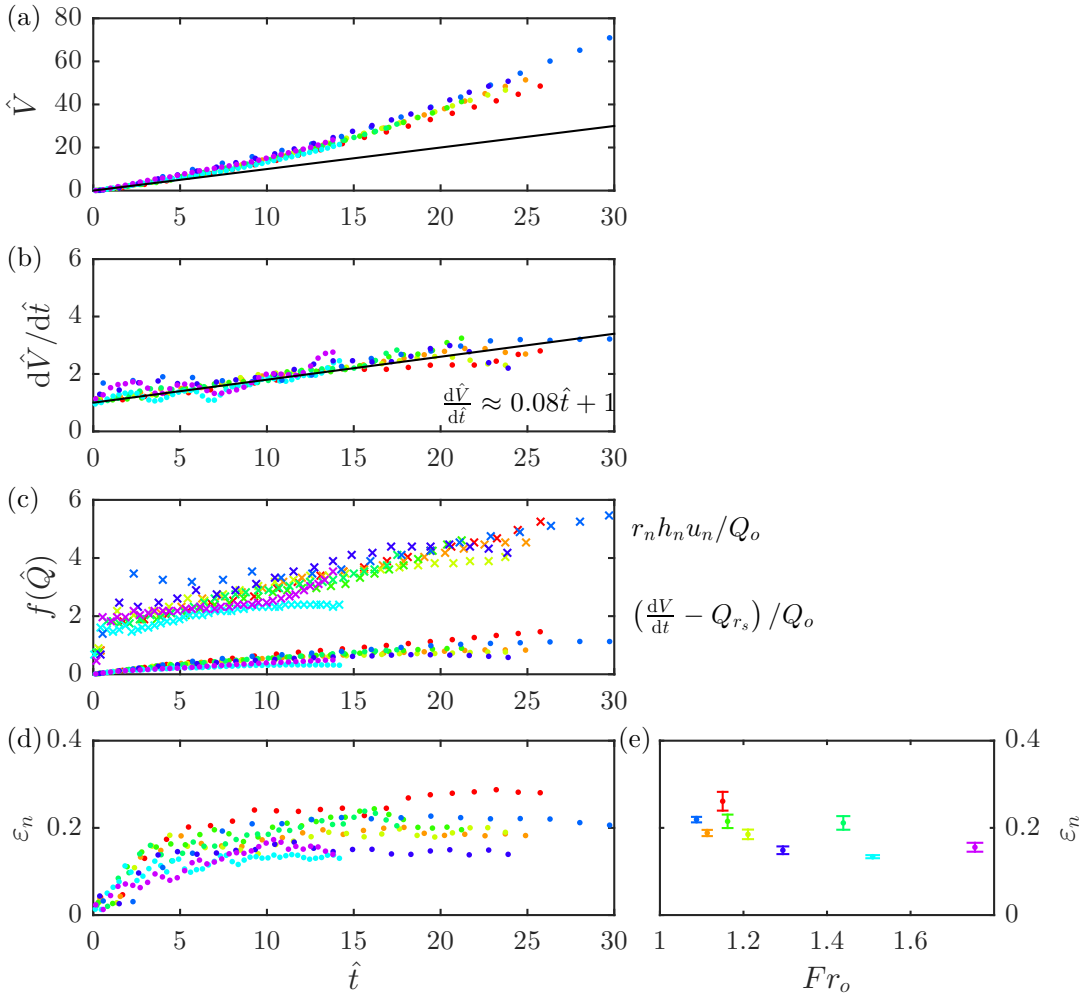

Fig. 3.13 (a) A plot of normalised volume with normalised time shows that the chosen length and time scales can successfully collapse the experimental data. The black line shows the source volume of the current based on the supply rate, Q_o. (b) A plot of volume change in time based on the data. The linear best fit (black line) is chosen to describe the general trend for experimental volume change. (c) The estimated volume fluxes associated with different parts of the currents. The crosses ($\times$) show the approximated volume fluxes being displaced by the advancing fronts, $r_n h_n u_n$ while the dots ($\cdot$) show the estimate volume fluxes being supplied behind the heads at $r_s(t)$. (d) The mixing coefficient near the front, $\varepsilon_n = 0.20 \pm 0.04$, is estimated from the volume change of the data. The mixing coefficients converge to a constant for each experiment but slightly vary from one experiment to another. (e) The time-averaged ε_n for $\hat{t} > 10$ from different experiments are plotted as a function of Fr_o. Colours represent results from different experiments as coded in table 3.1.

the flow and the ambient fluid entrained due to circulation near the front. The rate of change in current volume can then be written as

$$\frac{\mathrm{d}V}{\mathrm{d}t} = Q_o + \int_{r_o}^{r_s} \tilde{\varepsilon_b} u_r r \mathrm{d}r + \varepsilon_n Q_n \tag{3.14}$$

where ε_n is the fraction of ambient fluid ahead of the nose, denoted by volume flux Q_n, that can entrain into the current. $\tilde{\varepsilon_b} u_r r$ is the local entrainment velocity of ambient fluid along the current-ambient boundary arising from the shear instability at r with the vertical averaged radial flow velocity u_r, which will be integrated from r_o to r_s, the location of the back of the head (figure 3.6). The first term represents the constant volumetric flux feeding the current following the adjustment at the inflow.

Provided that the location of the rear of the head, r_s, is known, the second term of (3.14) can be simplified to $Q_{r_s} - Q_o$. However, it is difficult to determine r_s based on the apparent depth due to the time-dependent billow structure shredding from the rear of the head into the wake region. Instead, we assume that the head region maintains a certain proportion of instantaneous total volume at all time. Assuming 65% of total volume is located within the head region, the boundary seems to bisect the downstream advancing eddies region from the region of billow shredding behind the head as seen in figure 3.3(b,c). As a result, this criterion is used to determine r_s.

The volume flux of fluid being displaced by the advancing front can be estimated according to (see §2.4.2; cf. Sher & Woods, 2015),

$$Q_n = r_n h_n u_n, \tag{3.15}$$

and is shown in crosses in figure 3.13c based on our experimental data for u_n (figure 3.8a), r_n (figure 3.7f) and h_n (defined as the maximum depth within the front region). Using this definition for volume flux displaced by the head and the volume flux supply from the body region to the head, (3.14) can be written as

$$\frac{\mathrm{d}V}{\mathrm{d}t} = Q_{r_s} + \varepsilon_n r_n h_n u_n. \tag{3.16}$$

Using Q_{r_s} determined from the curve fit of Q_r for each experiment (figure 3.12a), dots in figure 3.13c shows the estimated volume supply rate in the head by the fluid in the body region, $\mathrm{d}V/\mathrm{d}t - Q_{r_s}$. The mixing coefficient within the front region can then be calculated (figure 3.13d). Our data show that, ε_b, increases with $\hat{t}$ but starts to level off to a constant value after $\hat{t} \approx 10$ for each experiment. It seems that the initial

growth of the current at the early time is mainly described by the effective source flux, Q_o, as seen in figure 3.13 when comparing the volume of the detected volume to that of the supplied volume. Figure 3.13e shows the time-averaged ε_n after $\hat{t} > 10$ as a function of Fr_o and is found to decreases from 0.27 ± 0.02 to 0.13 ± 0.01 with increasing Fr_o (from 1.11 to 1.75).

3.7 Comparison with theoretical models

3.7.1 Mathematical considerations

Slim & Huppert (2011) developed a model for the evolution of an axisymmetric gravity current, comprising a steady tail region connected with a head region that can be solved using a similarity solution. Subsequently, Johnson *et al.* (2015) showed that the similarity solution within the head region does not fully explain the evolution of the currents and refined the model by including the next leading order terms; however, the mixing of ambient fluid into the head was neglected. In this section, we follow the mathematical considerations used in their models which will then be compared to our experimental results in the followeing section. The mathematical parameters are non-dimensionalised using the length and time scales, $L = (Q_o^3/B_o)^{1/5}$ and $T = (Q_o^4/B_o^3)^{1/5}$, respectively, although the hat symbols ($\hat{\cdot}$) associated with the non-dimensionalised parameters are omitted in this section.

Assuming the entrainment of the ambient fluid to be negligible, the mass and momentum conservation equations for axisymmetric gravity currents are in the form

$$\frac{\partial h}{\partial t} + \frac{1}{r}\frac{\partial}{\partial r}(r u_r h) = 0, \tag{3.17}$$

$$\frac{\partial}{\partial t}(hu) + \frac{1}{r}\frac{\partial}{\partial r}\left(r u_r^2 h\right) + \frac{\partial}{\partial r}\left(\frac{h^2}{2}\right) = 0, \tag{3.18}$$

with the boundary condition

$$u_r = Fr_n\sqrt{h}, \quad \text{at} \quad r = r_n(t). \tag{3.19}$$

Based on the numerical solution, Johnson *et al.* (2015) argued that the solution is not in a similarity form, but rather consists of a region of steady inner tail connected, through a discontinuity, to a frontal region that evolves with time. Using this argument,

the two conservation equations at the steady tail region will become

$$\frac{\mathrm{d}}{\mathrm{d}r}(ru_r h) = 0, \tag{3.20}$$

$$\frac{\mathrm{d}}{\mathrm{d}r}\left(\frac{u_r^2}{2} + h\right) = 0, \tag{3.21}$$

with the knowledge of the source conditions

$$ru_r h = 1 \quad \text{and} \quad \frac{u_r^2}{2} + h = \tilde{E} \quad \text{at} \quad r = r_o \tag{3.22}$$

where r_o is the source radius. These source conditions represent the constant mass flux and the energy density (Bernoulli constant), respectively. Writing u_r in terms of the source Froude number, $u_r = F_o\sqrt{h}$ at $r = r_o$, they obtained an expression for the Bernoulli constant as

$$\tilde{E} = \frac{Fr_o^{-2/3} + (1/2)Fr_o^{4/3}}{r_o^{2/3}}. \tag{3.23}$$

Accordingly, they derived the solutions for the u_r and h at $r \gg r_o$ which can be written in the form

$$u_r(r) = (2\tilde{E})^{1/2} + ..., \quad \text{and} \quad h(r) = \frac{(2\tilde{E})^{-1/2}}{r} + ..., \tag{3.24}$$

Johnson *et al.* (2015) showed that the solution involves a steady tail region which merges into a moving head. They modelled the transition into the head as a shock front, and that the head extended ahead of this transition by a finite distance to the front of the flow (figure 3.14). Using the two conservation equations across the discontinuity at $r = r_s(t)$, which is moving with a speed u_{r_s}, the two equations can then be written as

$$[(u_r - u_{r_s})h]_{r_s^-}^{r_s^+} = 0, \tag{3.25}$$

$$\left[u_r(u_r - u_{r_s})h + \frac{h^2}{2}\right]_{r_s^-}^{r_s^+} = 0. \tag{3.26}$$

Considering the largest term in the equations, they anticipated that r_n and r_s grow as $t^{4/5}$. However, by including the next largest term that was omitted in Slim & Huppert (2011)'s formulation, they showed that this term will be different from the leading

term by $O(t^{-1/5})$. By this argument, they derived expressions for the positions of the front, the shock, the radial velocity and the height at $r_s < r < r_n$ in the form

$$r_n(t) = r_{no}t^{4/5} + r_{n1}t^{3/5} + ..., \tag{3.27}$$

$$r_s(t) = r_{so}t^{4/5} + r_{s1}t^{3/5} + ..., \tag{3.28}$$

$$u_r(r,t) = r_{no}\mathcal{U}_o(\eta)t^{-1/5} + r_{n1}\mathcal{U}_1(\eta)t^{-2/5} + ..., \tag{3.29}$$

$$h(r,t) = r_{no}^2\mathcal{H}_o(\eta)t^{-2/5} + r_{n1}r_{no}\mathcal{H}_1(\eta)t^{-3/5} + ..., \tag{3.30}$$

where r_{no}, r_{n1}, r_{so} and r_{s1} are constants to be determined and $\eta = r/r_n$. By considering only the leading-order terms, the mass and momentum conservation equations (3.18) can then be written as

$$-\frac{2}{5}\eta\mathcal{H}_o - \frac{4}{5}\eta^2\mathcal{H}_o' + (\eta\mathcal{U}_o\mathcal{H}_o)' = 0, \tag{3.31}$$

$$-\frac{1}{5}\mathcal{U}_o - \frac{4}{5}\eta\mathcal{U}_o' + \mathcal{U}_o\mathcal{U}_o' + \mathcal{H}_o' = 0, \tag{3.32}$$

where the primes denote differentiation with respect to η. Differentiating (3.27) and applying the boundary condition, $u(r_n) = Fr_n\sqrt{h_n}$, they showed – by first considering only the leading-order terms and then including the next leading-order terms – that

$$\mathcal{U}_o(1) = \frac{4}{5}, \quad \mathcal{H}_o(1) = \frac{16}{25Fr_n^2}, \quad \mathcal{U}_1(1) = \frac{3}{5} \quad \text{and} \quad \mathcal{H}_1(1) = \frac{24}{25Fr_n^2}. \tag{3.33}$$

The speed of the shock, u_{r_s}, can be determined by differentiating (3.28). Using this result and considering the leading-order expressions for condition of the shock, (3.25, 3.26), $\mathcal{U}_o(\eta_s)$ and $\mathcal{H}_o(\eta_s)$ can be written as

$$\mathcal{U}_o(\eta_s) = \frac{4}{5}\eta_s \quad \text{and} \quad \mathcal{H}_o(\eta_s)^2 = \frac{2(2\tilde{E})^{1/2}}{r_{no}^5\eta_s}, \tag{3.34}$$

where $\eta_s = r_s/r_n = r_{so}/r_{no}$. By integrating (3.31) from $\eta = \eta_s$ to 1 using the values for $\mathcal{H}_o$ and $\mathcal{U}_o$ evaluated at $\eta = 1$ and η_s (3.33, 3.34), it can be deduced that

$$\frac{6}{5}\int_{\eta_s}^{1}\eta\mathcal{H}_o\mathrm{d}\eta = \left[\frac{4}{5}\eta^2\mathcal{H}_o - \eta\mathcal{U}_o\mathcal{H}_o\right]_{\eta_s}^{1} = 0, \tag{3.35}$$

which will be true only if $r_{no} = r_{so}$ since $\mathcal{H}_o > 0$. From (3.34), it can be shown that

$$r_{no}^5 = r_{so}^5 = \frac{5^4 Fr_n^4 \tilde{E}^{1/2}}{2^{13/2}}. \tag{3.36}$$

In order to determine the values for r_{n1} and r_{s1}, Johnson *et al.* (2015) evaluated the shock condition to the next order and showed that

$$r_{n1} = \frac{2 - 9Fr_n^2}{8r_{no}^3 \mathcal{H}_o(1)} \quad \text{and} \quad r_{s1} = \frac{-6 - 9Fr_n^2}{8r_{no}^3 \mathcal{H}_o(1)}. \tag{3.37}$$

The ODEs system for conservations of mass (3.31) and momentum (3.32) can then be solved numerically using the boundary values at the front (3.33), to find u_r and h at any r within the head region.

3.7.2 Comparison with the experimental data

Johnson *et al.* (2015)'s model requires the knowledge of the front Froude number, Fr_n, source Froude number, Fr_o, and the source radius, r_o. Here we use the front Froude number determined from the experimental time-averaged Fr_n at $\hat{t} > 5$ and assume the source radius is $\hat{r}_o = 60$ cm/L. Figure 3.14 shows the predicted height profiles for experiment C at different times calculated from (3.24) and (3.30) together with the experimental data for h, $\int g' \mathrm{d}z$ and the vertical profiles of g' in the tail region for comparison. These experimental data are normalised by L, $\overline{g'_o}L$ and $\overline{g'_o}$, respectively.

When applying this to the rest of our experiments, it was found that the model underestimated the front position and the height profile. This might be because the model does not account for the mixing between currents and the ambient fluid. We found that including $t_o = 3.5$ s to account for the virtual time origin, t_o, (cf. §2.4.3) can improve the mismatch between the observable front positions and the predicted $\hat{r}_n$. Yet, this does not seem to improve the mismatch between the predicted shock positions, $\hat{r}_s$, to the observable rears of the head. Considering the experimental $\int \hat{g}' \mathrm{d}\hat{z}$ profiles, which is equivalent to the profile should no mixing occur, the predicted height was higher than $\int \hat{g}' \mathrm{d}\hat{z}$ in the head region but lower in the tail region. Yet, the predicted height at the front, $\hat{h}(\hat{r}_n)$, appears to be comparable to our experimental data for $(\overline{g'}h)_n/\overline{g'_o}L$.

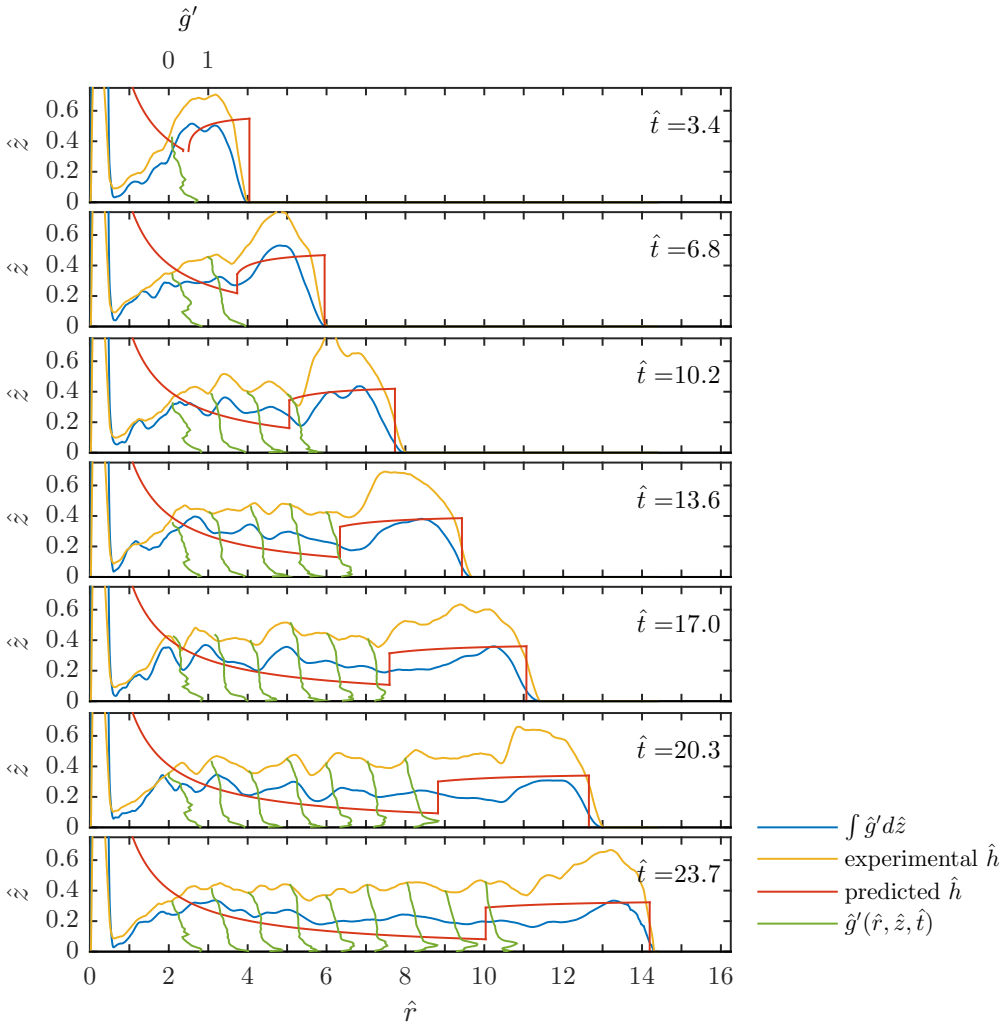

Fig. 3.14 The experimental data for the height and vertical integral buoyancy profiles from experiment C at different time. The predicted height profiles, following Johnson *et al.* (2015)'s model, calculated from associated Fr_o and $\langle Fr_n \rangle$ for this experiment (table 3.1) are shown for comparison. We also plotted the vertical profiles of $\hat{g}'$ at $\hat{r} = 2, 3, 4, ... < \hat{r}_s$. The profiles are scaled such that they are 0 at their corresponding positions and are 1 at the positions of the next adjacent profiles.

3.8 Discussion and conclusion

We have described a new series of experiments of the front speed, the depth and evolving buoyancy throughout an axisymmetric gravity current. Here the mixing coefficient within the head, ε_b, is defined as the fraction of the ambient fluid being displaced by the front propagation that can entrain into the current. We found that for a gravity current with an effective source Froude number, Fr_o, within a range 1.0 - 2.0, ε_b is approximately 0.20 ± 0.04 and shows a small decreasing trend with increasing Fr_o. This is comparable to the mixing coefficient of 0.15 to 0.30 determined for a two-dimensional gravity current with decreasing source Fr from 2.0 to 1.0 (Sher & Woods, 2017) though our results show less dependency on Fr_o.

For gravity currents generated by continuous supply of dense fluid, we found that currents develop a strong velocity and buoyancy shear, with the fluid at the base of the flow catching up with the head of the current, displacing ambient fluid and mixing, to form a more dilute zone at the top of the flow which advances more slowly than the head. The source fluid forms a dense bottom layer which eventually reaches the front. Subsequently, it rolls up, mixes with the ambient fluid and recirculates. Measurements of the velocity and buoyancy in the tail region of the flow suggest that the gradient Richardson number is an order 1-10, in excess of 0.25 across the tail region of the flow. Though, the radial volume flux determined from velocity profile suggests there is some entrainment of ambient fluid along the upper surface of the tail region with an entrainment coefficient within a range 0.03-0.09, the entrained fluid may not be able to penetrate through the whole depth of the current. This is illustrated by the dye experiments which shows that if mixing occurs, it only occurs in the upper part of the flow. The dense bottom flow feeding the head of the current is not mixed by the fluid above it due to the stable buoyancy stratification as reflected by the large value of Ri_g.

Our experiments suggest the nose of the current advances as $r_n \sim t^{3/4}$. The experimental data were compared to Johnson *et al.* (2015)'s models. Though the mixing is ignored, it can sufficiently estimate the frontal position yet does not give an accurate detailed for the height profiles of the currents.

Chapter 4

Thermodynamics of a lava lake

4.1 Abstract

We explore the heat transfer within a volcanic conduit under the influence of separated gas-liquid flow. We develop a series of analogue laboratory experiments in which we measure the mixing produced by the wakes of the bubbles as they move along the tube. To measure the mixing we release a pulse of dye in the liquid at the base of the tube and measure how it spreads along the tube as a continuous stream of bubbles pass by. The dye is dispersed along the tube with an effective diffusivity which depends on the gas flux and the speed of the bubbles. By carrying out a systematic series of experiments, we find that the dispersivity has the form, $D = 1.25 d_c u_g^{1/2} u_o^{3/2} (u_g + u_o)^{-1}$ where u_g is the superficial gas speed and u_o is the single bubble speed depending on conduit diameter, d_c. The dispersivity is independent of the liquid viscosity within the range 0.1 to 0.01 $\mathrm{cm^2 s^{-1}}$, for which the Reynolds number of the bubbles based on liquid viscosity and conduit diameter is in excess of 2000. We then argue that by analogy heat is transferred by slugs rising along a volcanic conduit. We develop a mathematical model using the experimentally determined dispersivity and we predict the heat flux along a volcanic conduit. The heat flux is comparable to the total heat loss by radiation and convection from the surface of several lava lakes which have been measured and reported in the literature.

4.2 Introduction

Active lava lakes are large molten bodies of lava confined within a volcanic crater and are believed to represent the exposed tops of magma plumbing systems, linked to

subsurface magma chambers via a volcanic conduit. Lava lakes involve active degassing with the gas flux varying by several orders of magnitude from volcano to volcano, with the gas flux being a few kg s^{-1} at Erta 'Ale volcano (Le Guern *et al.*, 1979; Sawyer *et al.*, 2008) to a few thousands kg s^{-1} at Ambrym volcano (Allard *et al.*, 2016).

Without a continuous heat flux supplied to the lava, we would expect lava lakes to cool and solidify. However, many lava lakes have proven to persist over decades indicating that a large heat flux is supplied from the magma plumbing system below the volcano. Magma convection in the conduit driven by the density differences between the hot magma at depth and the warm lava in the lake has been proposed as the main mechanism that replenishes the heat in the lava lake (Francis *et al.*, 1993; Huppert & Hallworth, 2007; Stevenson & Blake, 1998). Replenishing lava from depth also provides fresh and undegassed magma that maintains the persisting degassing behaviour observed at lava lakes. However, acoustic studies show large bubbles burst at the lake surface and that these large bubbles are over-pressurised suggesting a deep origin (Bouche *et al.*, 2010; Johnson *et al.*, 2008). Bouche *et al.* (2010) proposed that heat may be supplied to the lava lake by these bubbles if they originate at the base of the conduit and commented that the presence of large scale bubbles within the conduit would disturb the magma convection. However, there were no calculations or modelling of these hypotheses.

Conduit convection has been studied experimentally using viscous liquid (Beckett *et al.*, 2011; Huppert & Hallworth, 2007; Stevenson & Blake, 1998). However, with low to intermediate viscosity liquid, the flow within the conduit tends to mix and the simple convective cells of very long vertical extent are no longer observed. Although the experiments have shown and quantified conduit convection can occur within a volcanic conduit, they assume that gas and liquid flow together with no bubble slip relative to the liquid. On the other hand, as the bubbles increase in size, the slip velocity increases. However, many experiments on liquid-gas separated flows within a vertical conduit tend to focus on predicting bubble dynamics, void fraction and pressure drop due to vesicularity within the conduit (Pioli *et al.*, 2012; Seyfried & Freundt, 2000).

The aim of this study is to explore the role of large bubbles rising through the conduit in transferring heat from the base to the top of the conduit. We use a light attenuation technique to quantify the speed at which dye - injected at the base of the conduit - rises along the conduit, even with no net flow of liquid in the conduit. We argue that the dispersive mixing of the dye by the bubbles is analogous to the

dispersive mixing of heat along a conduit subject to a continuous stream of bubbles and we show that this can lead to a net heat flux even with zero net flow.

4.3 Experimental Method

Experiments were conducted in a vertical cylindrical conduit of an internal diameter of 3.7 cm and 3.5 m long. A section of the pipe 3.1 m long was back-lit by an LED light panel (W&Co Displays and Signs). A continuous supply of air was provided by peristaltic pump through an inlet attached at one side of the conduit wall 20 cm below the viewing area. The system allows air flow in the range 1.6 to 64.9 $cm^3\ s^{-1}$. A few experiments were conducted using a compressed air line which allows a larger flow up to 107.8 $cm^3\ s^{-1}$. The conduit is filled with either water or aqueous glycerol solution to vary the kinematic viscosity, ν, within the range 0.01 to 0.1 $cm^2\ s^{-1}$. The density of the glycerol solution was measured for each experiment using a pycnometer. The viscosity of the solution is calculated from its density and temperature before each experiment using a formula proposed by Takamura *et al.* (2012) except for the experiments with water whose viscosity was taken to be 0.01 $cm^2\ s^{-1}$.

For the light attenuation experiments, video clips were taken with a Nikon D5300 RGB DSLR camera located $\approx$ 3 m from the conduit. Two-phase flow was initiated by pumping in air to the stagnant column of colourless liquid of known viscosity. The experiment persisted for at least 30 s to ensure the equilibrium was reached; at this point, 20 mL dye solution of known concentration was injected at the bottom of the conduit through a small hole opposite but slightly above the gas inlet. The video frames were processed and analysed using a Matlab script to determine cross-sectional averaged concentration using a calibration curve obtained by measuring the light attenuation of the conduit when 20 different known dye concentrations were added to the liquid.

4.4 Results

4.4.1 Qualitative descriptions for mixing in the wake

The bubble size and shape are found to depend largely on gas flux. At low flow rates, we observe bubbles rising in the form of clusters of 3-5 bubbles each. With greater gas fluxes, bubbles in each cluster are observed to be larger and eventually merge into one

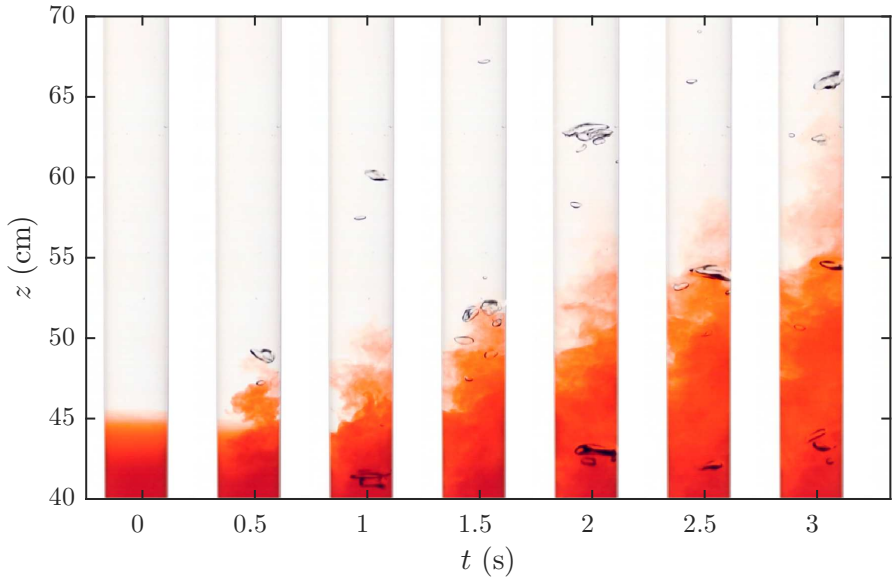

Fig. 4.1 Photos of dye mixing due to gas flows in a vertical tube. Dye originally located at the bottom of the tube is gradually mixed and transported upwards under the influence of bubbles rising within the conduit.

conduit-size bubble with a spherical cap shape, rising in a slug flow regime. As the gas flux further increases, the size of the bubbles became expectedly bigger, but the confinement due to the conduit wall forces the bubble to elongate along the direction of the stream, leading to bubbles which resemble Taylor bubbles.

As a bubble rises, it displaces liquid ahead of it. The displaced liquid falls down around the bubble, forming a downflow region between the bubble and the conduit wall. A wake region is subsequently formed in the liquid behind the bubble where mixing between the liquid originally ahead of the bubble and the liquid behind the bubble occurs. In general, the wake can be laminar (closed and symmetric) or turbulent (open wake with an irregular and time-dependent wake boundary). The wake dynamics for single slugs was proposed to depend on Re_B (1.43) with a laminar wake forming when $Re_B < 500$ and a turbulent wake forming when $Re_B > 1500$ (Campos & Carvalho, 1988). Nevertheless, within the range of liquid viscosities used in our experiments, $Re_B > 2000$, turbulent wakes have always been observed. The recirculation of fluid through the turbulent wake leads to gradual mixing of dyed liquid along the conduit (Fig 4.1).

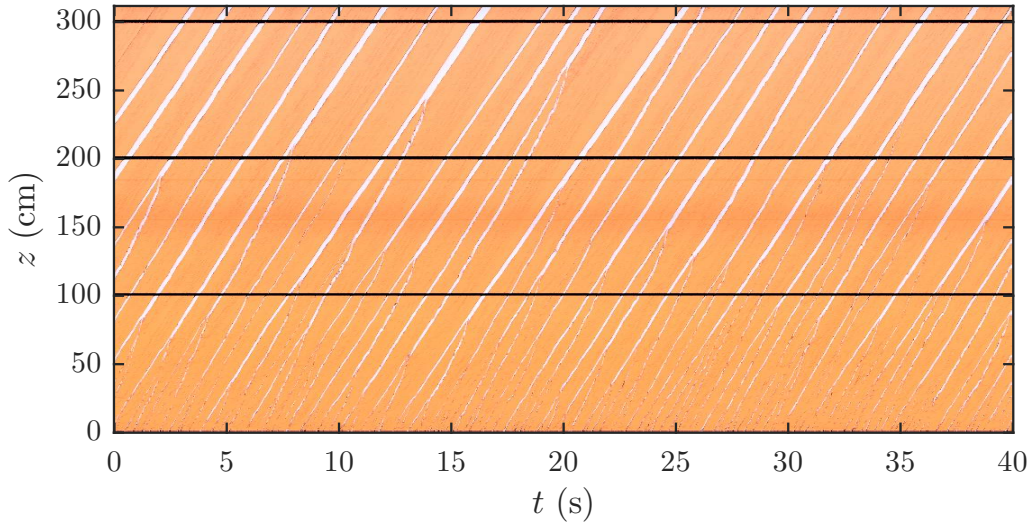

Fig. 4.2 Time series for gas slugs rising in a vertical conduit. The liquid phase was primarily mixed with red dye resulting from the conduit mixing by the bubble flow. The speed at which the bubbles rise can be determined from the gradient of bubbles in the plot which can be seen to be similar for each bubble. The speed is approximately constant except just before bubble coalescence, where the bubble is seen to accelerate (steeper slope) to catch up with the preceding bubble.

4.4.2 Bubble characteristics

The bubble speed, length and frequency (u_b, L_b and ω, respectively) can be determined from a time series of cross-sectional averaged images for each experiment. Since air and undyed liquid appear indistinguishable in the images, only data at a late stage after the dye has been fully mixed throughout the conduit can be used to determine bubble characteristics as the liquid and gas at this stage are clearly distinguishable. Figure 4.2 shows an example of the data for the bubble characteristic analysis. Bubble speed can be measured from the slope of the bubble top which appears to be linear except shortly before bubble coalescence when the following bubble accelerates and merges with the preceding bubble to form a larger gas slug. Bubble coalescence occurs frequently at $z < 100$ cm but can also be observed, though much less frequently, even towards the top end of the conduit.

Bubble length (or slug length), L_b, can be measured by the time it takes for the bubble to pass through the chosen height multiplied by the averaged bubble speed. It was found to become less dependent with height at $z > 100$ cm since the coalescence is less pronounced beyond this height. Here the reported L_b is measured at $z = 290$ cm. Bubble frequency, ω, is measured by the number of bubbles passing by this same level

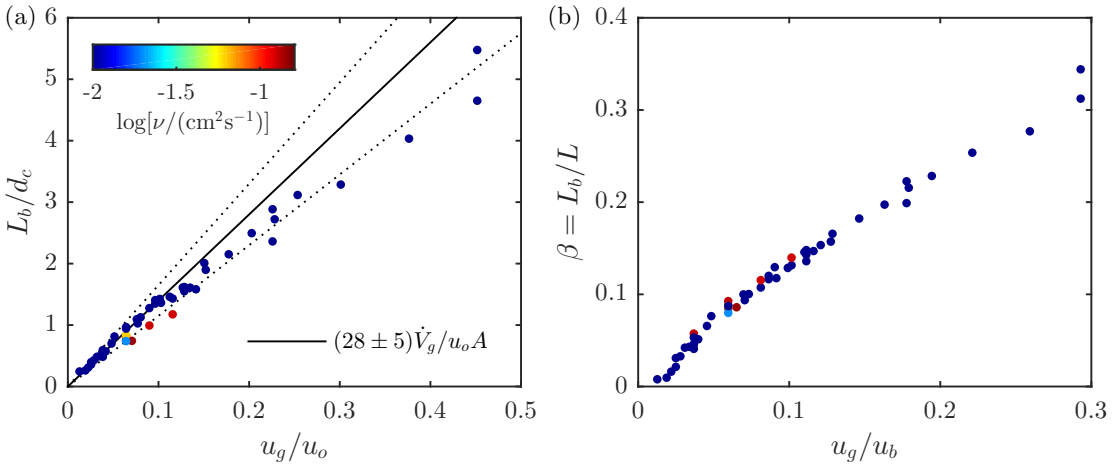

Fig. 4.3 Plots for bubble length, L_b, and bubble fraction, L_b/L, as a function of superficial gas speed, u_g. Gas flux is normalised by u_bA which is found to collapse all the data from inviscid experiments ($\nu < 0.1$ cm^2 s^{-1}). The results from different liquid viscosities are plotted in different colours.

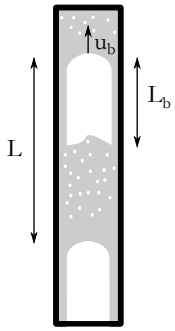

Fig. 4.4 Schematic diagram showing some nomenclature used to described a slug unit.

within a certain period of time. Figure 4.3a is a plot for bubble length as a function of superficial gas speed as determined by the gas flux:

$$u_g = \frac{\dot{V}_g}{A}. \tag{4.1}$$

The slug length, L_b, is found to increase from $0.25d_c$ to $5.5d_c$ with increasing superficial gas speed from 0.15 to 10.03 cm s^{-1} (corresponding to the gas flux from 1.6 to 107.8 cm^3 s^{-1}). In the figure, slug length is normalised by the conduit diameter and the superficial gas speed is normalised by the theoretical speed of a single gas slug, $u_o = 0.35(g'd_c)^{1/2}$. We found from the experiment that L_b follows the approximate

relationship as

$$\frac{L_b}{d_c} \approx 28\frac{u_g}{u_o} \tag{4.2}$$

Our results show that the dependency of L_b on liquid viscosity is small compared to the dependency on superficial gas velocity. We note, however, that at large superficial gas speed (hence large gas flux) the experimental slug length deviates from this approximation. This could be because the fully developed continuous slug flow, in which there is no interaction between consecutive gas slugs, has not yet been achieved even at this height especially for a flow with large u_g. The interaction between gas slugs leads to acceleration of the following slug towards the preceding slug and results in the coalescence of the two which can be observed more frequently in our experiments with large u_g. Without the interaction between gas slugs, each slug will rise independently and the coalescence between adjacent slugs is expected to be absent. (Pinto & Campos, 1996; Taitel *et al.*, 1980). Mayor *et al.* (2008) suggested that the fully developed continuous flow will be achieved at a height of at least $70d_c$ above the inflow. We note that this would be equivalent to ~ 280 cm for the conduit diameter used in our experiments, just about the height at which we made the measurement.

Here we consider a bubble fraction, L_b/L, where L is the sum of the bubble length and the length of liquid bridge connecting two consecutive gas slugs. In many studies, L is also known as a slug unit length as it represents the length of a complete unit comprising of a gas slug and liquid phase behind it. Theoretically this is less dependent on bubble coalescence, as combining two identical slug units would increase bubble length and the slug unit length by the same factor while the fraction between the two is unchanged. If we assume that the gas volume (void) fraction within the liquid phase in between two consecutive gas slugs is small, for slug flow with the bubble length, L_b, and bubble frequency, ω, the gas flux can be related to the bubble length and frequency in the form

$$\dot{V}_g = \omega A L_b. \tag{4.3}$$

As the bubble frequency passing a particular height can be related to the bubble velocity by $\omega = u_b/L$, the gas flux can then be written as

$$\dot{V}_g = u_b A \beta \quad ; \tag{4.4}$$

$$u_g = u_b \beta. \tag{4.5}$$

The plot of bubble fraction, $\beta = L_b/L$, as a function of u_g/u_b (figure 4.3b) shows a slight offset from equation (4.5). However, it is still within the variation of bubble length which is found to be as high as 0.1. Also, small slugs can be undetected in the analysis which can cause the slight overestimate for the reported β.

4.4.3 A modelling approach for mixing process

The plot of dye concentration in a $z^2 - t$ domain (figure 4.5a) shows the concentration contours are straight lines of different gradients meeting at the point of dye injection. This suggests that the evolution of dye concentration can be explained by a diffusion type process. In this plot, gas bubbles are filtered out using a one-directional median filter applied at each height. At each time, the filter returns the median of values within a given moving time window. By applying this, the anomalously low concentration related to bubbles can be suppressed.

Assuming a delta function for the dye source which then diffuses into a semi-infinite domain from $z = 0$ to $z \to \infty$, the solution for the diffusion equation is expected to be of the form

$$c(z,t) = \frac{M}{A\sqrt{\pi D t}} \exp\left(-\frac{z^2}{4Dt}\right), \tag{4.6}$$

where M, A and D are the mass of dye, cross-sectional area of the conduit and the diffusion coefficient, respectively. Figure 4.5b shows a plot of $c\sqrt{t}/c_o$ as a function of z^2/t where c_o is chosen for each experiment such that the curve is normalised to 1 at $z^2/t = 0$. The plot shows that the scaled concentration profiles collapse for all time. The data can thus be used to determine the diffusivity, D, given in (4.6) and shown as a black line in the figure.

The diffusion coefficient was found to depend on gas flow rates but not viscosity, at least within the range of viscosity $\nu = 0.01$ to 0.1 cm^2 s^{-1} for which the Reynolds numbers based on bubble speed are large. Here, Re_b, is calculated using the relation-

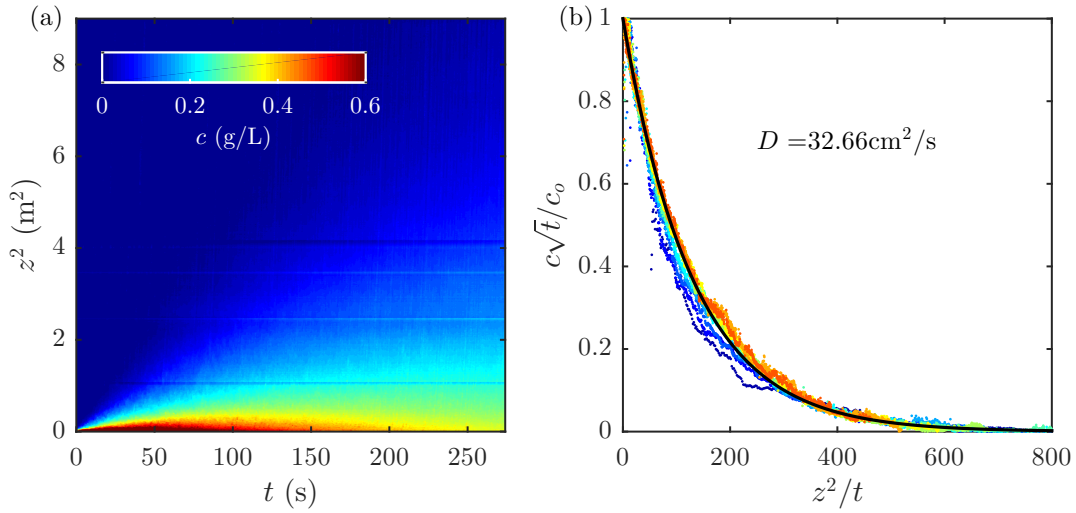

Fig. 4.5 shows the concentration profiles from a dye attenuation experiment. (a) Time series of averaged concentration re-plotted in the $z^2 - t$ domain shows a linear trend starting from the point of injection ($z = 0, t = 0$). Bubbles are filtered out using median filter over time direction. (b) Plots of normalised concentration profiles at different times, shown as plots in different colours, as a function of z^2/t shows collapse of the data confirming a diffusion-like process for dye propagation under the influence of bubble flow. The black line illustrates the best fit which determines the dispersion coefficient, D, describing this experiment.

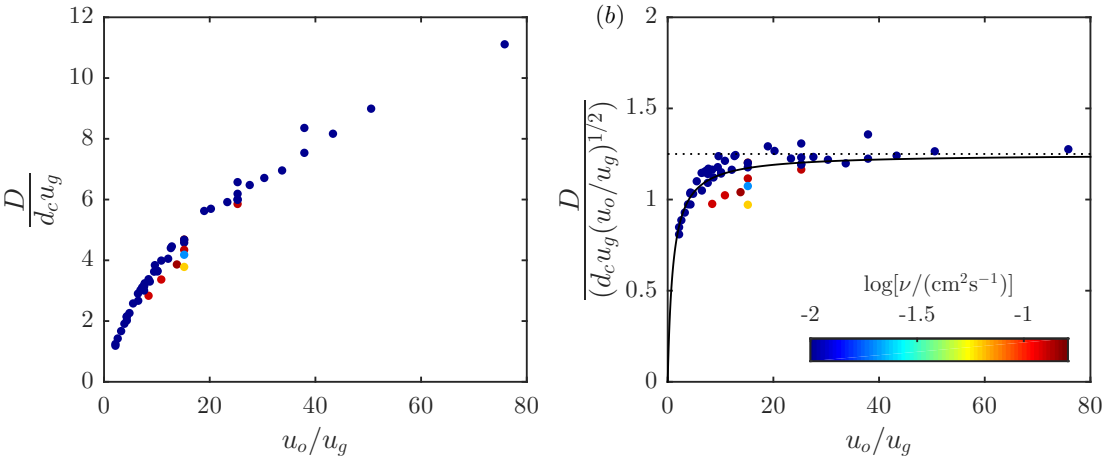

Fig. 4.6 (a) Plot of normalised diffusion coefficient, $D/(d_c u_g)$, as a function of, u_o/u_g. (b) Plot of normalised diffusion coefficient, $Du_g^{1/2}/(d_c u_g u_o^{1/2})$, as a function of, u_o/u_g. The black solid line illustrates the approximate fit to the data expressed in equation (4.9) and the dotted line corresponds to the asymptotic value expected for large u_o/u_g (4.10). The results from different liquid viscosities are plotted in different colours.

ship,

$$Re_b = \frac{u_b d_c}{\nu}, \tag{4.7}$$

where u_b is a averaged measured velocity of large gas bubbles and is found to be in excess of 800 for all experiments with $\nu < 0.1$ cm^2 s^{-1}. Note that Re_b is based on the actual slug speed, u_b, in a continuous flows and can be different from the Re_B that is based on the single slug speed, u_o, which is a function of the conduit size (1.41).

Dimensional analysis requires that the diffusivity D has dimensions L^2/T or UL, where L, T and U are length, time and velocity scales, respectively. We choose $L = d_c$ and $U = u_g = \dot{V}_g/A$ as our experiments show that D increases with u_g. This leads to the scaling law

$$D \sim d_c u_g f\left(\frac{u_o}{u_g}\right), \tag{4.8}$$

where u_o is the ascent speed of a single Taylor bubble in the case of no background flow determined using equation (1.41). In order to determine the function $f(u_o/u_g)$, we plot $D/(d_c u_g)$ as a function of u_o/u_g in figure 4.6a. However, the exact expression for $f(u_o/u_g)$ is not obvious in this plot. Instead, plotting $D/\left(d_c u_g (u_o/u_g)^{1/2}\right)$ as a function of u_o/u_g as shown in figure 4.6b suggests that the function seems to collapse to a constant at large u_o/u_g. However, we found that for small values of u_o/u_g, a slight adjustment is required to fit the data in this region. As shown by the solid line in the figure, a reasonable fit to the data is then given by the expression

$$D \approx 1.25 d_c u_g \frac{(u_o/u_g)^{\frac{3}{2}}}{1 + (u_o/u_g)} = 1.25 d_c \frac{u_g^{\frac{1}{2}} u_o^{\frac{3}{2}}}{u_g + u_o}, \tag{4.9}$$

In the case of large conduit, the superficial gas speed becomes small compared to the ascent bubble speed, $u_g \ll u_o$. This is likely to be the case for slug flows in a volcanic conduit. Also it might be more convenient to write $d_c u_g^{1/2}$ in terms of gas flux, $\dot{V}_g$, for comparison with field data. For a cylindrical conduit, $A = \pi d_c^2/4$, we may therefore write the empirical approximation for the diffusion coefficient as

$$D \approx 1.5 \dot{V}_g^{\frac{1}{2}} u_o^{\frac{1}{2}}, \tag{4.10}$$

which will be used in the following sections to model the slug flows in a volcanic conduit. This scaling law may be viewed as $D \sim UL$ where $U = (u_g u_o)^{\frac{1}{2}}$, the geometric mean of u_g and u_o while $L = A^{\frac{1}{2}} \sim d_c$, the conduit diameter.

A conduit-filling bubble in a volcanic conduit may be unstable and break up to a few smaller-sized bubbles as shown in a numerical study (Suckale *et al.*, 2010). Our experiments with small gas fluxes also show that gas bubbles may rise as clusters of a few small bubbles (figure 4.1) rather than one big slug which might resemble what it would look like when a large bubble breaks. This limit of gas flux corresponds to large u_o/u_g in figure 4.6b which is explained by the empirical relationship given in (4.10). Thus, the effect of bubble instability has been accounted for in our empirical relationship.

The dispersivity law determined from our experiments can depend on the dynamics of the flows. In our experiments, the flows are relatively inviscid with $Re_B > 2000$. As mentioned earlier, the flows within a volcanic conduit may be turbulent or transitional because the physical properties of the flows (e.g. viscosity and the conduit sizes) vary over a large range. We expect that our dispersivity law can explain the dynamics at volcanic conduits at least for those with large Re_B. However, for a small Re_B flow, the dispersion process caused by turbulent mixing is suppressed and a different model might be required. As further support of the relevance of our dispersivity law, the inertial forces overcome the surface tension at $E_o > 100$ which is found to be both for the case of our experiments ($E_o \sim 200$) and for typical volcanic conduit flows ($E_o > 10^7$) (Seyfried & Freundt, 2000).

If there exists a lava lake on top of a volcanic conduit, gas bubbles will no longer be confined within a restricted wall once they enter the lake. We expect that the mixing induced by the bubble rise may be less efficient and dispersivity might be lower. For simplicity, however, we assume the same dispersivity law (4.10) both within the lake and the conduit. This is valid for open-vent volcanoes, small lava lakes or when the depth of the lake is negligible compared to the conduit length in which the bubbles ascend.

4.5 Modelling temperature profile within a volcanic conduit

We consider here the process of heat transfer from the magma chamber to the surface via a volcanic conduit. We proposed that the heat transfer is through gradual mixing influenced by the gas bubbles rising up the conduit. However, our proposed mechanism is different from the gas bubbles-influenced mechanism proposed earlier by (Bouche *et al.*, 2010) which suggested that heat is maintained by bubbly wakes that reside in the lake and gradually lose their heat to the lake before they can escape to the atmosphere. Provided that the Reynolds number for bubble flow within a volcanic conduit is large enough to maintain turbulent mixing which is the case for many basaltic volcanic systems (Bouche *et al.*, 2010; Vergniolle & Brandeis, 1996; Vergniolle & Gaudemer, 2015), the experiments suggest that the heat budget can be gradually transported to the shallower level by a diffusion-like process, similar to those illustrated in our experiments.

4.5.1 Model development

When considering the temperature change within a volcanic conduit at a steady state for gas-magma separated flows, one might assume that the bubbles and magma have the same temperature at each depth. This implies that the heat exchange between the gas and liquid happens quickly at each level. However, the heat exchange between the melt and gas phases can be a slow process compared to the time required for the bubbles to rise along the conduit. In order to model the temperature profiles within the volcanic conduit, the temperature change of the gas and melt require separate equations to describe each phase. This allows the two phases to have different temperatures at a particular depth. We assume there is no mass exchange between the two phases, i.e. there is no effect of bubble growth due to dissolved gas diffusing into the bubble. Here we propose a solution for a quasi-steady state arisen when a constant gas flux supplying a regular frequency of gas slugs that rise in a volcanic conduit.

For the gas phase, we consider the temperature change during the ascent of bubbles, over a small vertical distance $\mathrm{d}z$, to be the result of two processes: 1) heat exchange with the surrounding magma, $-Q_T$ and 2) the work done by gas expansion, $-P\mathrm{d}V_g$. The conservation of energy requires that, $\Delta U = -Q - W$, where ΔU is the change in internal energy which will result in a temperature change of the system, Q is the

heat loss and W is the work done by the system. The change in temperature of the gas phase, per unit vertical length, in a quasi-steady state can therefore be written in terms of gas flux and heat flux as

$$c_g \dot{M} \frac{\mathrm{d}T_g}{\mathrm{d}z} = -\dot{Q}_T - P\frac{\mathrm{d}\dot{V}_g}{\mathrm{d}z}, \tag{4.11}$$

where $T_g(z)$ is the temperature of the gas phase, $\mathrm{d}\dot{V}_g/\mathrm{d}z$ is the vertical gradient in gas volume flux and P is the gas pressure. Using the ideal gas law, $PV = MRT$, where M is the mass of the gas and R is the specific gas constant, we may write the work done by gas expansion as

$$-P\frac{\mathrm{d}\dot{V}}{\mathrm{d}z} = \dot{V}_g\frac{\mathrm{d}P}{\mathrm{d}z} - \frac{\mathrm{d}}{\mathrm{d}z}\left(P\dot{V}_g\right) = \dot{V}_g\frac{\mathrm{d}P}{\mathrm{d}z} - \dot{M}R\frac{\mathrm{d}T_g}{\mathrm{d}z}. \tag{4.12}$$

For the gas density ρ_g, the gas volume flux can be converted into gas mass flux using the relation $\rho_g\dot{V}_g = \dot{M}$. Although the gas mass flux may increase with height as more volatiles exsolve from the magma, we assume the increase in the mass flux from this process is negligible and $\dot{M}$ is taken to be independent with depth. Assuming magmastatic pressure, $\mathrm{d}P/\mathrm{d}z = -\rho_m g$, the equation can then be transformed into

$$-P\frac{\mathrm{d}\dot{V}_g}{\mathrm{d}z} = -\frac{\dot{M}}{\rho_g}(\rho_m g) + \dot{M}R\frac{\mathrm{d}T_g}{\mathrm{d}z}. \tag{4.13}$$

Substituting this into (4.11) and rearranging the equation, we find that $\mathrm{d}T_g/\mathrm{d}z$ is given by

$$\left(c_g + R\right)\dot{M}\frac{\mathrm{d}T_g}{\mathrm{d}z} = -\dot{Q}_T - \dot{M}g\frac{\rho_m}{\rho_g}, \tag{4.14}$$

This allows us to calculate $\mathrm{d}T_g/\mathrm{d}z$ at any depth if $\dot{Q}_T$ is known. On the other hand, the magma temperature can be related to $\dot{Q}_T$ using the advection-diffusion equation for heat transfer in the magma

$$\frac{\partial T_m}{\partial t} = \nabla\cdot(D\nabla T_m) - \nabla(\mathbf{u}T_m) + \frac{\dot{Q}_T}{\rho_m c_m}, \tag{4.15}$$

where T_m is the magma temperature, D is the heat diffusivity, $\mathbf{u}$ is the velocity field of the magma and $\dot{Q}_T/(\rho_m c_m)$ here is considered as the heat transfer from the gas phase. Provided that the system reaches a quasi-steady state and there is no net magma flow,

$\partial T_m/\partial t = 0$ and $\nabla(\mathbf{u}T_m) = 0$. The equation advection-diffusion in one-dimension in terms of heat fluxes can be written as

$$0 = \rho_m c_m A \frac{\mathrm{d}}{\mathrm{d}z}\left(D\frac{\mathrm{d}T_m}{\mathrm{d}z}\right) + \dot{Q}_T \tag{4.16}$$

where $T_m(z)$ is the magma temperature at quasi-steady state. As illustrated in the experimental results, D is found to be a function of gas volume flux which depends on depth. Here we may use the empirical approximation of D for gas volume flux, $\dot{V}_g$. Knowing that $\rho_g \dot{V}_g = \dot{M}$, we can write the empirical values for D in terms of gas mass flux as

$$D \approx 1.5\left(\frac{\dot{M}}{\rho_g}u_o\right)^{\frac{1}{2}}. \tag{4.17}$$

Assuming ideal gas law, ρ_g is expected to increase with depth due to increasing in magmastatic pressure. The expression for ρ_g can be written as

$$\rho_g(z) = \frac{P_o - \rho_m g z}{R T_g(z)}, \tag{4.18}$$

where P_o is the gas pressure at the top of the conduit. Using (4.17) and (4.18), equation (4.16) can now be written as a second order differential equation as

$$\dot{Q}_T = -\frac{3}{2}\rho_m c_m A\left(\frac{\dot{M}u_o}{\rho_g}\right)^{\frac{1}{2}}\left(\frac{\mathrm{d}^2 T_m}{\mathrm{d}z^2} - \frac{1}{2\rho_g}\frac{\mathrm{d}\rho_g}{\mathrm{d}z}\frac{\mathrm{d}T_m}{\mathrm{d}z}\right) \tag{4.19}$$

For bubbles with much smaller diameter than the conduit diameter, d_c, D might be smaller than the empirical formula (4.17). As the effectiveness of the mixing will be likely to depend on bubble size, we suggest that D should be rescaled by the bubble radius, r_b. In this case, a factor of $4r_b^2/d_c^2$ should be included in (4.19) when considering the heat flux with small bubbles. This scaling implies that the bubble rises in a straight trajectory while in fact large bubbles may oscillate from side to side and the cross-sectional area of liquid affected by rising of a bubble may be bigger than the size of the bubble itself.

The theoretical approximation for $\dot{Q}_T$ can be explained by the heat exchange over a boundary layer on the surface of a spherical bubble. The boundary layer thickness can be scaled as $\delta \sim \sqrt{\kappa t} \sim \sqrt{\kappa r_b/u_o}$ where κ is thermal diffusivity. The conductive heat flux over this boundary layer for a single spherical bubble can be written as

$\dot{Q}_{T,s} = \rho_m c_m \kappa (4\pi r_b^2)\Delta T/\delta$. The conductive heat flux per unit conduit length can be estimated by dividing this by the slug unit length (The length of a complete slug unit comprising of gas bubbles and liquid phase behind it), $L = 4\pi u_b r_b^3/(3\dot{V}_g)$,

$$\dot{Q}_T \sim \rho_m c_m \sqrt{\frac{\kappa u_b}{r_b}}(T_g - T_m)(4\pi r_b^2)\left(\frac{3\dot{M}}{4\pi\rho_g u_b r_b^3}\right). \tag{4.20}$$

Though large gas bubbles may be observed at the surface of the lava lake suggesting slug flow within the conduit at least in the shallow level, the high pressures at depth imply these bubbles are much smaller than the conduit at deeper level. Here the rise speed of the bubble can be determined from balancing the inertia and buoyancy force,

$$u_b = 0.707\sqrt{2gr_b}. \tag{4.21}$$

By using this estimate, the maximum possible speed for a spherical bubble within the conduit can be larger than speed of the gas slug (1.41) which might not be physically sensible. In fact, bubble shape is not necessarily spherical, may be more akin to a spherical cap, and hence the gas bubble may fill up the conduit even when the equivalent diameter, should it exist as a sphere, is much smaller than the conduit diameter (figure 4.1). Here, we assume that the transition from a free bubble to a confined bubble occurs when the speed of the free spherical bubble matches the speed of a bubble confined within the walls of the conduit.

4.5.2 Model validation

Using (4.20) as an approximation for $\dot{Q}_T$ and substituting into (4.14) and (4.19), the differential equation system can be solved numerically to estimate T_g and T_m within the domain $-z_{\max} < z < 0$. Here we impose the temperature at the source depth, $z = -z_{\max} = -1$ km, for the melt and the gas to be identical, $T_g = T_m = 1000°$C. Another condition is required to solve for $T_m(z)$ as the equation is second order, we first set $\mathrm{d}T_m/\mathrm{d}z$ to be equal to $\mathrm{d}T_g/\mathrm{d}z$ at $z = -z_{\max}$. This implies that at the source, the temperature change of magma and gas are identical while in fact this is not necessarily true. However, for the first set of calculations in which we explore the model, we make this simplification. Later in the chapter, we replace this with a new boundary condition at the surface of the lava lake, matching the heat flux supplied to the lake with the heat loss from the lake. This then leads to prediction of the temperature gradients at the base of the conduit.

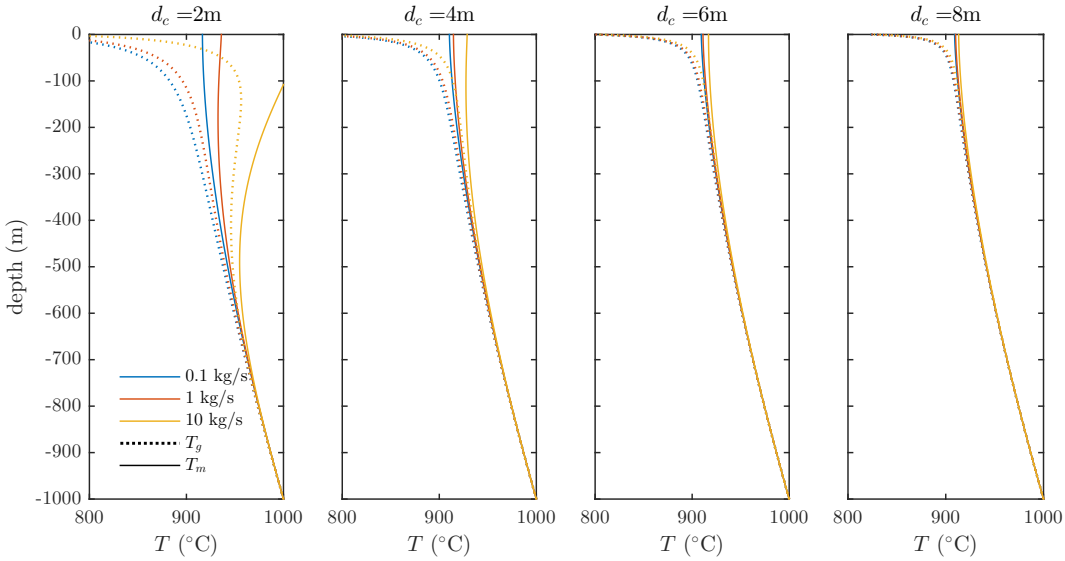

Fig. 4.7 Numerical solutions for a model concerning heat flux due to gas expansion and partial thermal exchange between gas bubble and liquid melts. The boundary conditions are set for $T_g = T_m = 1000^o$C and $\mathrm{d}T_g/\mathrm{d}z = \mathrm{d}T_m/\mathrm{d}z$ at z = -1 km.

Figure 4.7 shows the results based on these boundary conditions assuming the initial bubble size, $r_b(-z_{\max})$, is 0.5 m for all chosen conduit diameters and different gas flux will result in different bubble frequency. The bubble size, $r_b(z)$, is re-calculated at each depth based on the ideal gas law, $PV = MRT$. The observed temperature at the surface is found to be hotter in the case of a high gas flux. This can be explained by the fact that increasing gas flux leads to larger heat flux due to diffusion-like process and hence, high temperature can be maintained at the surface. With increasing conduit diameter, the temperature profiles of both phases become less dependent with the gas fluxes. The distance at which the gas and melt phases maintain the same temperature also increases with increasing conduit size, which could be because the heat exchange between the two phases are more effective when the bubbles are not conduit filling causing the two phases to remain in equilibrium.

Figure 4.8 shows the effect of gas flux, conduit diameter and initial bubble size at the base of the conduit on the predicted surface magma temperature. In general, the magma surface temperature increases with increasing gas flux but decreases with increasing conduit size. This is expected as the heat may be transported up the conduit more efficiently with a larger gas flux while it is more difficult to provide sufficient heat maintain a high temperature in the case of large conduits.

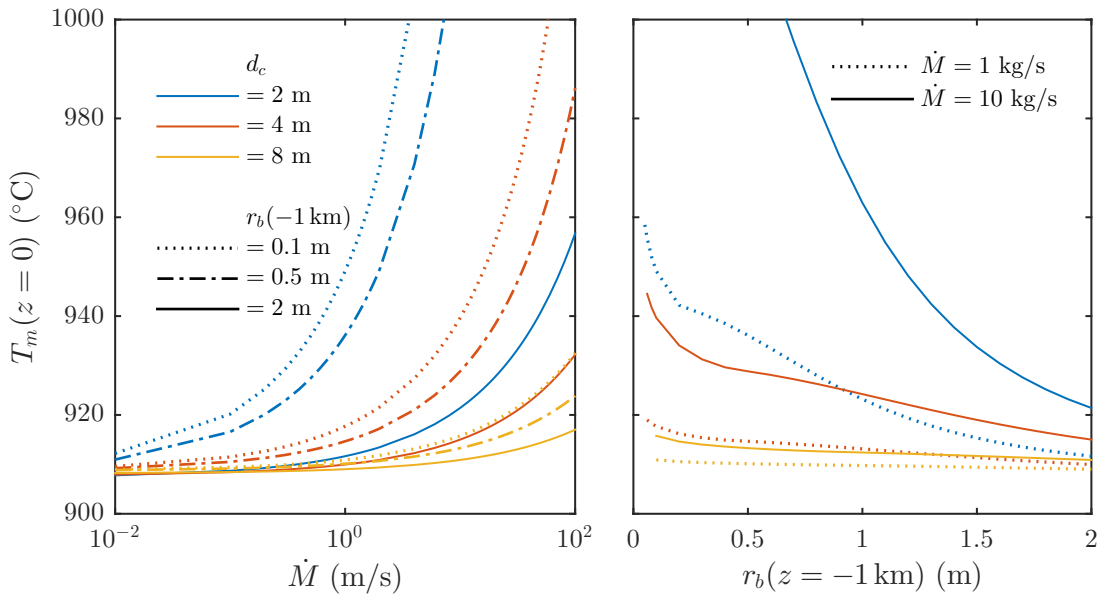

Fig. 4.8 T_m at the surface as predicted for different gas fluxes, conduit diameters and initial bubble sizes at the base of the conduit. The conduit is set to be 1 km deep and the magma temperature gradient at $z = -z_{\max}$ is assumed to be the same as the gas temperature gradient.

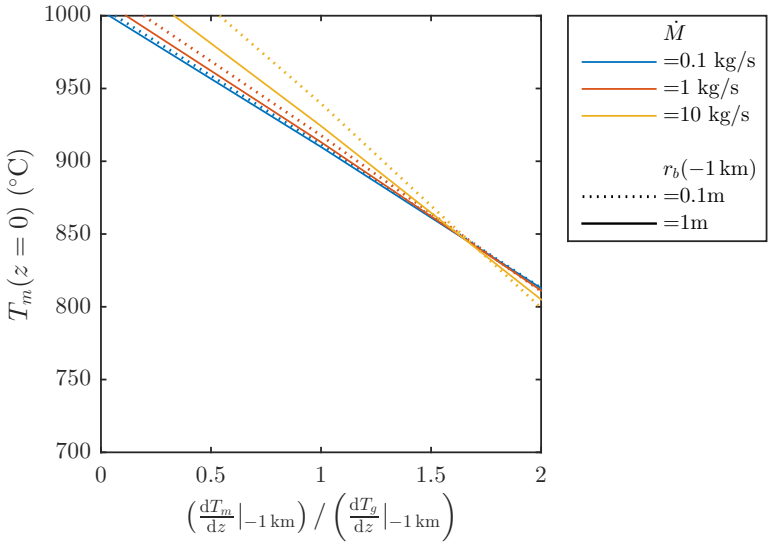

Fig. 4.9 Surface temperature as predicted by function of different $\mathrm{d}T_m/\mathrm{d}z$ at z = -1 km. The result is shown for the conduit diameter of 4 m.

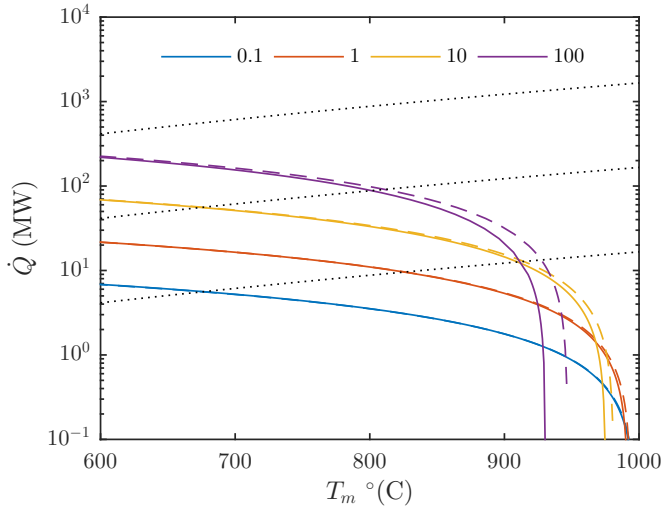

Fig. 4.10 A plot of heat supply/loss at a lava lake. Dotted lines show the estimated total heat loss ($\dot{Q}_{\rm rad} + \dot{Q}_{\rm conv}$) as a function of surface temperature T_m for lava lake of the sizes (from bottom to top) 100, 1000, 10000 m^2. Coloured lines show the predicted heat supply associated with different gas fluxes as a function of predicted temperature which is varied by changing dT_m/dz at the source depth. Dashed lines show the predicted values at 50 m below the surface while solid lines show the predicted values at the surface and are plotted as a function of their corresponding local temperatures. The model is set for $d_c = 4$ m, $-z_{\rm max} =$ -1 km and initial $r_b = 1.8$ m.

The predicted surface temperature is also found to decrease with larger initial bubble radius. This can be because the heat exchange between the two phases becomes smaller with increasing r_b (4.20) which then leads to smaller heat flux for the melt phase (4.16) and hence, cooler temperature at the surface. Based on the field observations at different lava lakes, large bubbles arrive at the surface with volumes from 10-10^4 m^3, equivalent to ∼1 to 15 m in radius. At a depth of 1 km, the temperature of a bubble may be 1000 °C but our model predicts that it cools towards 900 °C by the time it reaches the surface. At a depth of 1 km, the gas density is ∼110 times larger and the bubble radius will be ∼4.7 times smaller than those at the surface. This would result in bubble a radius of 0.2-3 m at 1 km deep.

In general, dT_m/dz at $z = -z_{\rm max}$ is not necessarily identical to dT_g/dz. Figure 4.9 shows the variation of predicted magma temperature at the surface as a function of the value assumed for dT_m/dz at $z = -1$ km. The calculation is shown for the case in which $d_c = 4$ m and as the value of dT_m/dz at $-z_{\rm max}$ ranges from 0 to 2 · dT_g/dz. The dependence of the surface temperature is more pronounced with large gas fluxes and

small initial gas bubbles. With larger conduit size, the predicted surface temperatures become independent on initial gas bubbles and gas fluxes.

Figure 4.10 shows a plot of the predicted surface temperature as a function of the heat supply estimated using our model. Here we set the source depth to 1000 m and initial bubble size of 1.8 m (equivalent to bubble radius of ≈5 m at the surface). The results for the values at the surface and 50 m below the surface are shown in solid and dashed lines respectively as a function of local temperature (T at surface and at -50 m). The heat loss associated with the lake area and surface temperature is shown by dotted lines for comparison. The figure indicates that a larger gas flux can supply a larger heat flux at the surface. The heat flux at the surface is slightly lower than the heat flux at $z = -50$ m because the temperature gradient is smaller near the surface as seen in temperature profile plot in figure 4.7.

4.5.3 Additional consideration for solidified crusts

The heat flux associated with the diffusion-like process requires magma to remain in a molten state. This implies that the temperature of the magma must always exceed its freezing point, which has been determined to be within the range of 700-800 °C. However, the surface temperatures predicted by our models suggest that, in some conditions, magma temperatures can be lower than 700 °C at the surface (figure 4.8). Based on field observations reported in the literature, solidified crusts have been observed at many lava lakes (Harris *et al.*, 2005; Patrick *et al.*, 2016; Spampinato *et al.*, 2008; Vergniolle & Bouche, 2016). Before comparing the apparent temperature that acts as the heat source for radiation and convection to the predicted temperature at the surface based on our model for heat supply by slug flows, the temperature change across this layer needs to be included.

Considering a solid crust on top of hot molten magma, heat may be conducted across the layer following the relation

$$\dot{Q}_H = -kA_{\text{lake}}\frac{\mathrm{d}T}{\mathrm{d}z}, \tag{4.22}$$

where k is the conductivity of the solidified magma, A_{lake} is surface area of the lake and $\mathrm{d}T/\mathrm{d}z$ is the temperature gradient across the layer. As there is no further heat generation or heat loss, $\dot{Q}_H$ must be the same as heat supply underneath and total heat loss above the layer ($\dot{Q}_{\text{rad}} + \dot{Q}_{\text{conv}}$).

The lava lake activities may vary in time leading to a sluggish phase (when the lateral motion of the lake is slow) and a vigorous phase (when the lateral motion of the lake is fast). The crust is expected to be thicker during the sluggish phase as the solidified magma has a longer residing time before it is recycled at the cracks (Harris *et al.*, 2005). The switching between the two modes has been previously suggested to be related to the exchanged flow within the conduits (figure 1.5)(Harris *et al.*, 2005). Yet, Patrick *et al.* (2016) showed that this needs not be the case at least at Halema‘uma‘u lava lake. Our suggested mechanism does not allow exchange flow to directly influence the convection observed at the lake surface and an alternative mechanism will be required to explain the switching between the two modes. The main focus in our proposed model is the behaviour of lava lakes in a quasi-steady state and thus does not differentiate between the different modes of the lava lake activities.

4.5.4 Transition depth to conduit-filling bubbles

Magma convection implies that exchange flows, i.e. with hot and volatile-rich magma rising at the core while warm and degassed magma descends near the wall, occurs within a conduit. This cannot be the case for conduit-filling slug flows which are expected to occur at the top part of the conduit where the gas slugs will mix and disturb the exchange flow. However, these gas slugs are smaller at depth due to higher pressure and may no longer be conduit-filling. Here, we suggest that bubble ascent and magma convection may coexist if the bubble size is not large enough to disturb the descending magma. Based on this argument, we define the transition depth as the depth at which the size of a bubble, upon its rise in the conduit, becomes large enough to prevent magma convection at the shallower depths. We interpret this to be the point at which heat transfer mechanism shifts from magma convection to a bubble-induced diffusion-like process. To estimate the depth at which there is a transition so that bubbles become conduit-filling, we first estimate the volume of a single bubble at depth using the relationship,

$$\dot{M} = V_b \rho_g \omega, \tag{4.23}$$

where V_b is the volume of a single gas bubble and ω is the bubble frequency. Assuming that density change due to magmastatic pressure is much larger than the density

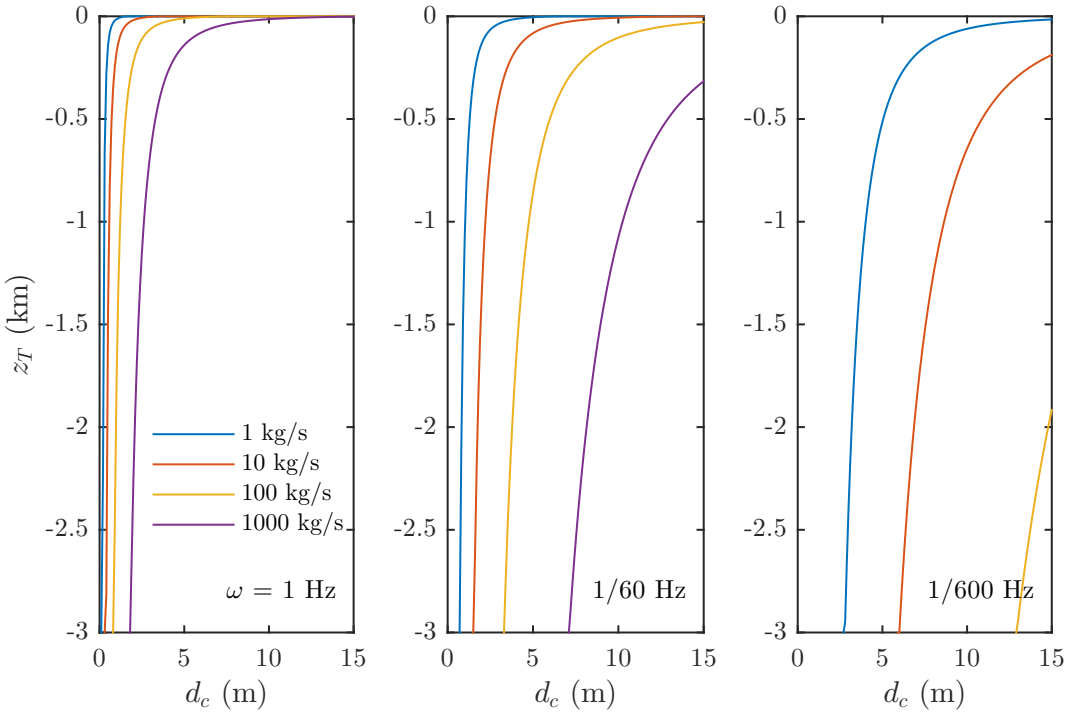

Fig. 4.11 Plots of estimated transition depth where the gas bubble becomes conduit filling as a function of conduit diameter for given gas flux and bubble frequency. The bubble frequency chosen is equivalent to bubble appearance of (from left to right) one every second, minute and ten minutes.

change due to temperature variation within the conduit, ρ_g can be written as

$$\rho_g = \frac{P_o - \rho_m g z}{R\hat{T}}, \tag{4.24}$$

where P_o is a reference pressure, $\hat{T}$ is a characteristic temperature within the conduit and R is the gas constant. Using $\rho_m = 2600$ kg m^{-3}, $\hat{T} = 1273$ K, $R = 189$ J kg^{-1}K^{-1} (gas constant for CO_2) and $P_o = 101,325$ Pa at $z = 0$ for calculation, figure 4.11 shows the estimated transition depth for different gas fluxes and bubble frequencies as a function of conduit diameters, d_c. Here we assume the bubbles are spherical and the bubble radius, r_b, can be determined from $V_b = 4\pi r_b^3/3$. The transition depth is chosen where $r_b = d_c/2$, defining the point where the spherical bubbles are assumed to fill the conduit. These boundary conditions will be used as constraints for the initial bubble size and initial depth at which we begin the calculation.

Figure 4.11 shows that for a particular conduit size, the transition depth is shallower for a smaller gas flux compared to a larger gas flux. This is because a smaller gas flux implies smaller size bubbles for a given frequency and hence the bubbles only fill the conduit at a shallow level. For a given gas flux, a decrease in the bubble frequency results in larger bubble radius. Hence, the bubble can become conduit filling at a deeper level. The transition depth can be deeper if bubbles are deformed into ellipsoidal or spherical caps, as their radii are bigger than that of spherical bubbles of the same volume.

The transition depth can also be expected to be deeper in the presence of significant liquid film thickness around rising bubbles. Llewellin *et al.* (2012) found experimentally that the film thickness depends on the Reynolds number based on the buoyancy forces, Re_B, (1.43) and the film thickness can be as large as 33% of the conduit radius for $Re_B \lesssim 10$ but becomes smaller with increasing Re_B. At $Re_B \gtrsim 10^4$, the film thickness becomes independent of Re_B and converges to $\approx 8\%$ of the conduit radius.

By combining the gas composition data, mostly determined using an open-path Fourier transform infrared (FTIR) spectroscopy, to the total flux of SO_2 routinely measured at many volcanoes, total degassing has been reported at each volcano. Alternatively, gas bubble bursting at the surface generates acoustic and seismic waves that can be analysed and related back to the bubble volumes and hence, gas fluxes. It has been noticed that these estimated gas fluxes based on the latter technique appears to be lower than that measured directly using the FTIR by an order of magnitude (Vergniolle & Gaudemer, 2015). It is suggested that while the FTIR technique measures total amount of degassing, only a portion of over-pressurised gas bubbles, originated from deep levels, is detectable by the acoustic measurement.

We note that in our calculations, the transition depth estimated here and in further calculations is estimated based on the radius of spherical bubbles and neglegible film thickness around them. The estimation of the transition depth constrains the depth at which the magma temperature starts to drop from the temperature associated with the convective exchange flow. This depth can be imposed as the boundary for our model when considering heat flux associated at each lava lake, which will be illustrated in the next section.

	data			assumption		prediction	
	bubble period	$\dot{M}$ (kg/s)	A_{lake} (m^2)	crust	T_{lake} (°C)	z_T (m)	d_c (m)
Erta 'Ale	50 mins	0.804	910	✓	700-920	680-340	4-5
Erebus	24 hrs	0.12	1200	✓	710-900	280-140	4-5
Stromboli	4.8 mins	0.0067	4.7	×	700-800	350-240	2.2-2.5
Villarica	18.75 s	4.59	550	×	850-950	95-50	2.5-3

Table 4.1 A summary of the bubble period, gas flux and lava lake used in heat balance analysis based on our predicted heat supply due to bubble flows. The condition for a 10 cm solidified crust on top of the lake is included when the heat balance suggests a lake temperature of lower than 700-800 °C. The conduit diameter, d_c, is then predicted based on this analysis for each lava lake.

4.6 Application to geological problems

In this section, we apply our proposed model to some lava lakes where the information about gas fluxes and bubble frequencies are available. The model is used to predict the surface temperature which can be compared to the heat loss estimated by the lake surface area. Based on further assumption about information about the molten magma temperature below solidified crusts, the information about the conduit diameter can be estimated. The lake surface temperature and surface area can be observed, measured and interpreted directly, whereas the studies on gas fluxes and bubble characteristics require more complicated instruments and interpretations. The detailed studies about degassing and bubble characteristics are, therefore, more limited at many lava lakes. Hence, we only present data at a couple of lava lakes where both types of studies are available. Table 4.1 summarises the predicted d_c and z_T at Erta 'Ale, Erebus, Stromboli and Villarica. We later show that based on conduit diameter estimated by Burgi *et al.* (2014), our model can also be used to predict the bubble frequency at Nyiragongo.

4.6.1 Erta 'Ale

At Erta 'Ale lava lake, the surface of the lake was observed to be typical of lava lakes and consists mostly of one to several cold plates. In December 2004, however, it became completely solidified consisting of four hornitos, where the lake degasses. At this time, the lake level was at high level (∼88 m from the crater floor) and had a very large area (∼2-3 $\times 10^4$ m^2) (Vergniolle & Bouche, 2016).

Near surface bubbles were reported from the observations in 2003 to have the gas volume in the the range of 36-700 m^3 bursting every 40-60 mins (Bouche *et al.*, 2010) which is equivalent to a gas flux of 0.01-0.3 m^3 s^{-1}. The total gas flux of $\sim$ 8 kg s^{-1} measured using open-path FTIR was reported for the observation in 2005 (Sawyer *et al.*, 2008). Based on this data and assuming gas temperature of 650 °C and atmospheric pressure (101,325 Pa) suggests a gas flux of order $\sim$ 30 m^3 s^{-1}. This is much larger than the gas flux determined from acoustic measurements. However, the total gas flux at the lava lake has varied quite significantly throughout the history with the lowest value of 1.38 kg s^{-1} reported in 1973 (Le Guern *et al.*, 1979). Also, it has been argued that acoustic measurement only detects active over-pressured bubbles that originated at depth while the open-path FTIR measures the total degassing (Vergniolle & Gaudemer, 2015). Based on the reported gas flux at an active pool at Erta 'Ale (Oppenheimer *et al.*, 2004) compared to the fumerollic passive degassing within a nearby crater, Vergniolle & Gaudemer (2015) approximated that the active degassing from bubbles rising through the conduit will only be 7 times smaller than the total gas flux.

The surface temperature and area of the lava lake have been reported in several studies since 1973, showing variations from 910 to 7600 m^2 for the lake area and 200 to 600 °C for the radiative temperature (Le Guern, 1987; Oppenheimer *et al.*, 2004; Oppenheimer & Yirgu, 2002; Spampinato *et al.*, 2008). The maximum temperature of 1174 °C is observed at cracks in between solidified lava crusts (Oppenheimer *et al.*, 2004).

To begin our analysis, we make an initial estimate of the diameters of the volcanic conduit that feeds the lake to be possibly within the range 4-7 m. The transition depths associated with these conduit sizes can be determined from the gas flux, 5.63 kg s^{-1} (Oppenheimer *et al.*, 2004), and bubble frequency, 50 mins (Bouche *et al.*, 2010). Figure 4.12a shows the the transition depths calculated for gas flux at Erta 'Ale lava lake in the black line. From this plot, the transition depths are suggested to be approximately at 680, 340, 200 and 120 m for the chosen conduit diameters of 4, 5, 6 and 7 m, respectively.

Using these conduit sizes and corresponding transition depths, determined from figure 4.12b, as constraints, the prediction for gas fluxes arriving at the surface of the lava lake is presented as a functional plot of predicted surface temperature (figure 4.12b). In these calculations, the boundary condition $T_{\max} = 1000$ °C is chosen for

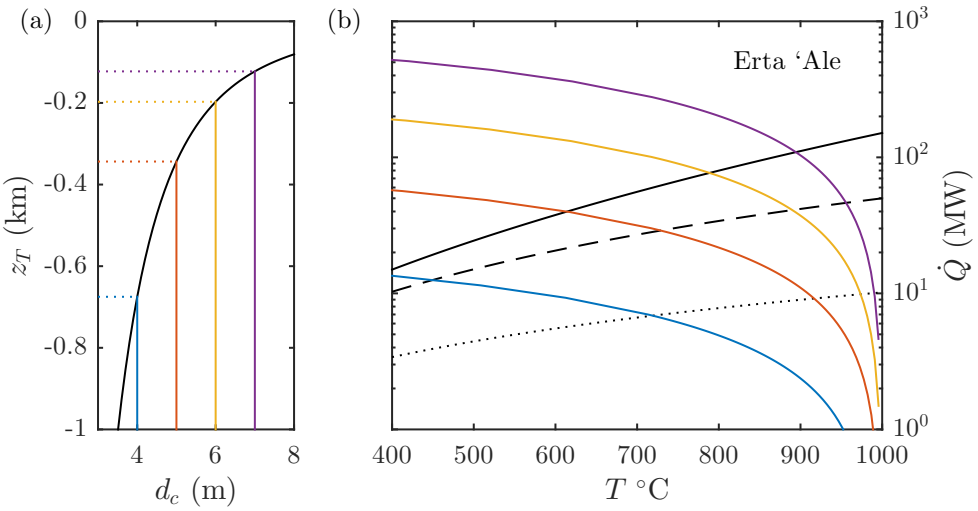

Fig. 4.12 Comparison between our model and the field data acquired from Erta 'Ale lava lake. (a) A plot of transition depth based on information of gas flux and bubble frequency is shown in black. Three conduit diameters (4, 5, 6, 7 m) are chosen in order to calculate the heat flux at the surface. The transition depths at which bubbles become conduit-filling are determined for each conduit diameter. (b) Lines in different colours show the predicted heat supply at the surface as a function of surface temperature for each chosen diameter. This is calculated using the corresponding z_T for each conduit size, read from panel (a), as the boundary where the temperature starts to drop from $T_{\max} = 1000$ °C. The solid black line shows the calculated heat loss ($\dot{Q}_{\text{rad}} + \dot{Q}_{\text{conv}}$) as a function of surface lake temperature. The dashed and dotted black line show the calculated heat loss as a function of estimated molten lake temperature when including 1 and 2 cm thick conductive solidified crusts, respectively.

the depth at $-z_{\max} = z_T$. This is an approximate temperature of magma within a volcanic conduit (Harris, 2008; Harris & Stevenson, 1997).

To compare the predicted surface temperatures to the reported heat loss at the surface, heat radiation and heat convection are calculated as a function of the lake surface temperature and shown by the solid black line in figure 4.12b. Here we use the lake area of 910 m^2 associated with the lake when the gas flux was measured (Oppenheimer *et al.*, 2004). Assuming no solidified crust is formed, the predicted surface temperatures will be the same as the temperatures of the radiation and convection heat source. The intersections between the predicted heat fluxes (coloured lines) and the calculated heat loss (solid black line) suggests balances between the heat supply and the heat loss at the lake. This leads to estimates of the lake temperatures of $\sim$ 400, 600, 800 and 880 °C which correspond with the conduit diameters of 4, 5, 6 and 7 m respectively.

However, field observations at the lava lake suggest that magma appears as solidified crusts at the lake surface. Based on the total heat loss at the surface, we can calculate the temperature gradient across the conductive layer. By further assumption on the thickness of the solidified layer, the temperature below the crust – associated with the molten magma underneath – can be determined using (4.22). We assume a uniform characteristic thickness over the whole lake in the calculation, though we note that it is likely that the crust will be thin near the upwelling magma, and will become thicker as it is further away. In figure 4.12b, the dashed and dotted lines show the plots of the total heat loss as a function of molten magma temperatures in the case of 1 and 10 cm thick conductive layers, respectively. In this calculation, we use $k = 1.67$ W m^{-1} K^{-1}, proposed to be an averaged thermal conductivity for basalts (Sharma, 1997). The chosen thicknesses are in the orders of magnitudes of Harris *et al.* (2005)'s calculation based on a mathematical model for lava flows (Hon *et al.*, 1994) i.e. ∼2.5 and ∼8.5 cm during the sluggish and vigorous phases, respectively.

By including the temperature drop due to the heat conduction through a 1 cm thick crust, the balancing points for heat loss and heat supply suggest the lake temperatures associated with the conduit diameters of 4, 5, 6 and 7 m to be 450, 720, 880 and 950 °C, respectively. For a 10 cm thick crust, the predicted magma temperature increases by approximately 50-200 °C depending on the conduit size. From this analysis, we conclude that for the crust of 1 cm thick formed at the surface, a conduit diameter of at least 5.0 m is needed for the lake to have a temperature of greater than ∼720 °C, which is required to keep the lake in a molten state. A smaller conduit might also be able to maintain the molten magma but a thicker crust will be expected. In addition, our model assumes that gas bubbles immediately escape the lake once they reach the surface. In fact, clusters of small bubbles from the wake of conduit-filling bubbles may reside for a significant period and provide additional heat flux to the lake before they can escape to the atmosphere (Bouche *et al.*, 2010). However, if the bubbly wake accounts for ∼ 20% of the total active degassing (approximated from Bouche *et al.*, 2010) and the gas temperature further drops by 100 °C; the additional heat flux, $\dot{Q} = \dot{M} c_g \Delta T_g$, will only account for ∼25000 W.

We note that the surface area, as well as the level, of the Erta 'Ale lava lake has varied throughout the history. This has been explained by the thickness of a stable foam layer at the top of the magma reservoir (Vergniolle & Bouche, 2016). Since the crater has a funnel-like shape, a higher lake level will result in a larger exposed surface area and lead to more heat loss through radiation and convection processes. The

graphical representation for the increase in the area of lava lake will be equivalent to shifting the heat loss line (the black solid line in figure 4.12) upwards. This is opposite to what happens when the calculation includes solidified crusts. Consequently, in order to compensate this effect of greater heat loss such that the heat supply can still balance the heat loss for a given lake temperature, our model suggests the formation of thicker solidified crusts. This corroborates with the observation in December 2004 (Vergniolle & Bouche, 2016) when the lake had a very high level and thus, covered a large area. The lake appeared as a solidified surface which we interpret as a very thick crust that must be required in our model to maintain the molten magma underneath.

4.6.2 Erebus

Erebus volcano hosts two lava lakes containing phonolitic magma, which has a viscosity as high as 1600 Pa s, the highest among lava lakes considered in this section. Bubbles with diameter of 1.1 - 8.7 m burst at the surface of the lakes every 3-5 mins (Calkins *et al.*, 2008). Assuming a spherical bubble, this is equivalent to bubble volume of $\sim 0.003 - 1$ m^3, which is an order of 100-1000 smaller than the mass flux of 27.3 kg s^{-1} ($\sim$ 80 m^3 s^{-1} using the same assumption as above) as reported by Oppenheimer & Kyle (2008) based on the FITR technique. On top of these metre-scale bubbles, several Strombolian eruptions which resulted from larger bubble bursts ($\sim$10-30 m in diameter – Peters *et al.*, 2014) have been observed daily (Jones *et al.*, 2008; Rowe *et al.*, 2000). Study in acoustic wave forms estimates the mass of these large gas bubbles to be an order of 10^3 kg (Johnson *et al.*, 2004). Assuming the averaged frequency for these large over-pressurised bubbles to be 10 per day, this results in gas flux of $\sim$0.12 kg s^{-1}, only about 1% of the total gas flux measured using the FTIR technique (Oppenheimer & Kyle, 2008). The field data in 1985 and 1989 for lava lake area were reported to be 180 and 300 m^2 together with their corresponding radiative surface temperatures of 788-903 and 574-716 °C respectively (Harris *et al.*, 1999).

While the Strombolian eruptions are believed to be caused by bursting of over-pressurised decametre-scale bubbles originated from depth (Burgisser *et al.*, 2012; Oppenheimer *et al.*, 2011), the origins for smaller (metre-scale) bubbles are uncertain and possibly formed from within the lake (Peters *et al.*, 2014). Here we apply a similar analysis using the information from Erebus volcano, using approximated bubble recurrence time of 2.4 hours and a gas flux of 0.12 kg s^{-1}, associated with the gas flux of large bubbles that cause Strombolian eruptions. The gas transition depths associated with conduit diameters of 4, 5 and 6 m are estimated to be approximately at 280,

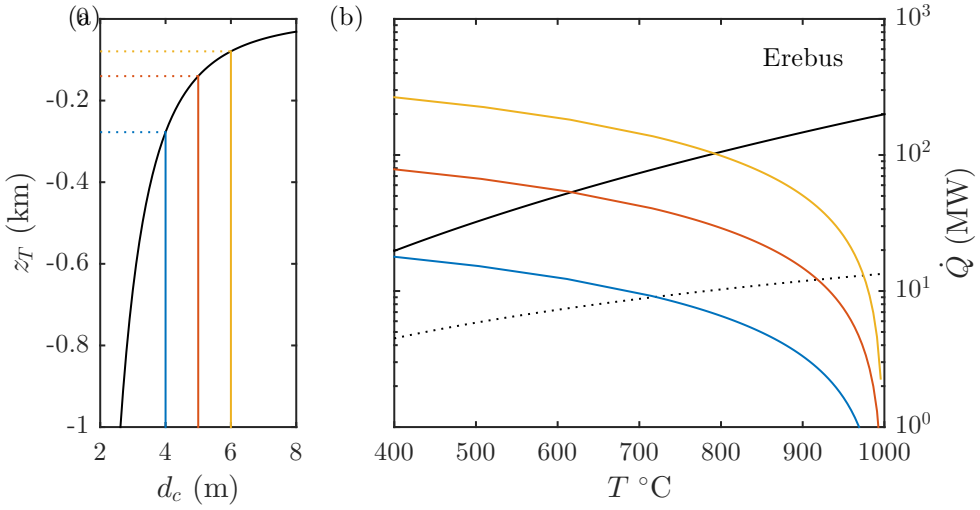

Fig. 4.13 Comparison between our model and the field data acquired from Erebus volcano. (a) A plot of transition depth based on information of gas flux and bubble frequency is shown in black. Three conduit diameters (4, 5, 6 m) are chosen in order to calculate the heat flux at the surface. The transition depths at which bubbles become conduit-filling are determined for each conduit diameter. (b) Lines in different colours show the predicted heat supply at the surface as a function of surface temperature for each chosen diameter. This is calculated using the corresponding z_T for each conduit size, read from panel (a), as the boundary where the temperature starts to drop from $T_{\max} = 1000$ °C. The solid black line shows the calculated heat loss ($\dot{Q}_{\text{rad}} + \dot{Q}_{\text{conv}}$) as a function of surface lake temperature. The dotted black line shows the calculated heat loss as a function of estimated molten lake temperature when including a 10 cm thick conductive solidified crust.

140 and 80 m below the surface, respectively. The temperature at the surface is then compared to the expected heat loss by a lava lake size of 1200 m^2, taken from the mean surface area of the two lakes (Calkins *et al.*, 2008). Excluding the crust on the lake surface, the lake temperatures at the balancing points for the conduit diameters of 4, 5 and 6 m are predicted to be approximately 400, 600 and 790 °C, respectively (figure 4.13). By including a 10 cm crust, the predicted lake temperatures increase to 710, 920 and 980 °C, respectively. From this, we conclude that if a 10 cm crust is formed at Erebus, a conduit diameter of at least 4 m is required in order to keep the lava lake in a molten state (lake temperature of ∼750-850 °C).

4.6.3 Stromboli

Strombolian eruptions observed at Stromboli volcano have been described to be the result of bubbles bursting at the surface. Harris & Stevenson (1997) used Electronic Distance Measurements (EDM), which indicated that explosive events occur from between 5 and 15 open vents situated within the crater terrace at Stromboli. Vent temperatures between 830 and 940 °C were reported based on the observed temperature of an incandescent vent wall at the two vents. Studies of the acoustic wave form of bubbles breaking at the surface suggest the bubbles have a radius of 1 m, which is approximately the same size as the conduit radius, with the length ranging from a few to tens of meters (Vergniolle & Brandeis, 1996). Together with the bubble frequency being 5-20 events per hour (Del Bello *et al.*, 2012), this would suggest a gas flux of ∼0.01-0.2 m^3 s^{-1}. Direct measurements made between 1980-1993 suggest a total gas flux of ∼70-140 kg s^{-1} (Allard *et al.*, 1994) equivalent to ∼170-600 m^3 s^{-1} using the same assumption as above. By studying gas venting activity at the volcano, Tamburello *et al.* (2012) suggested that active degassing by these large bubble bursts can account for 7% of total degassing. Acoustic and seismic studies suggest the bubble source to be about 250 m below the surface though, it was argued that this estimated source depth might actually reflect the point where bubbles pass a conduit discontinuity rather than the depth of the origin of the bubbles (Burton *et al.*, 2007; James *et al.*, 2006). Another type of non-passive degassing, known as puffing, accounting for ∼16% of the total gas flux, can also be observed at the volcano (Harris & Ripepe, 2007; Tamburello *et al.*, 2012). Puffing is observed to occur more frequently, once every 1 to 2 s (Ripepe *et al.*, 2002).

At Stromboli, we assume that the heat supply from the mixing associated with the gas slugs balances the total heat loss within the crater terrace comprising 10 open-

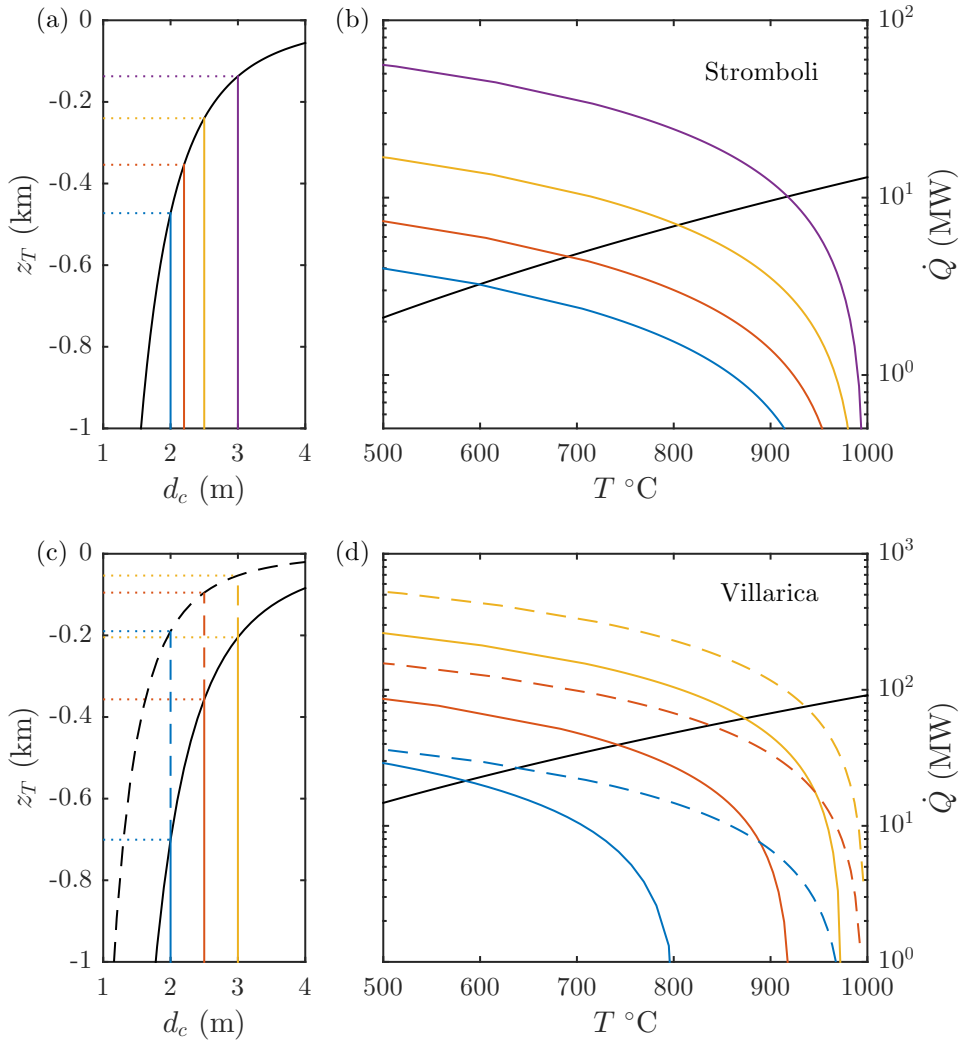

Fig. 4.14 Comparison between our model and the field data acquired from Stromboli and Villarica volcanoes. (a, c) plots of transition depth based on information of gas flux and bubble frequency are shown in black. Here we choose the conduit diameters of 2, 2.2, 2.5, 3 m for Stromboli and 2, 2.5, 3 m for Villarica. (b, d) Lines in different colours show the predicted heat supply at the surface as a function of surface temperature for each chosen diameter. This is calculated using the corresponding z_T for each conduit size, read from panel (a,c), as the boundary where the temperature starts to drop from $T_{\max} = 1000$ °C. The solid black line shows the calculated heat loss ($\dot{Q}_{\text{rad}} + \dot{Q}_{\text{conv}}$) as a function of surface lake temperature. At Villarica, (c-d), the solid and dashed lines associated to the calculations based on total and active degassing, respectively.

vents, each with the radius of 1-2 m. The total gas flux of 105 kg s^{-1}, as the mean value of the reported range 70-140 kg s^{-1} (Allard *et al.*, 1994), is used for the calculation. First, we focus on large bubbles associated with the Strombolian eruptions which account for 7% of the total gas flux. Our models predict the transition depths of 470, 350, 240 and 140 m; and the surface temperature of 600, 700, 800 and 920 °C for the chosen conduit diameters of 2, 2.2, 2.5 and 3 m, respectively. It can be seen that conduit diameters of 2.2-2.5 m are enough to maintain molten magma without further inclusion of solidified crusts into the models. We then attempt the same calculation but use the information on the gas puffs which accounts for 16% of the total gas flux. However, with the bubble frequency of 0.75 Hz, associated with the puffing, the bubbles are relatively small and not conduit filling until the uppermost 10 m for the conduit diameter as small as 2 m. As a result, it appears that the gas bubbles associated to gas puffs may not account adequately for the heat transport from depth to the surface.

While previous acoustic and seismic studies at the volcano suggested a shallow origin, ∼250 m, for the slug genesis, Burton *et al.* (2007)'s study on the magmatic gas composition suggested deeper origins within the range 0.8-2.7 km below the vents. They argued that the geophysical data rather reflect a permanent structural discontinuity rather than the actual depth to the slug genesis (James *et al.*, 2006). Although our models predict the transition depths to be relatively shallow (470-240 m) for the conduit diameters of 2-2.5 m, the predicted transition depths may be deeper if other conditions are considered in the calculations. These include the existence of the film thickness, non-spherical bubble shape or longer bubble recurrence time which will cause the bubble to become conduit-filling at deeper levels.

4.6.4 Villarica

The summit pit at Villarica stratovolcano exists as a small lava lake (30-40 m diameter) or an open, degassing, vent depending on the magma level. Thermal imaging above the vent shows the lava lake emits clouds of hot gas with temperature of 600-700 °C (Gurioli *et al.*, 2008). No thermal image of the lake surface is available but the lake appears as always molten without a solidified crust, implying the surface temperature of lava is higher than the freezing point of the magma. The total gas flux of 45.9 kg s^{-1} was measured using open-path FTIR spectroscopy (Sawyer *et al.*, 2011). We assume the gas is released at the surface with atmospheric pressure (101,325 Pa), temperature 650 °C, and that based on the reported mass fraction of H_2O and CO_2, there is a gas

flux of ∼150 m^3s^{-1}. This is within the gas flux range 30-370 m^3 s^{-1} generated by a typical bubble of volume ∼200 - 2500 m^3 bursting at a frequency of 8.8 per minute as reported by Gurioli *et al.* (2008). Excluding the data on gas puffing, referred to as type I events in their study, the bubble frequency reduces to 3.2 per minute. However, the gas mass fluxes associated with each different type of degassing are not available.

Based on the gas flux of 45.9 kg s^{-1} (Sawyer *et al.*, 2011) and total bubble frequency of 8.8 per minute (Gurioli *et al.*, 2008), the transition depths associated with the conduit diameters of 2, 2.5 and 3 m are predicted to be 700, 350 and 200 m below the surface (the solid line in figure 4.14a), respectively. Using a lava lake surface of 550 m^2 (Gurioli *et al.*, 2008), predicted surface temperatures are found to be 590, 750 and 890 °C for heat supply by the chosen conduit diameters (2, 2.5 and 3 m - figure 4.14b). The images of the lava lake (Moussallam *et al.*, 2016) showed that the surface of the lava lake is always molten without the formation of solidified crusts. To keep the magma in molten state, our models suggest that a conduit diameter of at least ∼2.5 m is required.

As it has been suggested for other volcanoes that puffing is likely to caused by bubbles originated from a shallow depth (Peters *et al.*, 2014), we then repeated the calculations excluding this type of degassing. Although the bubble frequency for more powerful bubble bursts was reported at the lava lake (Gurioli *et al.*, 2008), the gas flux from such events have not been quantified. This may possibly range from ∼7% to ∼14% of the total degassing as suggested for Stromboli (Tamburello *et al.*, 2012) and Erta 'Ale (Vergniolle & Gaudemer, 2015), respectively. If the gas flux associated with over-pressurised bubbles accounts for 10% of the total detected gas flux, the transition depth is expected to be shallower for a given conduit size as shown in the black dashed line in figure 4.14a. The predicted transition depths for conduit diameters of 2, 2.5 and 3 m now become 190, 95 and 50 m, respectively. As a result, high temperature can be maintained up to shallower levels by magma convection and increases the lake temperature to be 650, 850 and 950°C for the three chosen conduit diameters (the dashed lines in the figure 4.14b).

4.6.5 Nyiragongo

Nyiragongo is one of the largest lava lakes discovered on Earth. Recent studies reported the lake surface area of 46550 m^2 in 2010-2011 (Burgi *et al.*, 2014) and 31400 m^2 in 2012 (Spampinato *et al.*, 2013). The gas flux was measured in 2005 and 2006 to be 349

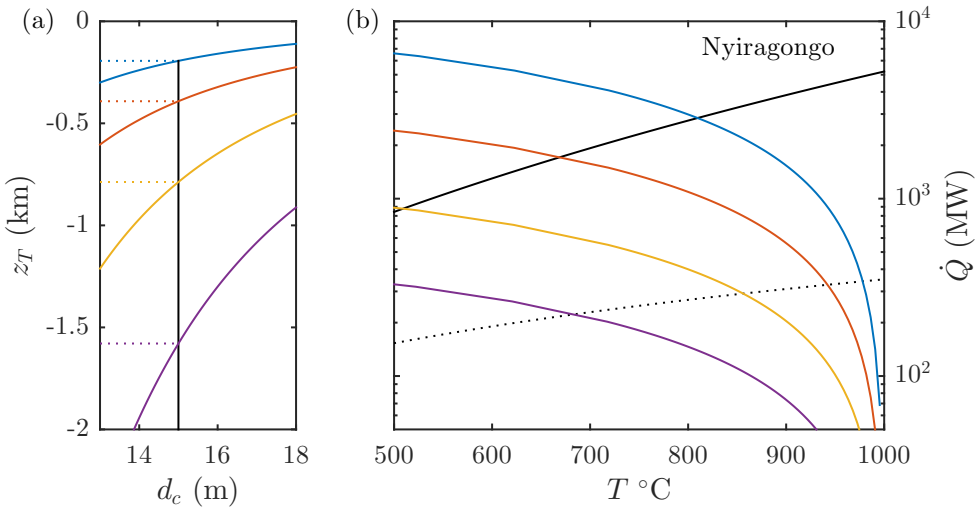

Fig. 4.15 Comparison between our model and the field data acquired from Nyiragongo lava lake. (a) A plot of transition depth based on information of gas flux and bubble frequency is shown coloured lines. The blue, red, yellow and violet curves are associated with chosen bubble occurrence times of 0.5, 1, 2 and 4 hours, respectively. Here we fix the conduit diameter to be 15 m and z_T is predicted for each chosen bubble frequency. (b) Lines in different colours show the predicted heat supply at the surface as a function of surface temperature for each chosen bubble frequency. This is calculated using the corresponding z_T for each conduit size, read from panel (a), as the boundary where the temperature starts to drop from $T_{\max} = 1000$ °C. The solid black line shows the calculated heat loss $(\dot{Q}_{\text{rad}} + \dot{Q}_{\text{conv}})$ as a function of surface lake temperature. The dotted black line shows the calculated heat loss as a function of estimated molten lake temperature when including a 10 cm thick conductive solidified crust.

and 206 kg s^{-1} respectively (Sawyer *et al.*, 2008) yet detailed information for bubble characteristics are not available at this lava lake.

At Nyiragongo, although the total gas flux was reported, the information about bubble frequency is not available and the gas fluxes associated to quiescence degassing, gas puffs and over-pressurised bubbles are not differentiated. However, the conduit diameter has been estimated to be 15 m based on draining time observed during a field exploration (Burgi *et al.*, 2014). Using this estimated conduit diameter and further assumption that over-pressurised bubbles account for 10% of total degassing, we may estimate the bubble frequency that is required to maintain the molten lava at the surface. Our model including a 10 cm solidified crust suggests that large bubbles must occur at least every 4 hours to maintain molten magma of temperature 700 °C in the lake (figure 4.15). With higher bubble frequency, the lake is expected to be hotter.

4.7 Conclusion

We have described a series of experiments that illustrate the role of slug flows in a vertical conduit in transporting dye tracers from the base to the top of the conduit without net liquid flow. The dye can be seen to disperse in a diffusion-like process whose dispersivity can be measured using a light attenuation technique. We estimate that the dispersivity is determined to be $D = 1.25 d_c u_g^{1/2} u_o^{3/2} (u_g + u_o)^{-1}$, where u_g is the superficial gas speed and u_o is the rise speed of single gas slugs determined from the conduit diameter.

Although the conceptual model for heat being supplied at lava lakes by magma convection has been widely accepted, the presence of conduit-filling – as reported to be observed at many lava lakes – seems to contradict this mechanism. Here we propose that the heat transfer within the upper part of a volcanic conduit is caused by the mixing in the wakes of the slugs which rise up the conduit, in an analogous fashion to the laboratory experiments in which we showed how dye is mixed along a pipe by a stream of bubbles. At depth, bubbles can be of smaller size and the rise of bubble and magma flow may both operate. The transition from one regime to the other occurs at that depth in the conduit when the bubbles decompress, expand and begin to fill the conduit. At this point, the mechanism for heat transfer shifts from magma convection to dispersion of heat under the influence of bubble flows.

We develop a mathematical model to estimate the heat flux that arrives at the surface using our experimental data of dye dispersivity to constrain the dispersive heat flux. The predicted heat flux is found to be comparable to the heat loss by radiation and air convection at the surface of lava lakes. Using field data for bubble frequencies and gas fluxes, we show that our model can be used to predict the size of the volcanic conduit at Erta ‘Ale, Erebus, Villarica and Stromboli.

Chapter 5

Conclusions and future work

In this chapter, we summarise the experimental techniques and key findings from our study in mixing in gravity currents (5.1) and two-phase separated flows (5.2). Some potential future work is also proposed building from the present results.

5.1 Mixing in axisymmetric gravity currents

5.1.1 Conclusion

We have described a new series of laboratory experiments to inverstigate the dynamics of mixing in axisymmetric turbulent gravity currents. The experimental tank has an increasing width as a function of the distance downstream, and so the current resembles a sector of an axisymmetric gravity current. The tank is initially filled with fresh water and the current is formed from an aqueous salt solution being introduced either by a sudden release of a finite volume (chapter 2) or a continuous supply at a constant flow rate (chapter 3). The experiments were chosen to include only the flows that have Reynolds number in excess of 3000 to ensure the frictional stresses do not dominate the dynamics, which is beyond the scope of this study.

For the study of turbulent axisymmetric gravity currents produced from a sudden release of a finite volume explored in chapter 2, we found that the position of the nose increases with time as $r_n \approx (1.28 \pm 0.05)B^{1/4}t^{1/2}$, in agreement with the scaling law suggested by Huppert & Simpson (1980). Both the maximum depth of the head and the vertical integral of the buoyancy in the head are found to decrease with time. In the chapter, we estimate the maximum depth as a function of the front position and it is found to decrease as $h_n \sim 0.5H(r_o/r_n)^{1/4}$ while the maximum value of the vertical

integral of the buoyancy is found to decrease as $(\overline{g'h})_n \sim 0.9Br_n^{-2}$. The Froude number associated with the propagation speed and the vertical integral of the buoyancy within the head, Fr_n, is found to be approximately 0.86 ± 0.07. The results from the light attenuation experiments, which measure the cross-current averaged density of the flow, show that the buoyancy of the current is stratified both laterally and vertically.

By injecting a parcel of dye in the ambient fluid ahead of the current, we illustrate that as the ambient fluid is displaced by the nose, a fraction of it is entrained into the current and travels with the flow. We measured the change in the total volume of the currents with time and estimate that a fraction 0.33 ± 0.09 of displaced ambient fluid is entrained into the current. Some of the mixed fluid supplies the tail of the flow while the rest recirculates within the head. Approximately 25% of the total volume of the current is found to be left behind the turbulent front and forms a tail region that appears to be controlled by bottom friction.

Our experiments reveal that while the volume of the current is seen to become self-similar after some adjustment period, the buoyancy of the flow appears to slightly deviate from the self-similar approximation as seen by the gradual loss of buoyancy from the head into the wake. We have derived a new self-similar solution that includes the ambient entrainment at the nose, the vertical shear in the velocity and the lateral stratification of the buoyancy within the current. This model can capture the increase in depth and buoyancy towards the front as suggested experimentally.

In chapter 3, we explore the dynamics of turbulent axisymmetric gravity currents supplied by a constant buoyancy flux. Effective source Froude numbers, Fr_o, for the gravity currents were determined to be within the range of 1-2. The currents appear to form a steady tail region behind the advancing head, similar to the theoretical model proposed by Johnson *et al.* (2015). Although in their model, the mixing was ignored and they predict that the head advances as $r_n \sim t^{4/5}$. However, we found that the position of the front in our currents advances more closely to the prediction from a conventional scaling, $r_n \approx 1.32B_o^{1/4}t^{3/4}$.

As with the currents initiated from a finite volume release, the current becomes stratified both in velocity and density. Experiments in which dye is injected into the current illustrate that the dense fluid at the base travels faster than the front of the current. Once it arrives at the front, it circulates and mixes with the ambient fluid being displaced by the nose.

In the steady region observed behind the head, we attempted to measure the speed of the fluid by tracking structures within this region. The radial volume flux is then

estimated based on the velocity profile and is found to slightly increase with radius. This can be interpreted as a result of entrainment along the top boundary. The estimated entrainment coefficient is found to increase from ∼0.05 to ∼0.07 as Fr_o increases from 1.1 to 1.8. From our estimated vertical profile of radial velocity and the vertical profile of density acquired from the light attenuation technique, we estimated Ri_g at each radial position. This is found to be in excess of 0.25 in the main body of the current but is found to be just below 0.25 within a thin region near the top boundary of the current. The value for $Ri_g = 0.25$ is known to be a critical value above which the flows are expected to be stable and do not mix (Turner, 1979). This suggests that mixing appears to be localised near the top boundary of the current but not throughout the whole depth.

We found that mixing coefficients at the head of the current decreases from ∼0.2 to ∼0.18 with increasing Fr_o from 1.1 to 1.8. We note that the decreasing trend is also reported in the case of two-dimensional gravity currents (Sher & Woods, 2017). The theoretical model for non-mixing current proposed by Johnson *et al.* (2015) appears to underestimate both the depth profile and nose position with time when compared to our experimental data.

5.1.2 Future work

We have explored mixing in axisymmetric gravity currents, yet there are many problems related to this topic that can be investigated further. Here we propose a few topics that can be explored in order to provide better understanding about the dynamics of gravity currents.

- Gravity currents in nature can be several hundred metres thick and some of these currents may occur randomly in time, such as those produced by volcanic eruptions or slope failure in marine sediment (Simpson, 1999). The data acquisition for these field-scale currents can be challenging. However, there have been a few studies on field-scale experiments on the natural gravity-driven flows such as those presented by (Princevac *et al.*, 2005) and the references therein. It will be useful to investigate the applicability of our experimental results to these field observations.

- In geophysical flow situations, such as with turbidity currents or pyroclastic flows, the currents move over a subtle slope. It would be valuable to explore the impact of the inclination of the slope on the mixing coefficients of the currents.

Roughness of the boundary can also play an important role in the dynamics of the head and the effects of such drag on the mixing coefficients could also be tested. It would also be of interest to explore the mixing in gravity currents running along a free surface as it would be applicable to the case of fresh river discharges into the ocean.

- As mentioned in the introduction, in many geophysical flows, the excess buoyancy results from suspended particles within the currents. As these particles can settle as the flows propagate, the dynamics of the flow, and also of the entrainment of ambient fluid, may be affected by the particle load. Here it might be possible to extend our light attenuation technique to measure the spatial distribution of the particles within the flow as high particle concentrations would result in less light transmission in contrast to low particle concentration.

- Although the technique used to estimate the vertical profile for radial velocity is found to be useful, it would be interesting to compare this measured speed to those acquired from other techniques, for example, by injecting a vertical line of dye into the flow and tracking their position in time, or by applying a PIV technique to measure the velocity field in detail.

5.2 Thermodynamics of a lava lake

5.2.1 Conclusion

In **chapter 4**, we described a new series of laboratory experiments that explore the influence of gas flow in mixing liquid within a vertical conduit. Although the liquid is stagnant, dye tracers introduced at the bottom of the conduit are shown to propagate slowly upwards by the dispersive mixing associated with the bubble wakes.

For liquid of kinematic viscosity used in our study (0.1 to 0.01 $cm^2\ s^{-1}$), the Reynolds number based on the bubble speed is in the range 800 - 8000. This suggests bubbles have a turbulent wake as found in our study. As the liquid ahead of a bubble is displaced and falls down along the film region between the bubble and the conduit wall, it forms a wake behind the bubble where it is mixed. With time, this results in gradual upward propagation of dye tracer originally introduced at the bottom of the conduit. The propagation is found to be diffusion-like and the dispersion coefficient is determined accordingly for different superficial gas speeds as $D \approx 1.25 d_c u_g^{1/2} u_o^{3/2}/(u_g +$

u_o), where u_g is the superficial gas speed and u_o is the rise speed of single bubbles which is a function of the conduit diameter. In the limit where the superficial gas speed is small ($u_g \to 0$), this empirical relation can be written in terms of the volume gas flux as $D \approx \dot{V}_g^{1/2} u_o^{1/2}$.

The experimental gas-liquid flows in a vertical pipe resemble gas-magma separated flow in magmatic conduits. By analogy with the dispersion of dye in the experimental system, we envisage that there is a dispersive heat flux along the conduit driven by the mixing through the wakes of the successive bubbles. Using the empirical model for the dispersion based on the dye transport experiments, we find that at lava lakes, the mixing produced by the bubbles may supply sufficient heat flux to the lakes in order to maintain the radiative and convective losses from the lake. The conventional model that there is a counterflow driving the heat flux may be less applicable in the upper few hundred metres of the conduit owing to the mixing by the wakes of the slugs, which will tend to break down this convective exchange flow.

We first derive a model to predict the temperature gradient within the conduit due to the dispersive mixing induced by gas bubbles. In the model we account for the temperature change associated with the work done by gas expansion due to decompression as gas bubbles travel up the conduit. This leads to a temperature difference between gas and magma as they arrive at the surface which may be consistent with data from several lava lakes.

5.2.2 Future work

Our work provides a new model that explains the heat transfer mechanism within a volcanic conduit. In order to clarify and improve our understanding of the role of bubble flow on heat transport in volcanic conduit, we propose some further experiments and modelling studies to build on the present work.

- In our study, the liquid viscosity is chosen to ensure the development of a turbulent wake behind each bubble. However, bubbles in volcanic conduits, in some cases, might have lower Reynolds numbers, so that non-turbulent wakes may develop. Experiments with liquid of higher viscosity would enable quantification of the mixing by lower Reynolds number bubbles. Experiments with a variety of conduit diameters would also help test our empirical formula for the dispersion coefficient. Furthermore, the roughness in the conduit wall might also play an

important role in magma mixing as it encourages the turbulent motion of the liquid.

- Based on the field data, bubble recurrence time can be of the order of 10 minutes and each bubble is more likely to rise independently. To explore this limit where interaction between gas slugs is minimised, we might introduce the gas as a series of pulses instead of a steady flux that is used in our study.

- The temperature decrease within volcanic conduits can lead to crystallisation of liquid magma. The presence of solid particles can potentially affect the motion of liquid and also the rise of bubbles. This process could be investigated using laboratory experiments.

- Apart from conduit-filling bubbles within the volcanic conduit, it is widely believed that there is a substantial amount of degassing at shallow levels. These bubbles form at a shallow depth and are expected to be much smaller and dispersed within the conduit. This may resemble the bubbly flow regime that can be achieved in experiments with a lower gas flux. An experimental study of the mixing produced by separated bubbly flow would provide further understanding of the influence of gas bubbles of different sizes on the heat transport in the volcanic plumbing system. It would be interesting to include this additional gas flux in the model.

References

Adduce, C., Sciortino, G. & Proietti, S. 2012 Gravity Currents Produced by Lock Exchanges: Experiments and Simulations with a Two-Layer Shallow-Water Model with Entrainment. *Journal of Hydraulic Engineering* **138** (2), 111–121.

Allard, Patrick, Burton, Mike, Sawyer, Georgina & Bani, Philipson 2016 Degassing dynamics of basaltic lava lake at a top-ranking volatile emitter: Ambrym volcano, Vanuatu arc. *Earth and Planetary Science Letters* **448**, 69–80.

Allard, P., Carbonnelle, J., Métrich, N., Loyer, H. & Zettwoog, P. 1994 Sulphur output and magma degassing budget of Stromboli volcano. *Nature* **368**, 326–330.

Ancey, Christophe & Bain, Vincent 2015 Dynamics of glide avalanches and snow gliding. *Reviews of Geophysics* **53** (3), 745–784.

Beckett, F. M., Mader, H. M., Phillips, J. C., Rust, A. C. & Witham, F. 2011 An experimental study of low-Reynolds-number exchange flow of two Newtonian fluids in a vertical pipe. *Journal of Fluid Mechanics* **682** (2011), 652–670.

Benjamin, T. Brooke 1968 Gravity currents and related phenomena. *Journal of Fluid Mechanics* **31** (02), 209.

Bizouard, H, Barberi, F & Varet, J 1980 Mineralogy and petrology of Erta Ale and Boina volcanic series, Afar rift, Ethiopia. *Journal of Petrology* **21** (2), 401–436.

Bonnecaze, Roger T., Hallworth, Mark a., Huppert, Herbert E. & Lister, John R. 1995 Axisymmetric particle-driven gravity currents. *Journal of Fluid Mechanics* **294**, 93.

Bouche, E., Vergniolle, S., Staudacher, T., Nercessian, A., Delmont, J. C., Frogneux, M., Cartault, F. & Le Pichon, A. 2010 The role of large bubbles detected from acoustic measurements on the dynamics of Erta 'Ale lava lake (Ethiopia). *Earth and Planetary Science Letters* **295** (1-2), 37–48.

Britter, R. E. 1979 The spread of a negatively buoyant plume in a calm environment. *Atmospheric Environment* **13** (9), 1241–1247.

Britter, R. E. & Simpson, J. E. 1978 Experiments on the dynamics of a gravity current head. *Journal of Fluid Mechanics* **88**, 223.

Burgi, P. Y., Darrah, T. H., Tedesco, D. & Eymold, W. K. 2014 Dynamics of the Mount Nyiragongo lava lake. *Journal of Geophysical Research: Solid Earth* **119** (5), 4106–4122.

Burgisser, Alain, Oppenheimer, Clive, Alletti, Marina, Kyle, Philip R., Scaillet, Bruno & Carroll, Michael R. 2012 Backward tracking of gas chemistry measurements at Erebus volcano. *Geochemistry, Geophysics, Geosystems* **13** (11), 1–24.

Burton, M., Allard, P., Muré, F. & La Spina, A. 2007 Magmatic Gas Composition Reveals the Source Depth of Slug-Driven Strombolian Explosive Activity. *Science* **317** (5835), 227 LP – 230.

Calkins, J., Oppenheimer, C. & Kyle, P. R. 2008 Ground-based thermal imaging of lava lakes at Erebus volcano, Antarctica. *Journal of Volcanology and Geothermal Research* **177** (3), 695–704.

Campos, J. B. L. M. & Carvalho, J. R. F. Guedes De 1988 An experimental study of the wake of gas slugs rising in liquids. *Journal of Fluid Mechanics* **196** (-1), 27.

Cantero, M. I., Balachandar, S. & Garcia, M. H. 2007*a* High-resolution simulations of cylindrical density currents. *Journal of Fluid Mechanics* **590**, 437–469.

Cantero, Mariano I., Lee, J. R., Balachandar, S. & Garcia, Marcelo H. 2007*b* On the front velocity of gravity currents. *Journal of Fluid Mechanics* **586**, 1–39.

Carazzo, Guillaume, Kaminski, Edouard & Tait, Stephen 2006 The route to self-similarity in turbulent jets and plumes. *Journal of Fluid Mechanics* **547**, 137–148.

Chen, Jing-Chang 1980 Studies on gravitational spreading currents. PhD thesis, California Institute of Technology.

Davies, R. M. & Taylor, G. 1950 The Mechanics of Large Bubbles Rising through Extended Liquids and through Liquids in Tubes. *Proceedings of the Royal Society A: Mathematical, Physical and Engineering Sciences* **200** (1062), 375–390.

Del Bello, Elisabetta, Llewellin, Edward W., Taddeucci, Jacopo, Scarlato, Piergiorgio & Lane, Steve J. 2012 An analytical model for gas overpressure in slug-driven explosions: Insights into Strombolian volcanic eruptions. *Journal of Geophysical Research: Solid Earth* **117** (2).

Dufek, Josef 2016 The fluid mechanics of pyroclastic density currents. *Annual Review of Fluid Mechanics* **48**, 459–485.

Dunbar, Nelia W, Cashman, Katharine V & Dupré, Roslyn 1994 Crystallization processes of anorthoclase phenocrysts in the Mount Erebus magmatic system: evidence from crystal composition, crystal size distributions, and volatile

contents of melt inclusions. *Volcanological and environmental studies of Mount Erebus, Antarctica* pp. 129–146.

Ellison, TH & Turner, JS 1959 Turbulent entrainment in stratified flows. *Journal of Fluid Mechanics* (February).

Fernandes, R. C., Semiat, R. & Dukler, A. E. 1983 Hydrodynamic model for gasliquid slug flow in vertical tubes. *AIChE Journal* **29** (6), 981–989.

Fragoso, A. T., Patterson, M. D. & Wettlaufer, J. S. 2013 Mixing in gravity currents. *Journal of Fluid Mechanics* **734**, R2.

Francis, P., Oppenheimer, C. & Stevenson, D. 1993 Endogenous growth of persistently active volcanoes. *Nature* **366** (6455), 554–557.

Garcia, Michael O, Rhodes, J Michael, Wolfe, E W, Ulrich, George E & Ho, R A 1992 Petrology of lavas from episodes 2–47 of the Puu Oo eruption of Kilauea Volcano, Hawaii: evaluation of magmatic processes. *Bulletin of Volcanology* **55** (1-2), 1–16.

Gonnermann, Hm & Manga, Michael 2012 Dynamics of magma ascent in the volcanic conduit. *Seismo.Berkeley.Edu* pp. 55–84.

Gurioli, L., Harris, A. J. L., Houghton, B. F., Polacci, M. & Ripepe, M. 2008 Textural and geophysical characterization of explosive basaltic activity at Villarrica volcano. *Journal of Geophysical Research: Solid Earth* **113** (8), 1–16.

Hacker, J., Linden, P.F. & Dalziel, S.B. 1996 Mixing in lock-release gravity currents. *Dynamics of Atmospheres and Oceans* **24** (1-4), 183–195.

Hallworth, Mark A., Huppert, Herbert E., Phillips, Jeremy C. & Sparks, R. Stephen J. 1996 Entrainment into two-dimensional and axisymmetric turbulent gravity currents. *Journal of Fluid Mechanics* **308**, 289–311.

Hallworth, Mark A., Phillipsi, Jeremy C., Huppert, Herbert E. & Sparks, R. Stephen J. 1993 Entrainment in turbulent gravity currents. *Nature* **362**, 829–831.

Harmathy, Tibor Z. 1960 Velocity of large drops and bubbles in media of infinite or restricted extent. *AIChE Journal* **6** (2), 281–288.

Harris, A. J. L. 2008 Modeling lava lake heat loss, rheology, and convection. *Geophysical Research Letters* **35** (7), n/a–n/a.

Harris, A. J. L., Carniel, R. & Jones, J. 2005 Identification of variable convective regimes at Erta Ale Lava Lake. *Journal of Volcanology and Geothermal Research* **142** (3-4), 207–223.

Harris, A. J. L., Flynn, L. P., Rothery, D. A., Oppenheimer, C. & Sherman, S. B. 1999 Mass flux measurements at active lava lakes: Implications for magma recycling. *Journal of Geophysical Research: Solid Earth* **104** (B4), 7117–7136.

Harris, A. J. L. & Ripepe, M. 2007 Temperature and dynamics of degassing at Stromboli. *Journal of Geophysical Research* **112** (B3), B03205.

Harris, A. J. L. & Stevenson, D. S. 1997 Thermal observations of degassing open conduits and fumaroles at Stromboli and Vulcano using remotely sensed data. *Journal of Volcanology and Geothermal Research* **76** (3-4), 175–198.

Head, James W & Wilson, Lionel 1986 Volcanic processes and landforms on Venus: Theory, predictions, and observations. *Journal of Geophysical Research: Solid Earth* **91** (B9), 9407–9446.

Hogg, Andrew J, Hallworth, Mark A & Huppert, Herbert E 2005 On gravity currents driven by constant fluxes of saline and particle-laden fluid in the presence of a uniform flow. *Journal of Fluid Mechanics* **539** (2005), 349–385.

Hon, Ken, Kauahikaua, Jim, Denlinger, Roger & Mackay, Kevin 1994 Emplacement and inflation of pahoehoe sheet flows: Observations and measurements of active lava flows on Kilauea Volcano, Hawaii. *Geological Society of America Bulletin* **106** (3), 351–370.

Hoult, David P. 1972 Oil spreading on the sea. *Annual Review of Fluid Mechanics* **341** (1), 341–368.

Huppert, H. E. & Hallworth, M. A. 2007 Bi-directional flows in constrained systems. *Journal of Fluid Mechanics* **578** (2007), 95.

Huppert, Herbert E. & Simpson, John E. 1980 The slumping of gravity currents. *Journal of Fluid Mechanics* **99** (04), 785.

James, M. R., Lane, S. J. & Chouet, B. A. 2006 Gas slug ascent through changes in conduit diameter: Laboratory insights into a volcano-seismic source process in low-viscosity magmas. *Journal of Geophysical Research: Solid Earth* **111** (5), 1–25.

Johnson, ChristopherG., Hogg, AndrewJ., Huppert, HerbertE., Sparks, R.StephenJ., Phillips, JeremyC., Slim, AnjaC. & Woodhouse, MarkJ. 2015 Modelling intrusions through quiescent and moving ambients. *Journal of Fluid Mechanics* **771**, 370–406.

Johnson, Christopher G. & Hogg, Andrew J. 2013 Entraining gravity currents. *Journal of Fluid Mechanics* **731**, 477–508.

Johnson, Jeffrey, Aster, Richard, Jones, Kyle R., Kyle, Philip & McIntosh, Bill 2008 Acoustic source characterization of impulsive Strombolian eruptions from the Mount Erebus lava lake. *Journal of Volcanology and Geothermal Research* **177** (3), 673–686.

Johnson, Jeffrey B, Aster, Richard C. & Kyle, Philip R. 2004 Volcanic eruptions observed with infrasound. *Geophysical Research Letters* **31** (14), L14604.

Jones, Kyle R, Johnson, Jeffrey B, Aster, Rick, Kyle, Philip R & McIntosh, W. C. 2008 Infrasonic tracking of large bubble bursts and ash venting at Erebus Volcano, Antarctica. *Journal of Volcanology and Geothermal Research* **177** (3), 661–672.

Kaye, N. B. & Hunt, G. R. 2007 Overturning in a filling box. *Journal of Fluid Mechanics* **576**, 297–323.

Kazahaya, Kohei, Shinohara, Hiroshi & Saito, Genji 1994 Excessive degassing of Izu-Oshima volcano: magma convection in a conduit. *Bulletin of Volcanology* **56**, 207–216.

Kneller, Ben & Buckee, Clare 2000 The structure and fluid mechanics of turbidity currents: a review of some recent studies and their geological implications. *Sedimentology* **47**, 62–94.

Kyle, Philip R 1977 Mineralogy and glass chemistry of recent volcanic ejecta from Mt Erebus, Ross Island, Antarctica. *New Zealand journal of geology and geophysics* **20** (6), 1123–1146.

Le Guern, F. 1987 Mechanism of Energy Transfer in the Lava Lake of Niragongo (Zaire), 1959 - 1977. *Journal of Volcanology and Geothermal Research* **31**, 17–31.

Le Guern, F., Carbonnelle, J. & Tazieff, H. 1979 Erta'Ale lava lake: heart and gas transfer th the atmosphere. *Journal of Volcanology and Geothermal Research* **6**, 27–48.

Linden, Paul F. & Simpson, John E. 1990 Continous two-dimensional releases from an elevated source. *Journal of Loss Prevention in the Process Industries* **3** (1), 82–87.

Llewellin, E. W., Del Bello, E., Taddeucci, J., Scarlato, P. & Lane, S. J. 2012 The thickness of the falling film of liquid around a Taylor bubble. *Proceedings of the Royal Society A: Mathematical, Physical and Engineering Sciences* **468** (2140), 1041–1064.

Marino, B. M., Thomas, L. P. & Linden, P. F. 2005 The front condition for gravity currents. *Journal of Fluid Mechanics* **536**, 49–78.

Mayor, T S, Pinto, AMFR & Campos, JBLM 2008 Vertical slug flow in laminar regime in the liquid and turbulent regime in the bubble wake-comparison with fully turbulent and fully laminar regimes. *Chemical Engineering Science* **63** (14), 3614–3631.

Meiburg, Eckart & Kneller, Ben 2010 Turbidity Currents and Their Deposits. *Annual Review of Fluid Mechanics* **42** (1), 135–156.

Miles, John W. 1961 On the stability of heterogeneous shear flows. *Journal of Fluid Mechanics* **10** (04), 496.

Morgado, A. O., Miranda, J. M., Araújo, J. D.P. & Campos, J. B.L.M. 2016 Review on vertical gas–liquid slug flow. *International Journal of Multiphase Flow* **85**, 348–368.

Morton, B. R., Taylor, G. & Turner, J. S. 1956 Turbulent Gravitational Convection from Maintained and Instantaneous Sources. *Proceedings of the Royal Society A: Mathematical, Physical and Engineering Sciences* **234** (1196), 1–23.

Moussallam, Yves, Bani, Philipson, Curtis, Aaron, Barnie, Talfan, Moussallam, Manuel, Peters, Nial, Schipper, C. Ian, Aiuppa, Alessandro, Giudice, Gaetano, Amigo, Álvaro, Velasquez, Gabriela & Cardona, Carlos 2016 Sustaining persistent lava lakes: Observations from high-resolution gas measurements at Villarrica volcano, Chile. *Earth and Planetary Science Letters* **454**, 237–247.

Murphy, Lesley M. 1986 Linear feature detection and enhancement in noisy images via the Radon transform. *Pattern Recognition Letters* **4** (4), 279–284.

Neri, Augusto 1998 A local heat transfer analysis of lava cooling in the atmosphere: application to thermal diffusion-dominated lava flows. *Journal of Volcanology and Geothermal Research* **81** (3-4), 215–243.

Nicklin, D J 1962 Two-phase bubble flow. *Chemical Engineering Science* **17** (March), 693–702.

Oppenheimer, Clive & Kyle, Philip R. 2008 Probing the magma plumbing of Erebus volcano, Antarctica, by open-path FTIR spectroscopy of gas emissions. *Journal of Volcanology and Geothermal Research* **177** (3), 743–754.

Oppenheimer, Clive, Lomakina, Alexandra S., Kyle, Philip R., Kingsbury, Nick G. & Boichu, Marie 2009 Pulsatory magma supply to a phonolite lava lake. *Earth and Planetary Science Letters* **284** (3-4), 392–398.

Oppenheimer, C., McGonigle, A. J S, Allard, P., Wooster, M. J. & Tsanev, V. 2004 Sulfur, heat, and magma budget of Erta 'Ale lava lake, Ethiopia. *Geology* **32** (6), 509–512.

Oppenheimer, Clive, Moretti, Roberto, Kyle, Philip R., Eschenbacher, Al, Lowenstern, Jacob B., Hervig, Richard L. & Dunbar, Nelia W. 2011 Mantle to surface degassing of alkalic magmas at Erebus volcano, Antarctica. *Earth and Planetary Science Letters* **306** (3-4), 261–271.

Oppenheimer, C. & Yirgu, G. 2002 Thermal imaging of an active lava lake: Erta 'Ale volcano, Ethiopia. *International Journal of Remote Sensing* **23** (22), 4777–4782.

Özgökmen, Tamay M., Iliescu, Traian & Fischer, Paul F. 2009 Reynolds number dependence of mixing in a lock-exchange system from direct numerical and large eddy simulations. *Ocean Modelling* **30** (2-3), 190–206.

Patrick, M. R., Orr, T., Swanson, D. A. & Lev, E. 2016 Shallow and deep controls on lava lake surface motion at Klauea Volcano. *Journal of Volcanology and Geothermal Research* **328**, 247–261.

Patterson, M. D., Simpson, J. E., Dalziel, S. B. & van Heijst, G. F. 2006 Vortical motion in the head of an axisymmetric gravity current. *Physics of Fluids* **18** (4), 046601.

Peters, Nial, Oppenheimer, Clive, Kyle, Philip & Kingsbury, Nick 2014 Decadal persistence of cycles in lava lake motion at Erebus volcano, Antarctica. *Earth and Planetary Science Letters* **395**, 1–12.

Pinto, A. M.F.R. & Campos, J. B.L.M. 1996 Coalescence of two gas slugs rising in a vertical column of liquid. *Chemical Engineering Science* **51** (1), 45–54.

Pioli, L., Bonadonna, C., Azzopardi, B. J., Phillips, J. C. & Ripepe, M. 2012 Experimental constraints on the outgassing dynamics of basaltic magmas. *Journal of Geophysical Research: Solid Earth* **117** (3), 1–17.

Piper, David J W, Shor, Alexander N & Clarke, John E Hughes 1988 The 1929 "Grand Banks" earthquake, slump, and turbidity current. *Geological Society of America Special Papers* **229**, 77–92.

Prandtl, Ludwig 1952 *Essentials of fluid dynamics: With applications to hydraulics aeronautics, meteorology, and other subjects.*. Hafner Pub. Co.

Princevac, M., Fernando, H. J. S. & Whiteman, C. D. 2005 Turbulent entrainment into natural gravity-driven flows. *Journal of Fluid Mechanics* **533**, 259–268.

Ripepe, Maurizio, Harris, Andrew J.L. & Carniel, Roberto 2002 Thermal, seismic and infrasonic evidences of variable degassing rates at Stromboli volcano. *Journal of Volcanology and Geothermal Research* **118** (3-4), 285–297.

Roche, Olivier, Phillips, Jeremy C & Kelfoun, Karim 2013 Pyroclastic density currents. In *Modeling Volcanic Processes* (ed. Sarah A Fagents, Tracy K P Gregg & Rosaly M C Lopes), pp. 203–229. Cambridge University Press.

Rottman, JW & Simpson, JE 1983 Gravity currents produced by instantaneous releases of a heavy fluid in a rectangular channel. *Journal of Fluid Mechanics* **135**, 95–110.

Rowe, C. A., Aster, R. C., Kyle, P. R., Dibble, R. R. & Schlue, J. W. 2000 Seismic and acoustic observations at Mount Erebus Volcano, Ross Island, Antarctica, 1994-1998. *Journal of Volcanology and Geothermal Research* **101** (1-2), 105–128.

Sawyer, G. M., Oppenheimer, C., Tsanev, V. I. & Yirgu, G. 2008 Magmatic degassing at Erta 'Ale volcano, Ethiopia. *Journal of Volcanology and Geothermal Research* **178** (4), 837–846.

Sawyer, G. M., Salerno, G. G., Le Blond, J. S., Martin, R. S., Spampinato, L., Roberts, T. J., Mather, T. A., Witt, M. L I, Tsanev, V. I. & Oppenheimer, C. 2011 Gas and aerosol emissions from Villarrica volcano, Chile. *Journal of Volcanology and Geothermal Research* **203** (1-2), 62–75.

Seyfried, Ralf & Freundt, Armin 2000 Experiments on conduit flow and eruption behavior of basaltic volcanic eruptions. *Journal of Geophysical Research: Solid Earth* **105** (B10), 23727–23740.

Sharma, Prem V 1997 *Environmental and engineering geophysics*. Cambridge university press.

Sher, Diana & Woods, Andrew W. 2015 Gravity currents: entrainment, stratification and self-similarity. *Journal of Fluid Mechanics* **784** (0), 130–162.

Sher, Diana & Woods, Andrew W. 2017 Mixing in continuous gravity currents. *Journal of Fluid Mechanics* **818**, R4.

Shin, J. O., Dalziel, S. B. & Linden, P. F. 2004 Gravity currents produced by lock exchange. *Journal of Fluid Mechanics* **521**, 1–34.

Simpson, JE 1999 *Gravity currents: In the environment and the laboratory*. Cambridge University Press.

Slim, Anja C. & Huppert, Herbert E. 2004 Self-similar solutions of the axisymmetric shallow-water equations governing converging inviscid gravity currents. *Journal of Fluid Mechanics* **506**, 331–355.

Slim, A. C. & Huppert, H. E. 2011 Axisymmetric, constantly supplied gravity currents at high Reynolds number. *Journal of Fluid Mechanics* **675**, 540–551.

van Sommeren, Daan D. J. a., Caulfield, C. P. & Woods, Andrew W. 2012 Turbulent buoyant convection from a maintained source of buoyancy in a narrow vertical tank. *Journal of Fluid Mechanics* **701**, 278–303.

Spampinato, L., Ganci, G., Hernández, P. A., Calvo, D., Tedesco, D., Pérez, N. M., Calvari, S., Del Negro, C. & Yalire, M. M. 2013 Thermal insights into the dynamics of Nyiragongo lava lake from ground and satellite measurements. *Journal of Geophysical Research: Solid Earth* **118** (11), 5771–5784.

Spampinato, L., Oppenheimer, C., Calvari, S., Cannata, A. & Montalto, P. 2008 Lava lake surface characterization by thermal imaging: Erta 'ale volcano (Ethiopia). *Geochemistry, Geophysics, Geosystems* **9** (12).

Sparks, Rsj, Bursik, Mi, Carey, Sn, Gilbert, Jennifer, Glaze, Ls, Sigurdsson, H & Woods, a 1997 *Volcanic Plumes*. Chichester ; New York: Wiley.

Stevenson, David S. & Blake, Stephen 1998 Modelling the dynamics and thermodynamics of volcanic degassing. *Bulletin of Volcanology* **60** (4), 307–317.

Suckale, Jenny, Hager, Bradford H., Elkins-Tanton, Linda T. & Nave, Jean-Christophe 2010 It takes three to tango: 2. Bubble dynamics in basaltic volcanoes and ramifications for modeling normal Strombolian activity. *Journal of Geophysical Research* **115** (B7), B07410.

Taitel, Y, Bornea, D & Dukler, AE 1980 Modelling Flow Pattern Transitions for Steady Upward Gas-Liquid Flow in Vertical Tubes. *AIChE Journal* **26** (3), 345–354.

Takamura, Koichi, Fischer, Herbert & Morrow, Norman R. 2012 Physical properties of aqueous glycerol solutions. *Journal of Petroleum Science and Engineering* **98-99**, 50–60.

Tamburello, G, Aiuppa, A, Kantzas, E. P., McGonigle, A. J.S. & Ripepe, M 2012 Passive vs. active degassing modes at an open-vent volcano (Stromboli, Italy). *Earth and Planetary Science Letters* **359-360**, 106–116.

Tazieff, Haroun 1994 Permanent lava lakes: observed facts and induced mechanisms. *Journal of Volcanology and Geothermal Research* **63** (1-2), 3–11.

Turner, John Stewart 1979 *Buoyancy effects in fluids*. Cambridge University Press.

US Geological Survey 2016 Glossary - Lava lake.

Varjavand, Peyman, Ghomeshi, Mehdi, Dalir, Ali Hosseinzadeh, Farsadizadeh, Davood & Gorgij, Alireza Docheshmeh 2015 Experimental observation of saline underflows and turbidity currents, flowing over rough beds. *Canadian Journal of Civil Engineering* **42** (11), 834–844.

Vergniolle, Sylvie & Bouche, Emmanuella 2016 Gas-driven lava lake fluctuations at Erta 'Ale volcano (Ethiopia) revealed by MODIS measurements. *Bulletin of Volcanology* **78** (9).

Vergniolle, S. & Brandeis, G. 1996 Strombolian explosions: 1. A large bubble breaking at the surface of a lava column as a source of sound. *Journal of Geophysical Research* **101** (B9), 20433.

Vergniolle, S. & Gaudemer, Y. 2015 From Reservoirs and Conduits to the Surface. pp. 289–321.

Viana, F., Pardo, R., Yánez, R., Trallero, J. L. & Joseph, D. D. 2003 Universal correlation for the rise velocity of long gas bubbles in round pipes. *Journal of Fluid Mechanics* **494** (2003), S0022112003006165.

Witham, Fred 2011 Conduit convection, magma mixing, and melt inclusion trends at persistently degassing volcanoes. *Earth and Planetary Science Letters* **301** (1-2), 345–352.

Wooster, M. J., Wright, R. & Rothery, D. A. 1997 Cooling mechanisms and an approximate thermal budget for the 1991-1993 Mount Etna lava flow. *Geophysical Research Letters* **24** (24), 3277–3280.

Wright, Robert & Flynn, Luke P. 2004 Space-based estimate of the volcanic heat flux into the atmosphere during 2001 and 2002. *Geology* **32** (3), 189–192.

Wright, Robert & Pilger, Eric 2008 Satellite observations reveal little interannual variability in the radiant flux from the Mount Erebus lava lake. *Journal of Volcanology and Geothermal Research* **177** (3), 687–694.

Appendix A

A.1 Error approximation based on conservation of dyes

In the experiments on axisymmetric gravity currents, the local light intensity is converted to the local (spanwise-averaged) buoyancy. In the case of a finite volume release, the total buoyancy in the observation field can be calculated using the relationship

$$B_o = g'_o V_o = \int r \int g' \mathrm{d}z \mathrm{d}r, \tag{A.1}$$

where B_o is the total buoyancy which is the product of the initial buoyancy, g'_o, and the lock volume, V_o. $g'(r, z, t)$ is the local buoyancy that can be measured using the calibration function determined locally. This is expected to be constant with time due to the conservation of buoyancy. Figure A.1 shows the ratio between the measured total buoyancy to the initial total buoyancy which is found to be within approximately 7-8%. Different colours represent values from different experiments. Similarly, the total buoyancy in the case of steady flux gravity currents can also be determined at each time. In these experiments, however, the expected total buoyancy is no longer constant but is a function of time

$$B(t) = g'_j Q_j t = \int r \int g' \mathrm{d}z \mathrm{d}r, \tag{A.2}$$

where $B(t)$ is the expected total buoyancy in the experimental tank, g'_j is the initial source buoyancy and Q_j is the volumetric flux. For these experiments, volume of the liquid pumped into the tank and the time taken to finish each experiment is measured to determine Q_j for each experiment. Figure A.2 shows the ratio between the

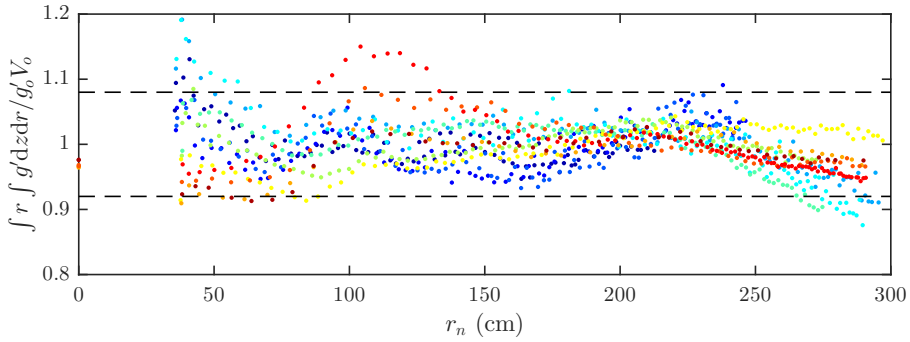

Fig. A.1 The ratio between the total measured buoyancy to the expected buoyancy in the case of discrete release gravity currents (chapter 2). Colours represent different experiments as coded in table 2.1.

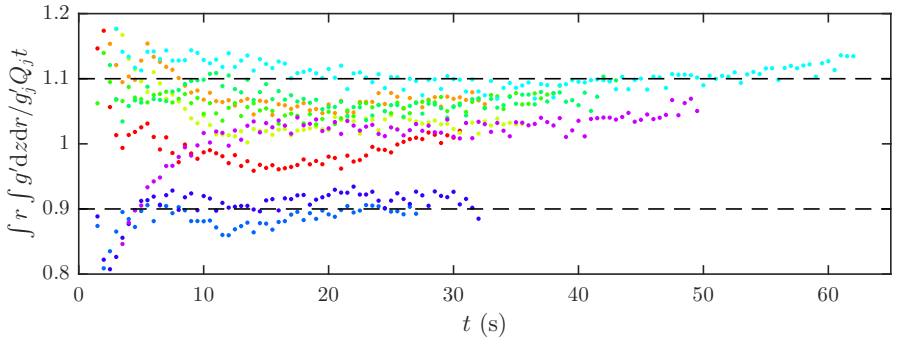

Fig. A.2 The ratio between the total measured buoyancy to the expected buoyancy in the case of constant flux gravity currents (chapter 3). Colours represent different experiments as coded in table 3.1.

measured total buoyancy to the expected total buoyancy which is found to be within approximately 10-12%. Different colours represent values from different experiments.

A.2 The sensitivity for the current detection

In order to differentiate the pixels that capture the current (red dye) from the ambient fluid (colourless), a threshold light intensity is carefully chosen such that the noise pixels are filtered out yet pixels associated with fluid of low dye concentration is included. The grayscale images, $I(r, z)$, of the flows are first converted into binary

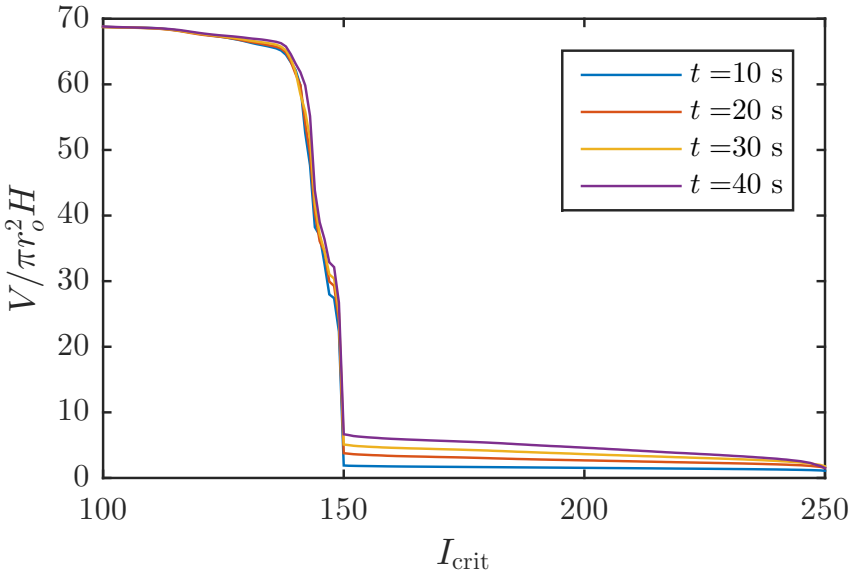

Fig. A.3 The normalised volumes detected when different threshold digital numbers are used. The threshold number of ~ 150 is consistent for all the four images corresponding to images taken at t =10, 20, 30 and 40 s. Images are taken from the finite volume release gravity current H.

images, $I'(r,z)$, based on critical light intensities, I_{crit}

$$I'(r,z) = \begin{cases} 1 & \text{if} \quad I(r,z) \leq I_{\text{crit}} \quad \text{and} \\ 0 & \text{if} \quad I(r,z) > I_{\text{crit}}. \end{cases} \tag{A.3}$$

As a result, the volume of the flow can then be determined for each image using the relationship

$$V(t) = \int r \int I' \mathrm{d}r\mathrm{d}z. \tag{A.4}$$

For each image (corresponding to an instantaneous time), we can repeat calculating V corresponding to different I_{crit}. Figure A.3 shows the normalised volume detected as a function of different I_{crit} on four representative images: $t = 10, 20, 30$ and 40 s (chapter 2, exp. H). Choosing too small a threshold digital number will include more noise and overestimate the detected volumes. Here, we chose $I_{\text{crit}} = 155$ to be the threshold digital number to be used to distinguish current pixels from the noise pixels.